# Experimental and numerical study of C electromigration in iron during ferrite - austenite phase transformation

Maxime Monzey

N°d'ordre NNT : 2022LYSEI019

**THÈSE de DOCTORAT DE L'UNIVERSITÉ DE LYON**
opérée au sein de
**l'Institut National des Sciences Appliquées de Lyon**

**Ecole Doctorale** N° ED 34
**Matériaux de Lyon**

**Spécialité/ discipline de doctorat** :
Matériaux

Soutenue publiquement le 24/03/2022, par :
**Maxime MONZEY**

---

# Experimental and numerical study of carbon electromigration in iron during ferrite – austenite phase transformation

---

Devant le jury composé de :

| | | |
|---|---|---|
| FRACZKIEWICZ, Anna | Directrice de recherche, EMSE | Présidente du jury |
| APPOLAIRE, Benoit | Professeur, Université de Lorraine | Rapporteur |
| GOURGUES-LORENZON, Anne-Françoise | Professeure, Mine ParisTech | Rapporteuse |
| DENIS, Sabine | Professeure, Université de Lorraine | Examinatrice |
| LE BOUAR, Yann | Directeur de recherche, CNRS | Examinateur |
| VAN LANDEGHEM, Hugo | Chargé de recherche, CNRS | Examinateur |
| CHANTRENNE, Patrice | Professeur, INSA LYON | Directeur de thèse |
| FABRÈGUE, Damien | Professeur, INSA LYON | Co-directeur |
| PEREZ, Michel | Professeur, INSA LYON | Invité |

# Département FEDORA – INSA Lyon - Ecoles Doctorales

| SIGLE | ECOLE DOCTORALE | NOM ET COORDONNEES DU RESPONSABLE |
|---|---|---|
| CHIMIE | **CHIMIE DE LYON**<br>**https://www.edchimie-lyon.fr**<br>Sec. : Renée EL MELHEM<br>Bât. Blaise PASCAL, 3e étage<br>secretariat@edchimie-lyon.fr | **M. Stéphane DANIELE**<br>C2P2-CPE LYON-UMR 5265<br>Bâtiment F308, BP 2077<br>43 Boulevard du 11 novembre 1918<br>69616 Villeurbanne<br>**directeur@edchimie-lyon.fr** |
| E.E.A. | **ÉLECTRONIQUE, ÉLECTROTECHNIQUE, AUTOMATIQUE**<br>**https://edeea.universite-lyon.fr**<br>Sec. : Stéphanie CAUVIN<br>Bâtiment Direction INSA Lyon<br>Tél : 04.72.43.71.70<br>secretariat.edeea@insa-lyon.fr | **M. Philippe DELACHARTRE**<br>INSA LYON<br>Laboratoire CREATIS<br>Bâtiment Blaise Pascal, 7 avenue Jean Capelle<br>69621 Villeurbanne CEDEX<br>Tél : 04.72.43.88.63<br>**philippe.delachartre@insa-lyon.fr** |
| E2M2 | **ÉVOLUTION, ÉCOSYSTÈME, MICROBIOLOGIE, MODÉLISATION**<br>**http://e2m2.universite-lyon.fr**<br>Sec. : Sylvie ROBERJOT<br>Bât. Atrium, UCB Lyon 1<br>Tél : 04.72.44.83.62<br>secretariat.e2m2@univ-lyon1.fr | **M. Philippe NORMAND**<br>Université Claude Bernard Lyon 1<br>UMR 5557 Lab. d'Ecologie Microbienne<br>Bâtiment Mendel<br>43, boulevard du 11 Novembre 1918<br>69 622 Villeurbanne CEDEX<br>**philippe.normand@univ-lyon1.fr** |
| EDISS | **INTERDISCIPLINAIRE SCIENCES-SANTÉ**<br>**http://ediss.universite-lyon.fr**<br>Sec. : Sylvie ROBERJOT<br>Bât. Atrium, UCB Lyon 1<br>Tél : 04.72.44.83.62<br>secretariat.ediss@univ-lyon1.fr | **Mme Sylvie RICARD-BLUM**<br>Institut de Chimie et Biochimie Moléculaires et Supramoléculaires (ICBMS) - UMR 5246 CNRS - Université Lyon 1<br>Bâtiment Raulin - 2ème étage Nord<br>43 Boulevard du 11 novembre 1918<br>69622 Villeurbanne Cedex<br>Tél : +33(0)4 72 44 82 32<br>**sylvie.ricard-blum@univ-lyon1.fr** |
| INFOMATHS | **INFORMATIQUE ET MATHÉMATIQUES**<br>**http://edinfomaths.universite-lyon.fr**<br>Sec. : Renée EL MELHEM<br>Bât. Blaise PASCAL, 3e étage<br>Tél : 04.72.43.80.46<br>infomaths@univ-lyon1.fr | **M. Hamamache KHEDDOUCI**<br>Université Claude Bernard Lyon 1<br>Bât. Nautibus<br>43, Boulevard du 11 novembre 1918<br>69 622 Villeurbanne Cedex France<br>Tél : 04.72.44.83.69<br>**hamamache.kheddouci@univ-lyon1.fr** |
| Matériaux | **MATÉRIAUX DE LYON**<br>**http://ed34.universite-lyon.fr**<br>Sec. : Yann DE ORDENANA<br>Tél : 04.72.18.62.44<br>yann.de-ordenana@ec-lyon.fr | **M. Stéphane BENAYOUN**<br>Ecole Centrale de Lyon<br>Laboratoire LTDS<br>36 avenue Guy de Collongue<br>69134 Ecully CEDEX<br>Tél : 04.72.18.64.37<br>**stephane.benayoun@ec-lyon.fr** |
| MEGA | **MÉCANIQUE, ÉNERGÉTIQUE, GÉNIE CIVIL, ACOUSTIQUE**<br>**http://edmega.universite-lyon.fr**<br>Sec. : Stéphanie CAUVIN<br>Tél : 04.72.43.71.70<br>Bâtiment Direction INSA Lyon<br>mega@insa-lyon.fr | **M. Jocelyn BONJOUR**<br>INSA Lyon<br>Laboratoire CETHIL<br>Bâtiment Sadi-Carnot<br>9, rue de la Physique<br>69621 Villeurbanne CEDEX<br>**jocelyn.bonjour@insa-lyon.fr** |
| ScSo | **ScSo***<br>**https://edsciencessociales.universite-lyon.fr**<br>Sec. : Mélina FAVETON<br>INSA : J.Y. TOUSSAINT<br>Tél : 04.78.69.77.79<br>melina.faveton@univ-lyon2.fr | **M. Christian MONTES**<br>Université Lumière Lyon 2<br>86 Rue Pasteur<br>69365 Lyon CEDEX 07<br>**christian.montes@univ-lyon2.fr** |

*ScSo : Histoire, Géographie, Aménagement, Urbanisme, Archéologie, Science politique, Sociologie, Anthropologie

*"C'qui compte c'est pas l'arrivée, c'est la quête."*

Orelsan, *La quête*
Orelsan / Phazz & Skread, (4'04) Album : *Civilisation*, Wagram Music, 2021.

# Remerciements

3 ans (et demi) de thèse se referment alors que je rédige ces dernières lignes. Une période difficile de par la quantité de travail et l'investissement qu'elle représente, les épreuves rencontrées tant scientifiques que mentales ... L'idée a germé lors de mon stage à Saint-Gobain Recherche mais je ne savais pas dans quoi je m'embarquais ! Et pourtant j'ai aimé cette aventure, cette expérience humaine, car j'ai rencontré de nombreuses personnes dont j'ai tâché de tirer le meilleur. Je me suis appuyé sur elles pour atteindre mes objectifs et je me dois de leur faire honneur maintenant.

Je voudrais dans un premier temps remercier les membres de mon jury pour avoir accepté d'évaluer mon travail. Merci donc à Anna, présidente de mon jury, pour vos retours et les discussions scientifiques précédemment à la soutenance. Je vous avais contacté à propos du fer ARMCO mais vous avez été rapidement intéressée par l'ensemble de mon travail et cela ne pouvait s'arrêter à une simple visio. Je remercie les deux rapporteurs pour leur lecture approfondie de mon manuscrit. Benoit - "pour sauver la situation parce que vous êtes sympas" - pour les commentaires notamment sur la thermodynamique et la modélisation, mais également dans le cadre des réunions de projet ECUME. Merci également d'avoir joué le rôle du méchant car je ne me sentirais pas crédible avec un jury conciliant. Anne-Françoise, pour votre regard neuf sur les microstructures et vos remarques enrichissantes, j'admire votre rigueur et vos qualités scientifiques. Merci à Hugo, Sabine et Yann d'avoir accepté de prendre le temps d'évaluer mon travail en participant à ma soutenance et pour la riche discussion que nous avons partagée.

Je tiens évidemment à remercier chaleureusement mes encadrants pour m'avoir guidé lors de ma quête scientifique et humaine. Patrice, je te suis très reconnaissant de m'avoir tendu la main après ma mésaventure de la thèse des couteaux. Un grand merci de m'avoir fait découvrir l'électro-migration et de m'avoir donné l'opportunité d'en explorer les possibilités avec toi. Certes, je suis plus friand du travail expéri-

mental que numérique mais nous avons pu travailler, échouer parfois, et apprendre sur les deux aspects. J'ai apporté ma modeste contribution dans le domaine et cela n'aurait pu se faire sans ton implication, ta bienveillance et ta pédagogie sans faille durant ma thèse. Damien, merci énormément d'avoir été présent aux moments où j'en avais le plus besoin. Ton expertise des métaux et ton soutien moral m'ont apporté la confiance nécessaire sur mes résultats et en arrivant à la soutenance. Bien que ton temps soit précieux, je savais que je pouvais compter sur toi à tout moment. Michel, je nous revois discuter au début de ma thèse, tes yeux pleins de la confiance que je n'avais pas encore. Merci pour ton écoute et tes précieux conseils, pour les tartes au sucre que je ne méritais peut être pas (sportivement) autant que les autres, pour les discussions sur mes résultats qui aboutissaient souvent à un schéma sur le tableau suivi d'un "Attends, je ne comprends pas". J'espère que j'aurai enfin réussi à répondre à tes questions lors de ma soutenance !

Un grand merci à ceux qui ont contribué de près ou de loin à ces travaux au laboratoire MATEIS et dans la meilleure équipe MétAl. Florian, l'indispensable soutien pour tout doctorant expérimentateur, merci pour les discussions jeux-vidéo et les bières partagées. Pierre-Antoine, merci pour tes précieuses participations à nos discussions qui m'ont permis de prendre du recul. Sophie et Xavier, pour votre expertise des aciers et vos précieux conseils pour avancer, pour les formations aux outils de microscopie et dureté, pour votre gentillesse et votre humour. Nos grands gourous Jean-Yves et Eric, j'admire votre simplicité et votre disponibilité. Merci beaucoup à Joël pour ton aide sur Python et Fiji, j'ai apprécié nos discussions et ces quelques jours de formation au CNRS d'Orléans avec toi.

La force (et l'honneur) de l'équipe MétAl réside parmi les nombreux et excellents doctorants qui la composent. Un immense merci aux membres du vrai bureau de l'ambiance, mes co-bureaux : Gabriel, pour m'avoir tout de suite accueilli ; Alexandre, pour le SAV du modèle GEM et la croziflette ; Théophile, le roseau qui plie mais ne rompt pas, merci frère pour les soirées péniche, les paquitos, la Chartreuse et l'ambiance (si il voit c'que j'veux dire) ; Arnaud, le meilleur allié et ami de galère, le Tic du Tac, merci pour ton humour et d'être aussi bon public pour mes pitreries. Thank you Masato for your kindness, your manners and your help during our experiments on the AET oven. I really enjoyed talking with you on a daily basis. Je suis reconnaissant pour tous les bons moments partagés avec vous, les jeunes (Ian, Julien, Louis, Mathilde, Maureen, Quentin, Samuel, Sébastien)

et les moins jeunes (Ce, Florian, Justine, Laurabelle, Louis, Lucas, Maël, Manon, Marion, Outhmane, Quentin). Au quotidien et à travers les différents évènements, on partage beaucoup plus que la science et le labeur, ce qui rend l'expérience d'autant plus enrichissante et agréable.

J'ai la chance d'être entouré de magnifiques personnes qui m'apportent chacun à leur manière. Merci aux crocodiles, aux lions, aux SA7 et aux Roucools. Merci à Antoine, mon meilleur ami et mon âme frère, le plus précieux soutien qui n'a pas besoin de beaucoup pour me comprendre. Ma famille qui m'épaule et m'a toujours poussé à accomplir mes rêves, mon père, ma mère et mon frère, je vous aime. Pour finir, merci à toi Camille pour tout ce que tu m'apportes au quotidien depuis plus de 5 ans. Après le stage et la thèse, il est temps de partager notre vie.

# Résumé en français

Cette partie est un résumé étendu en français, donnant le contexte et les objectifs des travaux, les principaux résultats et conclusions de chaque chapitre, ainsi que les principales perspectives. Pour accéder à l'intégralité des travaux, le lecteur est prié de se référer au reste du manuscrit, rédigé en anglais.

## Contexte industriel et scientifique

La production du secteur sidérurgique, en perpétuelle croissance (deux milliards de tonnes d'acier produites en 2020), est responsable d'environ 8 % de la demande énergétique finale mondiale et de 7 % des émissions de $CO_2$ du secteur énergétique. L'efficacité énergétique reste donc une priorité absolue, car elle permet de réduire les coûts de production et d'améliorer la compétitivité. Le charbon est la première source d'énergie en sidérurgie ; l'électricité et le gaz naturel représentent la majeure partie du reste de la demande énergétique, en majorité pour alimenter les fours à arc électrique et les fours à induction.

Les propriétés physiques et mécaniques des matériaux, généralement polycristallins et multiphasés, sont directement liées à leur microstructure, en particulier à la structure des grains et à la disposition spatiale des phases. Pour contrôler et optimiser leurs propriétés, on utilise un ou plusieurs traitement(s) thermique(s) ou thermomécanique(s), qui combine(nt) communément une déformation plastique (forgeage, laminage, etc.) et un traitement thermique (traitement thermique, trempe à l'eau, etc.), parfois en un seul processus. Les variations microstructurales se produisent souvent à travers les transformations de phases ou la restauration et la recristallisation des matrices métalliques qui éliminent les dislocations. Les fours radiatifs sont habituellement utilisés pour effectuer des traitements thermiques, en fournissant de la chaleur par convection ou rayonnement. Cependant, il s'agit de processus très

énergivores et chronophages, qui peuvent entraîner une perte d'énergie importante pendant les étapes de chauffage et de refroidissement. De nos jours, le chauffage par effet Joule est de plus en plus utilisé lors des différents traitements thermiques et des processus de mise en forme des matériaux en métallurgie. L'utilisation de l'électricité pour le chauffage direct présente de nombreux avantages : un contrôle précis des cinétiques de chauffage et de refroidissement, une régulation fine de la température et une grande reproductibilité des conditions de chauffage, ainsi qu'un chauffage sélectif pour ne chauffer que la partie souhaitée du matériau. Le chauffage par effet Joule se retrouve dans plusieurs techniques, aujourd'hui couramment utilisées dans le domaine de la métallurgie, comme le soudage par résistance électrique, le frittage par activation par courant électrique et le chauffage par induction.

Jusqu'à récemment, les traitements thermiques assistés par courant électrique étaient considérés comme équivalents aux méthodes de chauffage conventionnelles. Paradoxalement, il a été démontré que les courants élevés peuvent influencer le comportement des métaux et des alliages, par exemple l'effet du courant sur la vitesse de croissance des couches intermétalliques, les réactions de précipitation et de dissolution, et la cinétique de restauration et de recristallisation des métaux déformés. Cependant, la plupart des explications de tous ces effets considèrent l'interaction entre les électrons et les défauts métalliques, tels que les lacunes et les dislocations, d'une manière qualitative et sans aucun fondement sur une théorie quantitative.

L'**ÉlectroMiGration** (abrégé en EMG par la suite) est un mécanisme de transfert de masse observé dans les métaux lorsque des densités de courant électrique élevées les traversent. Le modèle couramment utilisé pour décrire le transfert de masse dû à l'EMG suppose que deux forces affectent les atomes d'un matériau conducteur lorsqu'un courant électrique est appliqué : la force électrostatique directe dans le sens du courant, et la force résultant du transfert de quantité de mouvement dû aux collisions des atomes avec des électrons se déplaçant dans le sens opposé. L'équilibre, ou la compétition, entre ces deux forces est caractérisée par la **charge effective** $Z^*$.

Dans ce projet, nous nous concentrons sur le système Fe-C pour analyser comment un courant électrique peut influencer la diffusion du carbone (C), ainsi que la cinétique de transformation de phases ferrite-austénite ($\alpha/\gamma$). Premièrement, le système Fe-C a été choisi en raison de son intérêt industriel évident, parce que sa

thermodynamique et ses propriétés de diffusion sont bien connues et parce que la cinétique de la transformation austénite-ferrite a déjà été étudiée en détail dans la littérature. Deuxièmement, l'influence d'un champ électrique sur la diffusion du C a déjà été étudiée dans des monophases de fer (ferrite et austénite). En effet, en analysant la distribution de C à l'état d'équilibre, les auteurs ont pu mesurer quantitativement la charge effective $Z^*$. Celle-ci dépend fortement des conditions expérimentales (température, densité de courant, phase). De plus, aucune valeur de $Z^*$ n'a encore été déterminée dans le domaine intercritique avec le changement de phases dans le fer.

## Organisation du manuscrit

Cette thèse démarrée en 2018 s'inscrit dans le cadre du projet ECUME (interactions of Electric CUrrents and Microstructures Evolutions), soutenu par une subvention de l'Agence Nationale de la Recherche (ANR-18-CE08-0008). Nous avons mené des expériences axées sur la détermination de l'impact d'un courant appliqué sur la diffusion des atomes de carbone dans le fer et sur la transformation de phases ferrite-austenite. L'objectif est de décrire et de comprendre les évolutions microstructurales du système Fe-C au cours d'une étape de maintien isotherme par chauffage Joule avec un courant électrique continu ou pulsé. Le manuscrit de thèse est composé de 4 chapitres :

1. Le **Chapitre 1** propose un état de l'art des évolutions microstructurales survenant lors du traitement électrique des matériaux métalliques. Il décrit les théories du transfert de masse induit par l'électricité, les mécanismes de diffusion dans les métaux, les transformations de phases allotropiques du fer et leur modélisation. La revue de la littérature se termine par des discussions sur les travaux autour des effets du courant électrique sur les transformations de phases.
2. Le **Chapitre 2** décrit l'état initial du matériau (fer ARMCO) utilisé au cours de cette thèse, les méthodes expérimentales et les installations utilisées pour les traitements thermiques ainsi que les méthodes de caractérisation des échantillons. Ce chapitre introduit également le modèle de diffusion du C prenant en compte la transformation de phases $\alpha/\gamma$ et l'électromigration du C dans le fer. L'étude de sensibilité des paramètres du modèle est utilisée pour mettre

en place une méthode permettant d'identifier les paramètres diffusionnels et d'électromigration en partant des résultats expérimentaux.

3. Le **Chapitre 3** est consacré à la détermination de l'influence du courant continu sur la cinétique de transformation $\alpha/\gamma$. La diffusion du C dans le fer ARMCO a été étudiée dans le domaine intercritique. Des traitements thermiques ont été réalisés avec et sans courant électrique. Les microstructures des échantillons ont été caractérisées afin de révéler la position des fronts de changement de phases et les profils de concentration en C. Des simulations numériques ont été menées afin d'identifier les principaux paramètres du modèle et de modéliser les phénomènes induits par le courant électrique.
4. Le **Chapitre 4** étudie l'influence possible du courant pulsé, comparée à celle d'un courant continu, sur l'électromigration du C et sur la cinétique de transformation de phases $\alpha/\gamma$. Pour une température donnée, la comparaison est faite pour le même effet Joule induit par le courant pulsé ou continu.

# Chapitre 1 : État de l'art

L'effet d'un courant électrique sur le système Fe-C implique principalement l'électromigration du C dans le réseau du fer. L'équation de diffusion (1) décrit l'évolution de la concentration en C rendant compte de ce phénomène (notations explicitées en section 1.1). Le flux atomique induit par la présence du courant électrique est décrit par une vitesse de dérive $v_d$ (Équation 2). Les principaux paramètres à considérer sont le coefficient de diffusion $D$ et la charge effective $Z^*$ du C dans le fer.

$$\frac{\partial C}{\partial t} = [\frac{\partial \mu^0}{\partial x} + F\frac{\partial (Z^*\phi)}{\partial x})]\frac{D}{RT}\frac{\partial C}{\partial x} + D\frac{\partial^2 C}{\partial x^2} \tag{1}$$

$$v_d = \frac{DZ^*}{RT}F\rho j \tag{2}$$

Le fer subit une transition allotropique d'une structure cubique centrée (ferrite ou Fe-$\alpha$) à une structure cubique à faces centrées (austénite ou Fe-$\gamma$) à 736 °C. Parmi les différents outils de modélisation disponibles dans la littérature, le modèle de minimisation de l'énergie de Gibbs (GEM) permet de facilement décrire la transformation de phases $\alpha/\gamma$ et l'électromigration du C dans le fer (grâce à la vitesse de dérive dans l'équation de diffusion). L'influence d'un champ électrique sur la

diffusion de C a déjà été étudiée dans les phases du fer, à la fois dans la ferrite et dans l'austénite. Cependant, la charge effective du C reste à déterminer dans le cas d'une transformation de phases. En fait, il est important de considérer que le courant électrique est déjà utilisé dans l'industrie pour les traitements thermiques du fer et des aciers dont la transformation de phases est minutieusement contrôlée.

## Chapitre 3 : Effet du courant électrique continu

Ce chapitre avait pour but d'étudier l'électromigration du C liée à la transformation de phases dans le fer soumis à un courant électrique continu. Les traitements thermiques ont été réalisés dans un four AET avec deux sources de chauffage (rayonnement et chauffage par effet Joule) afin de ne pas corréler le niveau de température avec le courant électrique, à trois niveaux de température différents (775 °C, 825 °C et 875 °C) dans le domaine intercritique. Ils ont d'abord été réalisés sans courant électrique, puis avec des densités de courant intermédiaire ($\sim 310\,\mathrm{A\,cm^{-2}}$) et plus élevée ($382\,\mathrm{A\,cm^{-2}}$). La plupart des expériences ont consisté en un maintien isotherme de 7 h. Néanmoins, des traitements plus courts ont également été réalisés afin de comparer les évolutions de la microstructure après 1 h, 3 h and 5 h. Ces derniers essais ont été réalisés sans courant électrique et avec une densité de courant maximale ($382\,\mathrm{A\,cm^{-2}}$).

Le modèle a montré que la transformation de phases ferrite-austénite dépend principalement de la diffusion du carbone dans l'austénite et de son coefficient $D_\gamma$. Comme attendu, elle est plus rapide pour une température plus élevée puisque la diffusion est un phénomène thermiquement activé. Grâce à l'électromigration, la distance de diffusion du C est augmentée en présence de courant électrique. En nous basant sur les positions finales des interfaces $\alpha/\gamma$, nous avons conclu que la cinétique de transformation de phases est plus rapide du côté de l'anode, dans la direction du courant électrique. Elle est freinée dans la direction opposée, du côté de la cathode. Une densité de courant plus élevée augmente cette différence de cinétique.

L'objectif du modèle développé dans ce travail était de déterminer les valeurs de $D_\gamma$ et $Z^*_\gamma$ sur la base de nos résultats expérimentaux. Le coefficient de diffusion du C dans l'austénite $D_\gamma$ est croissant avec la densité de courant électrique, pour un même niveau de température de traitement thermique. La charge effective du C

dans l'austénite $Z_\gamma^*$ dépend de la température et de la densité de courant électrique. Elle est égale à +24/+18/+36 pour une densité de courant continu de $\sim 310\,\mathrm{A\,cm^{-2}}$ à respectivement 775 °C, 825 °C et 875 °C. Sa valeur diminue pour une densité de courant plus élevée, puisque $Z_\gamma^*$ est de +16/+12/+16 à 775 °C, 825 °C et 875 °C pour $382\,\mathrm{A\,cm^{-2}}$ en courant continu. Nos simulations et nos résultats expérimentaux sont en accord pour les trois niveaux de température considérés dans le domaine intercritique, en termes de prédiction de la cinétique de transformation de phases $\alpha/\gamma$ et de la distribution de concentration en C qui en résulte.

La dépendance en température de $D_\gamma$ a été étudiée en tenant compte de nos expériences. Nous avons constaté que l'énergie d'activation pour la diffusion du C dans l'austénite diminue en présence d'un courant continu, passant de (2,06 ± 0,30) eV sans courant électrique à (1,03 ± 0,31) eV avec $310\,\mathrm{A\,cm^{-2}}$. L'augmentation de la densité de courant ($382\,\mathrm{A\,cm^{-2}}$) conduit à une barrière énergétique plus élevée (1,27 ± 0,07) eV. Comme la probabilité de collisions entre les électrons et les atomes de C augmente, la diffusion du C dans l'austénite est plus difficile dans le sens du courant électrique. Ceci est relié aux charges effectives $Z_\gamma^*$ plus faibles pour nos expériences impliquant les densités de courant les plus élevées. Cependant, nous n'avons pas pu associer ces énergies d'activation avec un mécanisme spécifique d'électromigration du C (supposé être interstitiel comme la diffusion thermique).

## Chapitre 4 : Influence de la nature du courant : pulsé ou continu

Ce chapitre visait à comparer l'effet du courant continu pulsé et du courant direct/continu, à la fois sur l'électromigration du C et sur la transformation de phases dans le fer. Les traitements thermiques ont été réalisés dans un appareil de frittage flash (*Spark Plasma Sintering* (SPS) en anglais) aux trois mêmes niveaux de température (775 °C, 825 °C ou 875 °C) dans le domaine intercritique. Les expériences ont consisté en un maintien isotherme de 7 h.

Comme il était attendu, la transformation de phases ferrite-austénite est plus rapide à haute température puisque la diffusion est un phénomène thermiquement activé. Grâce à l'électromigration, la profondeur de diffusion du C est augmentée en présence d'un courant électrique pulsé. Comme les résultats précédents avec le courant continu, la diffusion est plus rapide dans le sens du courant électrique et elle

est freinée dans le sens opposé, respectivement du côté de l'anode et de la cathode, quelle que soit la nature du courant électrique. Une densité de courant plus élevée augmente cette différence de cinétique. Cependant, elle est plus prononcée avec le courant pulsé qu'avec le courant continu.

Grâce au modèle développé prenant en compte l'électromigration du C dans le fer et la transformation de phases ferrite-austénite, les valeurs de $D_\gamma$ et $Z^*_\gamma$ pour le courant pulsé ont été déterminées à partir de nos résultats expérimentaux. Pour une température donnée, le courant pulsé a été modélisé par le courant continu induisant le même effet Joule (par la moyenne quadratique de la densité de courant). Le coefficient de diffusion du C dans l'austénite $D_\gamma$ est toujours plus élevé pour le courant pulsé pour le même niveau de température de traitement thermique. La charge effective du C dans l'austénite $Z^*_\gamma$ est également plus élevée pour le courant pulsé que pour le courant continu à 825 °C et 875 °C. Il existe un bon accord entre nos simulations et les résultats expérimentaux pour les trois niveaux de température considérés dans le domaine intercritique, en termes de prédiction de la cinétique de transformation de phases $\alpha/\gamma$ et de la distribution de concentration en C qui en résulte. Cependant, la relation entre la nature du courant électrique utilisé et la valeur de la charge effective reste absconde. La cinétique expérimentale et la distribution du C n'est pas décrite par un couple unique de paramètres du modèle. Le phénomène d'électromigration est favorisé par une augmentation de la température et de la densité du courant électrique. Or, dans la machine SPS, le niveau de température est ajusté en faisant varier la densité de courant. Ainsi, il est difficile de distinguer l'influence du vent d'électrons et de l'échauffement Joule local dans le cœur des échantillons pour ces essais.

La dépendance en température de $D_\gamma$ identifiée pour rendre compte de nos expériences a été étudiée. Nous avons constaté que l'énergie d'activation pour la diffusion du C dans l'austénite est similaire pour le courant continu et le courant pulsé, puisque sa valeur est de (1,03 ± 0,31) eV et (1,13 ± 0,25) eV avec 310 $\mathrm{A\,cm^{-2}}$ respectivement en courant continu et en courant pulsé. Ainsi, la cinétique de transformation de phases $\alpha/\gamma$ plus rapide avec le courant pulsé n'est pas due à une barrière énergétique plus faible. Elle proviendrait plutôt de la densité de courant électrique plus élevée des impulsions induisant une électromigration plus rapide du C dans le fer. Malheureusement, ces observations n'ont pas permis d'identifier le mécanisme d'électromigration du C lors de l'utilisation d'un courant pulsé ou continu.

# Perspectives : approfondir le travail expérimental de l'électromigration du C dans le fer

Pour poursuivre cette étude, plusieurs voies peuvent être explorées pour compléter et approfondir la caractérisation et la modélisation des évolutions microstructurales du système Fe-C lors d'une étape de maintien isotherme par chauffage Joule.

Le fer ARMCO n'était pas le matériau modèle idéal pour l'étude complexe de l'électromigration du C dans le fer. Les impuretés (C, Mn, P, S) ne sont pas négligeables si l'on souhaite étudier la carburation du fer pur. Le premier défi est de développer des échantillons modèles pour observer le rôle des différents types de défauts sur l'électromigration. Du fer pur ou des alliages binaires Fe-C pourraient être élaborés tout en contrôlant la concentration en impuretés (C, S, O, N $< 0{,}0005$ %) et la microstructure initiale (la taille des grains, le caractère monophasé ou biphasé ou les grains colonnaires). Des échantillons austénitiques (avec du nickel et du chrome) pourraient également être utilisés pour étudier spécifiquement l'électromigration du C dans l'austénite sans changement de phases. Cela permettrait de vérifier nos valeurs de diffusivité du C dans l'austénite, avec et sans courant électrique.

L'influence de la taille des grains sur la diffusion et l'électromigration du C dans le fer a déjà été explorée au cours de cette thèse. Des expériences de carburation ont été effectuées en utilisant des échantillons fabriqués à partir d'une barre de fer brut (pureté de 99,8 %) provenant de *Goodfellow* (désigné par la suite comme fer NON-ARMCO). La microstructure initiale était très différente de celle des échantillons de fer ARMCO. Ils présentaient notamment une granulométrie plus fine et des inclusions visiblement plus grandes, comme le montre la Figure 1.

Après un traitement de carburation dans le domaine intercritique avec un courant électrique continu (à 875 °C pendant 1 h avec 382 A cm$^{-2}$), les microstructures obtenues après refroidissement sont très différentes. Les deux échantillons présentent des grains entièrement perlitiques dans les premiers 120 µm à partir du bord de l'électrode. Ensuite, la distribution de la perlite dans le mélange de perlite et de ferrite n'est pas la même. L'échantillon NON-ARMCO a des grains plus petits et la position de l'interface $\alpha/\gamma$ n'est pas aussi clairement identifiable que dans l'échantillon ARMCO. De plus, les joints de grains parallèles à la direction du courant électrique semblent être des chemins préférentiels pour la diffusion du C. De la perlite se forme aux joints de grains dans tout l'échantillon.

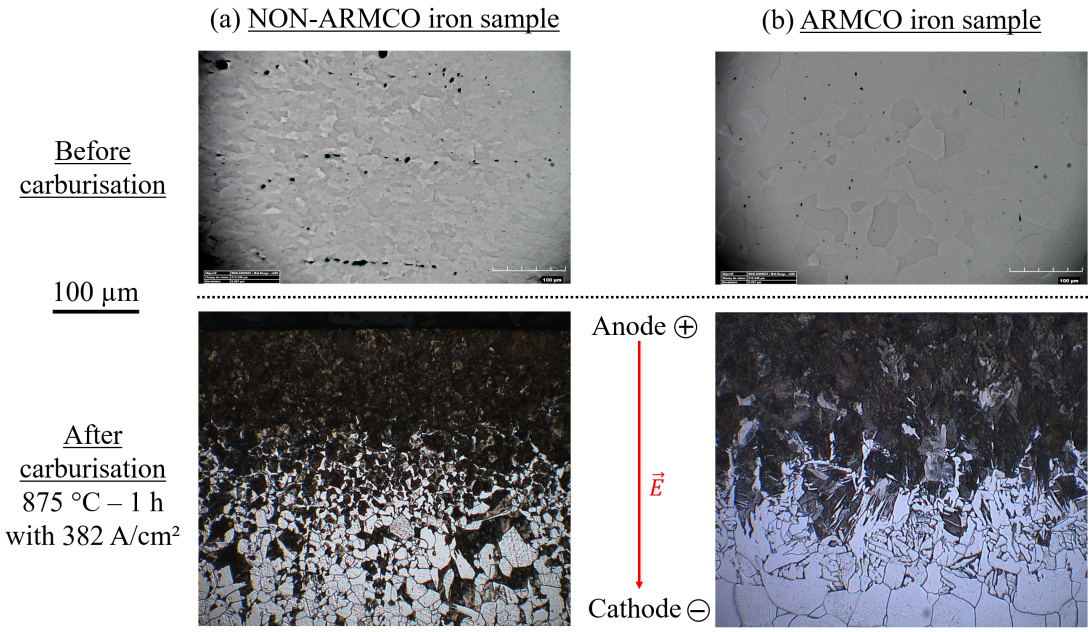


Figure 1: Micrographies optiques des microstructures avant et après 1 h de carburation à 875 °C avec 382 A cm$^{-1}$. (a) L'échantillon de fer NON-ARMCO à gauche, comparé à (b) l'échantillon de fer ARMCO à droite.

Nous supposons que le C a rapidement diffusé et saturé les joints de grains. Cependant, la taille du grain est principalement déterminée par l'énergie du joint de grain et le changement d'enthalpie de la ségrégation du joint de grain [LIU 04]. La croissance des grains est défavorable lorsque les joints de grains sont saturés. Ainsi, la croissance des grains d'austénite peut être limitée en raison de la saturation de leurs joints. Une modélisation de la diffusion du carbone en 2D est nécessaire pour rendre compte de ce phénomène. Il serait même possible d'étudier la relation entre l'orientation du joint de grain et la direction du courant électrique. Ce dernier peut fortement accélérer la diffusion du C à travers les joints de grains et précipiter leur saturation.

Pour mieux comprendre la diffusion du C dans le fer et la cinétique de transformation de phases, des expériences de carburation pourraient être couplées à des mesures par Diffraction aux Rayons X *in situ* (au synchrotron). La transformation de phases peut être suivie grâce à la transition cc vers cfc. Le profil de concentration en C peut être mesuré car il induit une distorsion du réseau cristallin et donc un changement du paramètre de maille. D'une part, les mesures macroscopiques du champ moyen permettraient de suivre la transformation des phases de fer pendant

les expériences. D'autre part, des mesures microscopiques sur des échantillons à gros grains peuvent être réalisées pour différencier la diffusion inter- et intra-granulaire du C. Les résultats de ces expériences, avec et sans courant électrique, seraient utilisés pour identifier les paramètres d'électromigration grâce au modèle développé dans ce travail de thèse.

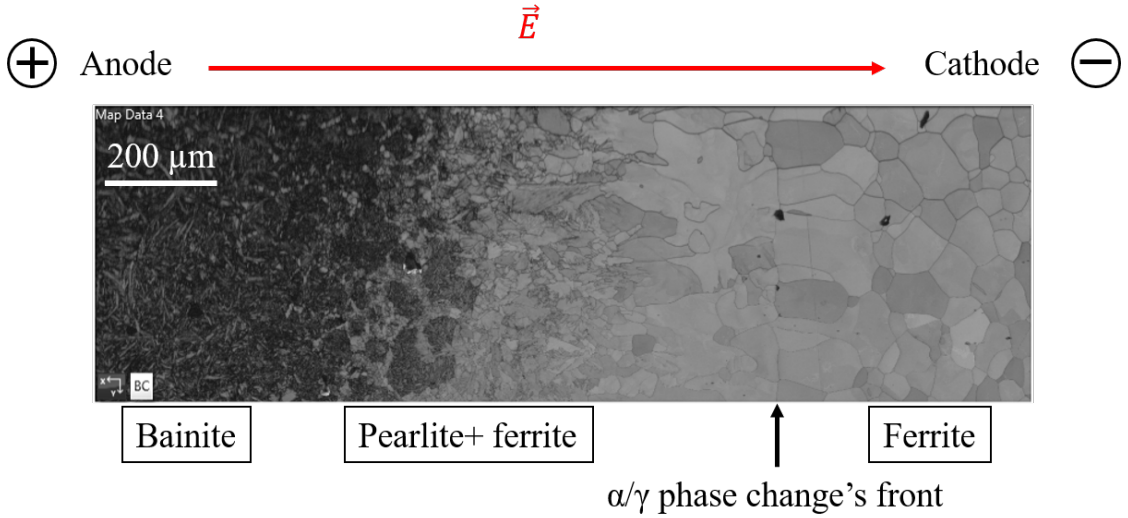


Figure 2: Métallographie de la microstructure de l'échantillon, dans la direction perpendiculaire à celle de diffusion du C, après un traitement thermique dans la machine de Test Electro-Thermo-Mécanique à 875 °C pendant 1 h avec $10^3$ A cm$^{-2}$.

En novembre 2019, des expériences préliminaires ont été réalisées à l'*European Synchrotron Radiation Facility*, (sans faisceau d'électrons). Elles ont montré que des conditions expérimentales appropriées peuvent être atteintes : température de 700 °C to 950 °C et densités de courant jusqu'à $10^3$ A cm$^{-2}$. Le dispositif expérimental utilisé était la machine ETMT (Test Électro-Thermo-Mécanique), dédiée à l'étude du changement de phases sous contrainte mécanique lors de traitements thermiques *in situ* suivis par la diffraction des rayons X. L'échantillon est chauffé grâce à l'effet Joule induit par un courant continu. L'analyse de la microstructure de l'échantillon après le traitement thermique à 875 °C pendant 1 h par chauffage par effet Joule avec $10^3$ A cm$^{-2}$ dans la Figure 2 montre que :

1. la diffusion du C a induit une transformation de phases
2. le volume transformé est suffisamment important par rapport au volume analysé
3. les tailles de grains permettent une statistique suffisante pendant l'acquisition.

La microstructure observée est similaire à celles présentées dans cette thèse, avec un gradient visible de concentration en C traduit par l'évolution microstructurale de la perlite à la ferrite. De manière surprenante, proche de l'anode, nous avons également identifié de la bainite formée lors du refroidissement rapide de l'échantillon après traitement. Près du front du changement de phases $\alpha/\gamma$ (identifié par une flèche), il est également intéressant de noter la présence de grains de ferrite assez gros avec une morphologie colonnaire dans la direction du courant électrique. Nous supposons que cela peut être dû à la présence du courant électrique. La saturation en C des joints de grains parallèles à la direction du courant pourrait conduire à cette croissance anormale.

Cependant, de forts gradients de température ont également été observés dans les échantillons pendant les tests. Ils étaient dus à l'échauffement important des feuilles de graphite lors du passage du courant de $10^3\,\mathrm{A\,cm^{-2}}$, provoquant un échauffement supplémentaire par rayonnement. Ce phénomène pourrait être limité en utilisant des feuilles plus fines ou de la colle graphite. Des sections d'échantillons plus petites permettraient également d'obtenir une température plus homogène. Une autre solution serait d'utiliser des plaques en céramique, comme bouclier thermique, pour réduire ou éliminer les rayonnements parasites.

# Contents

**Liste des ecoles doctorales** i

**Remerciements** v

**Résumé en français** ix

**Contents** xxi

**List of Figures** xxvii

**List of Tables** xxxiii

**Introduction** xxxv

**1 State of the art** 1

1.1 The electromigration phenomenon . . . . . 3

1.1.1 Diffusion in solid crystals . . . . . 3

1.1.2 Diffusion under external forces . . . . . 5

1.1.3 Diffusion in the presence of an electric current . . . . . 7

1.2 Iron allotropic phase transformations . . . . . 10

1.2.1 Allotropes of iron . . . . . 10

1.2.2 Modelling tools for phase transformation . . . . . 11

1.2.2.1 Phenomenological approach . . . . . 12

1.2.2.2 Physically based modelling . . . . . 13

1.3 Effect of electric current on microstructural transformations in metals 16

1.3.1 Effect on InterMetallic Compound (IMC) growth . . . . . 16

1.3.2 Effect on recovery and recrystallization . . . . . 18

1.4 Effect in the Iron-Carbon system . . . . . 19

1.5 Conclusions . . . . . 20

**2 Material and methods** **23**

2.1 Experimental strategy . . . . . 24
2.1.1 Material: ARMCO iron . . . . . 24
2.1.2 Heat treatments performed . . . . . 25
2.2 Experimental techniques . . . . . 26
2.2.1 Sample preparation before heat treatment . . . . . 26
2.2.2 Thermal treatments . . . . . 26
2.2.2.1 Spark Plasma Sintering (SPS) . . . . . 26
2.2.2.2 AET furnace . . . . . 29
2.2.3 Sample characterisation . . . . . 32
2.2.3.1 Sample preparation for metallography . . . . . 32
2.2.3.2 Optical microscopy (OM) . . . . . 32
2.2.3.3 Microhardness indentation . . . . . 36
2.2.3.4 Electron Probe MicroAnalysis (EPMA) . . . . . 37
2.3 Model and simulation . . . . . 38
2.3.1 Carburisation simulation configuration . . . . . 38
2.3.2 Example of results from the model . . . . . 42
2.3.3 Model parameters sensitivity study . . . . . 44
2.3.4 Key points . . . . . 47

**3 Effect of continuous electric current** **49**

3.1 Experimental ferrite-austenite phase transformation kinetics in the intercritical domain . . . . . 51
3.1.1 7-hour isothermal holding treatments . . . . . 51
3.1.2 Kinetics study of carburisation at 875 °C . . . . . 56
3.2 Comparison between simulation and experimental results . . . . . 57
3.2.1 Numerical ferrite-austenite phase transformation kinetics . . . 57
3.2.2 C concentration profiles . . . . . 63
3.3 Discussion . . . . . 65
3.3.1 Determination of activation energy of C thermal diffusion in austenite . . . . . 65
3.3.2 C diffusion in austenite with electric current . . . . . 67

3.3.2.1 Determination of activation energy of C diffusion in austenite with DC current . . . . . 67
3.3.2.2 Mechanism of electromigration of C in iron during ferrite-austenite phase transformation . . . . . 69
3.4 Conclusions . . . . . 70

**4 Electric current's nature effect: Pulsed vs. Direct Current 73**
4.1 Experimental conditions and results . . . . . 74
4.2 Comparison between simulation and experimental results . . . . . 77
4.2.1 Numerical ferrite-austenite phase transformation kinetics . . . 77
4.2.2 C concentration profiles . . . . . 79
4.3 Discussion . . . . . 86
4.4 Conclusions . . . . . 89

**Conclusions and Perspectives 93**

**A Demonstration of equations for C diffusion in Fe in presence of electric current 101**

**References 105**

# List of Abbreviations

| | |
|---|---|
| AC | Alternating Current (continuous) |
| DC | Direct Current (continuous) |
| EDXS | Energy-Dispersive X-ray Spectroscopy |
| EMG | Electromigration |
| EPMA | Electron microProbe MicroAnalysis |
| GEM | Gibbs Energy Minimization |
| IH | Induction Heating |
| IMC | Intermetallic compounds |
| RMS | Root Mean Square |
| PDC | Pulsed Direct Current |
| SEM | Scanning Electron Microscopy |
| SPS | Spark Plasma Sintering |
| XRD | X-Ray Diffraction |

# List of Figures


1 Micrographies optiques des microstructures avant et après 1 h de carburation à 875 °C avec 382 A cm$^{-1}$. (a) L'échantillon de fer NON-ARMCO à gauche, comparé à (b) l'échantillon de fer ARMCO à droite. xvii

2 Métallographie de la microstructure de l'échantillon, dans la direction perpendiculaire à celle de diffusion du C, après un traitement thermique dans la machine de Test Electro-Thermo-Mécanique à 875 °C pendant 1 h avec $10^3$ A cm$^{-2}$. . . . . xviii

3 Energy consumption in steel industry. From the Iron and Steel Technology Roadmap, International Energy, 2020) [BUD 20]. . . . . xxxvi

4 Schematic representation of electromigration in a conductor. $F_{direct}$ is the direct electrostatic force, $F_{wind}$ is the wind force and orange circles represent electrons. . . . . xl

5 (a) Plot of effective charge of carbon in ferrite, $Z^*_\alpha$, vs. temperature T, at different electric current densities (represented with a color scale). (b) Plot of effective charge of carbon in austenite, $Z^*_\gamma$, vs. electric current density ($1 \times 10^2$ to $3 \times 10^3$ A cm$^{-2}$), at different temperature levels (represented with a color scale). The dotted curves are a guide for the eyes, data from Okabe *et al.* [OKA 70, OKA 73], Nakajima *et al.* [NAK 77, NAK 78], Falquero and Youdelis [FAL 70]. . . . . xliv

1.1 Point defects in crystal structures. (figure created under Creative Commons license) . . . . . 3

1.2 Schematic of potential energy in a crystal (a) without any force (b) under an external force. . . . . 6

1.3 The interface of the Al/Ni couple annealed at 400 °C for 336 h (a) without passage of electric currents (b) with the passage of a $10^3$ A cm$^{-2}$ electric current. . . . . 17

1.4 Self-diffusion coefficients of iron phases in their solid state, with the intercritical domain filled in orange (736 to 911 °C = 1009 to 1184 K) [MEH 07]. . . . . 19

2.1 Optical micrograph of the as-received ARMCO iron microstructure (colloidal suspension final polishing). Ferrite grains heterogeneous in size and small (MnS, MnO) inclusions are observed. . . . . 24

2.2 (a) Schematic Iron-Carbon phase diagram. The boundary condition $C_0$ of the C concentration at the interface is determined by the equilibrium concentration between C and Fe at a given temperature $T$. The intercritical domain of temperature $Ae_1 < T < Ae_3$ is filled in orange. (b) Thermal cycle used to study the electromigration of C in ARMCO iron during the ferrite-austenite phase transformation. . . . 25

2.3 Principle of carburisation during SPS thermal treatment with phase transformation inside an ARMCO iron sample. The cross-section of an ARMCO iron ring is represented (vertical axis symmetry) and stretched for more clarity. C concentrations $C_0$, $C_1$ and $C_2$ are linked to the Fe-C phase diagram (Figure 2.2(a)). . . . . 27

2.4 (a) Overall picture of the AET furnace. (b) Vertical furnace: the sample is placed inside a quartz tube, in between two electrodes (anode and cathode) both in two parts made of two different materials, molybdenum and copper. The heating is obtained by radiation (symbolised by the small red arrows) with halogen lamps and/or *via* Joule heating with an external generator. (c) The sample made of ARMCO iron is glued with Papyex (graphite) sheets thanks to C-glue. Two type K thermocouples $T_{top}$ and $T_{bot}$ are inserted to measure the temperature in the sample's core. . . . . 29

2.5 (a) Electric cords connecting the lower electrode (anode) copper plate with the power supply. (b) Two braided wire leads connect each electrode with its copper plate. . . . . 30

2.6 Optical micrograph of a sample's cross-section (a) as polished; or (b) after Nital etching: pearlite (ferrite + cementite $Fe_3C$) appears black while ferrite is white. . . . . 33

2.7 (a) Optical micrograph after Nital etching: pearlite appears brown or black while ferrite is white. The result from thresholding this image is given in (b) where pearlite is black (grey value = 255) and ferrite is white (grey value = 0). . . . . 34

2.8 Typical result from phase quantification procedure using *Fiji*. The mean grey value profile allows to quantify the evolution of the fraction of pearlite with the depth of diffusion. . . . . 35

2.9 (a) Example of micro-hardness indentation along two staggered rows and (b) the hardness profile obtained. . . . . 36

2.10 Schematic carburisation simulation configuration with 2 migrating ferrite/austenite interfaces. . . . . 39

2.11 Ferrite-austenite phase transformation kinetics described by the displacement of the phase change's fronts (anode and cathode) over time. The dashed curves and the plain curves represent the simulated kinetics without electric current and with an electric current respectively. 43

3.1 Metallography of the sample microstructure perpendicular to the C diffusion direction after a thermal treatment in AET furnace at 875 °C for 7 hours (a) without electric current and (b) with $382\,\mathrm{A\,cm^{-2}}$. . . . 53

3.2 Plot of effective charge of carbon in austenite $Z^*_\gamma$ vs. electric current density ($1 \times 10^2$ to $1 \times 10^3\,\mathrm{A\,cm^{-2}}$), at different temperature levels (represented with a color scale). Data from Okabe *et al.* [OKA 70, OKA 73], Nakajima *et al.* [NAK 77, NAK 78], Falquero and Youdelis [FAL 70] are reported as hollow rings. The effective charges we determined based on our experimental results are plotted as solid stars (topped by an arrow). . . . . 59

3.3 Comparison of simulation predicted kinetics (curves) and experimental AET results (triangles) after 7 hours, from the anode and from the cathode. Results for heat treatments without electric current are displayed in black. Thicker lines are used to discriminate the anode's phase change front from the cathode's one. . . . . 62

3.4 Carbon concentration profiles from simulations of carburisation at 875 °C. Different linestyles are used to represent the profiles obtained at different times (1, 3 and 5 h). Black and red lines draw profiles without electric current and with an electric current density of 382 A cm$^{-2}$ respectively. . . . . 64

3.5 Temperature dependence of diffusion coefficient of carbon in austenite. $\ln(D_\gamma)$ is plotted versus $1/T$ to calculate the activation energy $Q$ as given in Equation 3.4. For three different carbon concentrations (0.1, 0.5 and 0.89 wt.% C), the curves plot the values predicted by Ågren (Equation 2.10) [ÅGR 86], while the dots are the values identified in our work with the associated linear regressions as dotted curves. . . . . 66

3.6 Activation energies of carbon (0.5 wt.% C) diffusion in austenite calculated in the case of DC current Joule heating. Data is displayed for the two electric current density ($\sim$ 310 and 382 A cm$^{-2}$) used during our experiments (Table 3.1) and compared with the values calculated for diffusion without electric current. . . . . 68

4.1 Metallography of the samples' microstructures perpendicular to the C diffusion direction after a thermal treatment at 825 °C for 7 h (a) with 296 A cm$^{-2}$ direct current and (b) with 293 A cm$^{-2}$ pulsed current (RMS values of current densities). . . . . 75

4.2 Comparison of simulation predicted kinetics (curves) and experimental results (triangles) after 7 h isothermal holding heat treatments with Pulsed Current (PDC) or Direct Current (DC), from the anode and from the cathode. Results for heat treatments without electric current are displayed in black. . . . . 80

4.3 Carbon concentration profiles from simulations of carburisation at 825 °C. Different coloured curves are used to represent the profiles obtained at different times (1 h, 3 h, 5 h and 7 h). Solid and dashed lines draw profiles with DC (in AET furnace) and PDC (in SPS machine) currents respectively. . . . . 82

4.4 Comparison of C profiles after 7 h of carburisation at 825 °C: from simulation (red curve), from phase quantification (brown curve) and from EPMA (brown square dots). Black diamonds are the microhardness measurements also used to observe qualitatively the evolution of the C concentration along the section. . . . . 84
4.5 Activation energies of carbon diffusion in austenite (0.5 wt.% C) calculated in the case of either continuous (DC) in orange or pulsed (PDC) current Joule heating in brown. They are compared with the values calculated for diffusion without electric current in blue. . . . . 87
4.6 Optical micrographs of the microstructures before and after 1 h carburation at 875 °C with 382 A cm$^{-2}$. (a) NON-ARMCO iron sample on the left hand side, compared to (b) ARMCO iron sample on the right hand side. . . . . 96
4.7 Metallography of the sample microstructure perpendicular to the C diffusion direction after a thermal treatment in ETMT machine at 875 °C for 1 h with $10^3$ A cm$^{-2}$. . . . . 98

# List of Tables


1.1 Characteristics of the iron crystal: structures and interstitial sites . . 11

2.1 Bulk composition of the ARMCO iron obtained by EPM and EDXS analyses . . . . . 24
2.2 Nominal values of model parameters (diffusion coefficients and effective charges). . . . . 42
2.3 Sensitivity coefficients of the model parameters (diffusion coefficients and effective charges) on the mean displacement value $\langle d \rangle$. . . . . 45
2.4 Sensitivity coefficients of the model parameters (diffusion coefficients and effective charges) on the difference of interfaces' displacement $\sigma_d$. 45

3.1 Experimental conditions of the heat treatments performed in AET furnace . . . . . 51
3.2 Experimental phase change front displacements ($\pm$ 40 µm) measured after 7 hours isothermal holding time heat treatments in the intercritical domain. $\langle d \rangle$ is the mean value of the fronts' displacement (Equation 3.1) and $\sigma_d$ is the difference between the anode and the cathode front displacements (Equation 3.2), in µm. . . . . 54
3.3 Experimental phase change front positions ($\pm$ 40 µm) measured after 1 to 7 hours isothermal holding time heat treatments at 875 °C. $\langle d \rangle$ is the mean value of the fronts' displacement (Equation 3.1) and $\sigma_d$ is the difference between the anode and the cathode front displacements (Equation 3.2), in µm. . . . . 56
3.4 Values of the model parameters that have been fitted from the results of heat treatments 7 hours isothermal holding time heat treatments at 775 °C, 825 °C and 875 °C. . . . . 57

3.5 Values of the model parameters that have been fitted from the results of 1 to 7 hours isothermal holding time heat treatments at 875 °C. . . 58

4.1 Experimental conditions of the 7-hour isothermal holding heat treatments performed with pulsed or continuous current. . . . . 74
4.2 Experimental phase change front positions measured after 7 h isothermal holding time heat treatments in the intercritical domain. $\langle d \rangle$ is the mean value of the fronts' displacement (Equation 3.1) and $\sigma_d$ is the difference between the anode and the cathode front displacements (Equation 3.2), in µm. . . . . 76
4.3 Values of the model parameters that have been fitted from the results of heat treatments 7 h isothermal holding time heat treatments at 775 °C, 825 °C and 875 °C with either pulsed or continuous electric current. . . . . 78
4.4 New values of model parameters ($D'_\gamma / D_{\text{Å}gren}$ and $Z^{*'}_\gamma$) with the new boundary condition $C'_0$. . . . . 83

# General introduction

## Industrial context

The iron and steel sector production (1,860 million tonnes in 2020) is energy- and emissions-intensive, responsible for about 8% of global final energy demand and 7% of energy sector $CO_2$ emissions [BUD 20]. While global steel production continues to grow, energy management systems try to ensure efficient use and recovery of energy throughout the steelmaking process. Since 1960, improvements in energy efficiency have led to reduction of about 60% in energy required to produce a tonne of crude steel. Energy constitutes up to 40% of the cost of steel production [RIZ 13]. Thus, improvements in energy efficiency are still a top priority as they result in reduced production costs and improved competitiveness. As shown in Figure 3, coal is the main energy input, accounting for almost three-quarters of the sector's energy use [HE 17]. Much of the coal consumed is coking coal used to produce coke for blast furnace-basic oxygen furnace, used for 75% of total steel production. Electricity and natural gas account for most remaining energy demand. Both of these energy carriers are used for a wide range of processes, including finishing processes, with a considerable proportion of the electricity used to power electric arc furnaces and induction furnaces.

Structural and functional materials are usually polycrystalline and multiphase materials. At macroscopic scale, their physical and mechanical properties are directly related to their microstructure, in particular to the grain structure and spatial arrangement of the coexisting phases. To control and optimize their properties, a thermal or thermo-mechanical treatment is used, which usually combines plastic deformation (forging, rolling, etc.) with thermal treatment (heat-treatment, water quenching, etc.), sometimes into a single process. The microstructural variations generally occur through the phase transformations or the recovery and recrystalli-

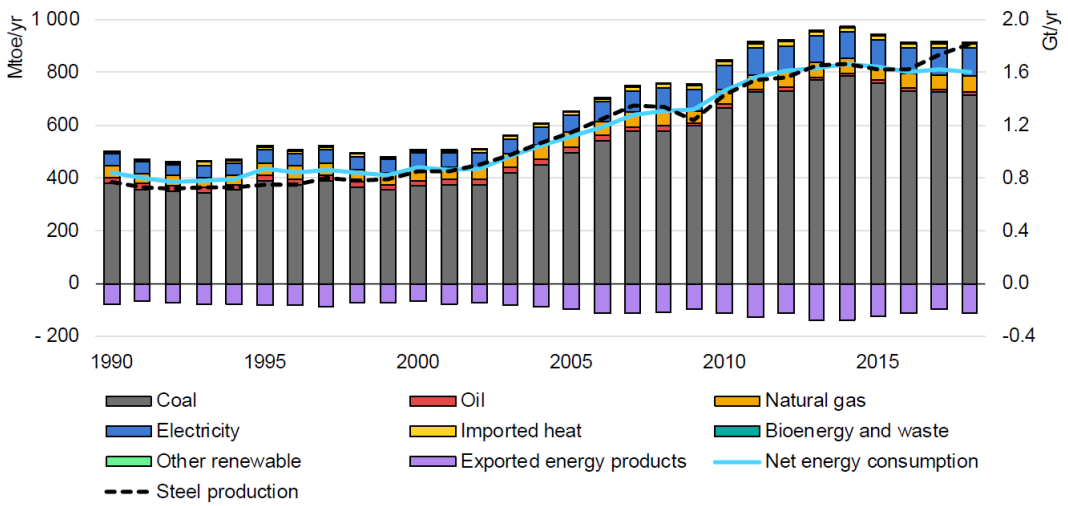


Figure 3: Energy consumption in steel industry. From the Iron and Steel Technology Roadmap, International Energy, 2020) [BUD 20].

sation of the metal matrices which eliminate the dislocations produced by hard working. Radiative furnaces are usually used to conduct heat treatments, providing heat (thermal energy) through convection or radiation. However, they are very time- and energy-consuming processes and may involve a large energy loss during the prolonged heating and cooling procedures. The energy management is a primordial question in manufacturing of materials. Nowadays, Joule heating is widely used during the different thermal treatments and material forming processes in metallurgy by a great diversity of techniques, such as resistance direct heating and electromagnetic induction heating. There are many advantages of using electricity for direct heating. The main benefit is the high control of the heating conditions. The heating and cooling kinetics are well controlled by adjusting the input electric power, which leads to a fine temperature regulation and a great reproducibility of heating conditions [OBE 99]. It also allows to heat only the desired part of the material and it induces less thermal inertia. The direct transformation of the electric power into heating power inside the material makes this method highly energy-efficient. The heating of metallic materials using electric current is found in several techniques now commonly used in the metallurgy domain.

**Electric resistance welding** This technique is widely used in manufacture of steel pipe and in assembly of bodies for cars. It is a welding process where metal parts in contact are permanently joined by heating them with an electric current (intensity between $10^2$ and $10^5$ A), melting the metal at the joint. It includes spot and seam welding, projection welding, flash welding and upset welding, different names for the same technology depending on the geometry of the weld and the method of applying pressure to the joint [NGU 15, ZHA 05]. It offers many advantages: a short heating time and a concentrated heat, which induces less deformation and stress in the small heat-affected area. The welding cost is low as it doesn't need either filler metals such as welding wire and electrode, or welding atmosphere such as oxygen, acetylene and hydrogen.

**Electric current activation sintering** This refers to various techniques such as Spark Plasma Sintering (SPS), Pulsed Electric Current Sintering, Field-Assisted Sintering Technique and Current-Activated Pressure-Assisted Densification [MUN 11]. These methods combine mechanical pressure with electric and thermal fields to enhance interparticle bonding and densification. Apart from the primary purpose to provide the required amount of resistive heat, the imposed electric currents may additionally enhance powder sintering by activating one or more concurring mechanisms, such as surface oxide removal, electromigration and electroplasticity [GRA 09]. A localised heat is concentrated at particle interfaces and serves to bond particles with each other. A massive heat promotes plastic deformation upon sintering. High heating rates (usually in the range from $10^2$ to $10^6\,\mathrm{K\,min^{-1}}$) can be advantageously used to reliably limit or even inhibit grain growth and therefore maintain fine-grained microstructures [BRA 20].

**Induction heating (IH)** This technique has a wide range of applications including (1) heat treating, (2) mass heating and (3) induction melting.

1. One of the most common applications of induction heat treatment is the hardening of steels, cast irons, and powder metallurgy materials. A typical hardening procedure involves heating the alloy to the austenitizing temperature range, holding it to form a fully or predominantly austenitic structure and then rapidly cooling/quenching to form martensite. It can be followed by additional heat treatments such as tempering and stress relieving, normalizing and annealing. IH allows short heat time for austenization (typically less

than 4 s) [RUD 17, BIE 21]. The precise, localized heating removes the need for "heat–cool" cycling. It results in low part distortion and also increased productivity.

2. Induction mass heating is used to heat various metallic materials to temperatures suitable for warm and hot forming (forging, upsetting, rolling, extrusion, bending, etc.) as well as pre-/postheating for coating operations [RUD 17]. High temperature uniformity or controlled temperature gradients are easily obtained by induction heating. The other major goal of IH is to provide the maximum production rate at which the metallic material can be processed. High powers (from hundreds to thousands of kilowatts) and relatively low frequencies (typically in the range from 50 to $3 \times 10^4$ Hz) are the most commonly used for induction mass heating.

3. Induction furnaces allow fast heating rate (over $100\,^{\circ}\mathrm{C\,s^{-1}}$), low thermal inertia and an easier metal melting under vacuum to obtain homogenous liquid metal baths [GAN 11]. They consist of a non-conductive crucible surrounded by a coil of copper wire. A strong alternating current flows through the latter, creating a reversing magnetic field that penetrates the metal. This induces eddy currents that heat the metal by Joule heating. Those circular currents also generate vigorous stirring of the melt, assuring a good mixing [RUD 17]. It is usually used for metal melting as a more clean, energy-efficient and well-controllable process compared to most other means of metal melting.

Until recently, thermal treatments assisted by electric current were considered equivalent to conventional heating methods. Paradoxically, it has been known for decades that large currents may influence the behaviour of metals and alloys [CON 00b, SPR 86]. Indeed, some studies have shown an effect of applied current on the growth rate of intermetallic layers [GAN 05], precipitation and dissolution reactions [CON 00a], variant selection, and recovery and recrystallisation kinetics of deformed metals [FAB 14]. It is worth emphasizing that the recent years have seen an increasing number of promising results on the refinement of microstructures in steels [LU 14, RAH 15b] and aluminium alloys [HAR 17, KIM 17]. However, most of the explanations of all these effects have considered the interaction between the electrons and the metal defects, such as vacancies and dislocations, in a qualitative manner without any strong support from any quantitative theory. Other theories have attempted to describe the mass transfer due to electric current in metals, known

as the ElectroMiGration (abbreviated as EMG thereafter). The most used model was first established for ionic liquids and solids. It was then extended to conductive materials, especially aluminium and copper in microelectronics.

## Brief definition and history of electromigration

In 1861, the French researcher Gerardin [GER 61] was the first to report observations of this phenomenon as he described the motion of atoms in molten salts under an applied voltage. For a number of years, it was thought that the effect did not occur in solid metals because it takes place at a much slower rate than in liquid metals. However, in the early 1930's a number of investigators experimentally demonstrated EMG in solid metals by using sufficiently high current densities and temperatures. Skaupy [SKA 14] introduced in 1914 the concept of "electron wind", which laid the foundation for the understanding of EMG. The electrons flow through a metal submitted to an electric current and collide with metal atoms, resulting in momentum transfer. In the 1950's, Seith and Wever [SEI 51] presented the first systematic studies of EMG based on the correlation between the direction of the current flow and the material transport. But it is only in the late 1960s that a real turn is made with the apparition of the first integrated circuits which operating time only lasted a few weeks. EMG is identified as the failure cause of Al networks carrying current densities up to $10^6\,\mathrm{A\,cm^{-2}}$. Thus, the interest and the direction of EMG studies have shifted their focus to investigate the EMG damage mechanisms and how to prevent them. This is still a topic of interest due to the decrease of the line sizes through scaling-down modern design, and due to the increase of current densities involved. The current densities are so high that EMG effects become spectacular; it displaces the copper and aluminium atoms, creating EMG-induced voids/hillocks formation [ABÉ 06].

The ElectroMiGration is a mechanism of mass transfer observed in metals when high electrical current densities are going through. It is also known as electrodiffusion or electrotransport. The model commonly used to describe the mass transfer due to EMG assumes that two forces affect the atoms $M$ in a conductive material when an electric current is applied (Figure 4):

- the direct electrostatic force $F_{direct}$ resulting of the direct action of the electric field $E$ on $M$ in the same direction as the electric current;

- the wind force $F_{wind}$ resulting of the momentum transfer due to collisions of $M$ with electrons moving in the opposite direction

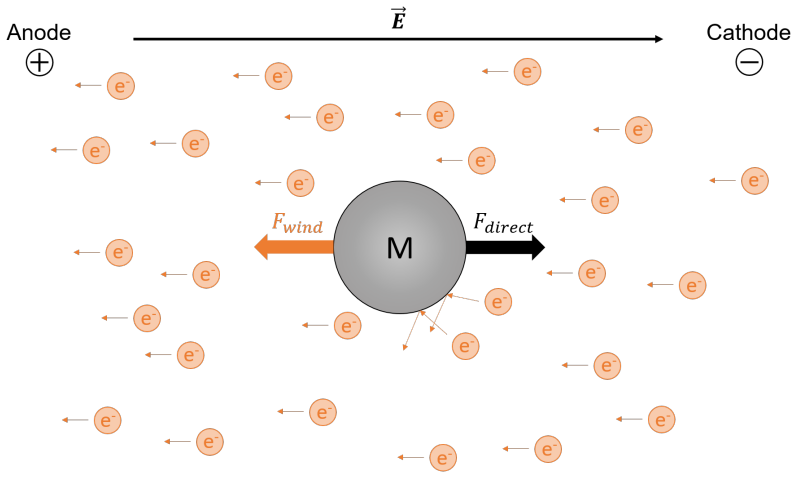


Figure 4: Schematic representation of electromigration in a conductor. $F_{direct}$ is the direct electrostatic force, $F_{wind}$ is the wind force and orange circles represent electrons.

The resultant force is written $F = eEZ^*$, where $e$ is the elementary charge ($1.602 \times 10^{-19}$ C), $E$ is the electric field intensity and $Z^*$ is the effective charge of metal atoms. The latter is one of the most important quantity to evaluate the magnitude of electromigration, as it sets the scale of the driving force resulting from the competition between the direct electrostatic force and the electron wind force. The direction of transport of component $i$ will be predicted by the sign of $Z^*$ in solid metals and dilute metallic alloys or solid solutions. A negative sign ($Z^* < 0$) indicates that the wind force predominates and the transport occurs towards the anode. A positive effective charge ($Z^* > 0$) means that the direct force is greater than the wind force and the transport is directed towards the cathode. It is important to understand that the equivalent charge in this model is not a realistic one but it is used to describe the effect of the different physical phenomena, which are not yet well understood.

## Electromigration in metallic alloys

The directional effects of EMG are easier to observe because the atomic diffusion often follows the direction of the electron flow or the electric current, depending on the

sign of $Z^*$. Chen *et al.* studied the electric current effects upon various interfacial reactions [CHE 00, CHE 98, SHE 18]. The passage of electric current ($5 \times 10^2\,\mathrm{A\,cm^{-2}}$) could either enhance or retard the growth of intermetallic compounds (IMC) in the Sn-Ag and Sn-Ni systems depending upon the flow direction of electrons. They determined the effective charge of tin to be $Z^*_{Sn} = -90$ even though Sn could welcome only 4 electrons (electronic configuration of Sn is [Kr] $4d^{10}\ 5s^2\ 5p^2$). Gan and Tu [GAN 05] also observed the effect of electromigration on kinetics of Cu-Sn IMC formation. With current densities from $4 \times 10^3$ to $4 \times 10^4\,\mathrm{A\,cm^{-2}}$ , the growth of the IMC layer was faster at the anode and hindered at the cathode, in comparison with the case without current. An acceleration of at least 125 % has been reported for the highest temperature and current density used.

Recent studies have shown that the electric current can induce lattice deformation [ZHA 08, LIN 17, VAL 03], electro-recrystallisation [CHI 13], grain rotation [WU 05], precipitation [CHE 00] and the alloy supersaturation effect [CHI 11]. These phenomena are not explained by the polarity of the electric current because the effects do not follow the direction of either the electron flow or the electric current. Several works [SHE 18, XIA 19, QIN 15] suggest that these phenomena might be due to the enhancement of dislocations mobility or the system Gibbs free energy modification. Many studies report a radical reduction of the deformation resistance and simultaneously a significant increase of the plasticity of various metals (Al, Cu, Ti, Ni, Fe) submitted to electrical pulses. This influence of the electric current pulses on the plastic flow is called the electroplastic effect [GUA 10]. The combination of Joule heating, drift electrons and residual stress may activate and enhance the movement of vacancies and dislocations, which accelerates the dislocation annihilation rates and leads to residual stress reduction inside the material.

Hence, despite the great potential of using electrical currents, both to monitor and to modify microstructure [BHA 15], a full application of electric methods of heating to a possible industrial scale requires a better basic understanding of the interactions between the electrical current and the microstructure evolutions [QIN 15]. The current state of knowledge relies essentially on estimates for ideal materials with no microstructure [ROS 87, GAL 16] on one hand, and on experimental evidences (e.g. [RAH 15a]) on the other hand. In any case, the interpretation of experimental observations is difficult, mainly because the experimental conditions do not always allow to distinguish the influence of the electron wind and the local Joule heating

in the core of the samples. Nevertheless, it is now clear that the electric current has a significant influence on the microstructure evolution in metals. All the physical phenomena induced by electric current are not fully understood, especially when phase change occurs during Joule heating. However, it opens new routes to tailor new microstructures and to improve the process productivity.

## Electromigration of C in iron and steels

Most thermal treatments of iron, ferrous alloys and steels imply heating in the intercritical domain or above, in which occurs the phase transformation of ferrite into austenite. To control and optimize their properties, a thermal or thermo-mechanical treatment is used. However, the transformations of the microstructure by application of intense electric currents are still not well understood.

The influence of the electric current on microstructural evolution in a ferritic-pearlitic 0.14%C steel has been investigated by Rahnama and Qin [RAH 15a]. They observed the effect of high electric current electropulsing treatments at ambient temperature. The initial lamellar structure of pearlite was first fragmented, and they witnessed the formation of new spheroidized cementite plates in the direction of electric current after further treatment. They measured an increase of the interlamellar spacing in pearlite, from 52 nm to 251 nm after 1000 pulses of electric current, consistent with a lower Vickers hardness, from 232 $HV_{10}$ to 181 $HV_{10}$. The authors explained the microstructural evolutions by the realignement of cementite plates with the current direction in order to present the lowest electrical resistivity, in addition to a lower Gibbs free energy in this configuration. Thermodynamical calculations [DOL 93] reaffirm a structural evolution in materials towards a state with lower electrical resistance caused by the electropulsing treatment. The authors also performed mechanical tests on electropulsed steel samples [RAH 15b]. The mechanical properties were affected by the electropulsing treatment, possibly due to the a lower vacancy and dislocation concentrations.

Lu *et al.* [LU 14] also studied the effect of electropulsing treatment on duplex stainless steel at high temperature. It was reported that the electropulsing promoted the decomposition of the stable $\delta$-phase that enables both the $\gamma$-phase and the $\sigma$-phase hard particles in the steel to survive and hence to strengthen it at high temperature. After quenching, the hardness of electropulsed sample was much

higher (472 HV) than the one that had not undergone an electropulsing treatment (316 HV). The modification of the fractions of equilibrium phases in steels due to electropulsing and changing Gibbs free energy might account for these observations.

There is a clear need for additional theoretical and experimental work to further evaluate the influence of electric fields and currents and the operative mechanisms in iron and steels. As expressed by Bhadeshia in a recent editorial [BHA 15] there is, in particular, a need for a theoretical framework that is quantitatively predictive for describing the electrical processing of materials.

In this project, we focus on the Fe-C system to analyze how an electric current can influence a diffusion process, as well as the kinetics of a phase transformation. First, the Fe-C system was chosen because of its obvious industrial relevance, because its thermodynamics and diffusion properties are well known and because the kinetics of the austenite-to-ferrite transformation has been studied in detail (e.g. [PHI 04, ZUR 09]). Secondly, the influence of an electric field on the diffusion of C has already been studied in single phases, both in $\gamma$-iron [OKA 70] and $\alpha$-iron [NAK 77]. Indeed, by analyzing the C distribution at the steady state, the authors were able to quantitatively measure the effective charge $Z^*$ (see Figure 5).

This effective charge is a key quantity to describe electromigration because the atomic drift flux of atoms, which occurs with application of an electric potential to a metal, is given by [HUN 61]:

$$\phi = \frac{ND}{k_B T} Z^* e \rho j \tag{3}$$

where $N$ is the atomic density, $D$ the diffusion coefficient, $T$ the temperature, $e$ the charge on an electron, $\rho$ the resistivity and $j$ the current density. They have shown that, at a constant temperature, when the sample is submitted to a constant electric current, $Z^*_\alpha$ scatters between +3 and +4 for temperatures higher than 700 °C. Concerning $Z^*_\gamma$, it significantly depends on electric current density as its values drop from +14 for low current densities to around +4 for high current densities. The effect of the temperature level on $Z^*_\gamma$ is not clear, especially for current densities below $1 \times 10^3\,\mathrm{A\,cm^{-2}}$ where reported values of $Z^*_\gamma$ are scattered between +3.5 and +14.3. Only one value of $Z^*_\gamma$ is reported in the intercritical domain (736 °C < T < 911 °C).

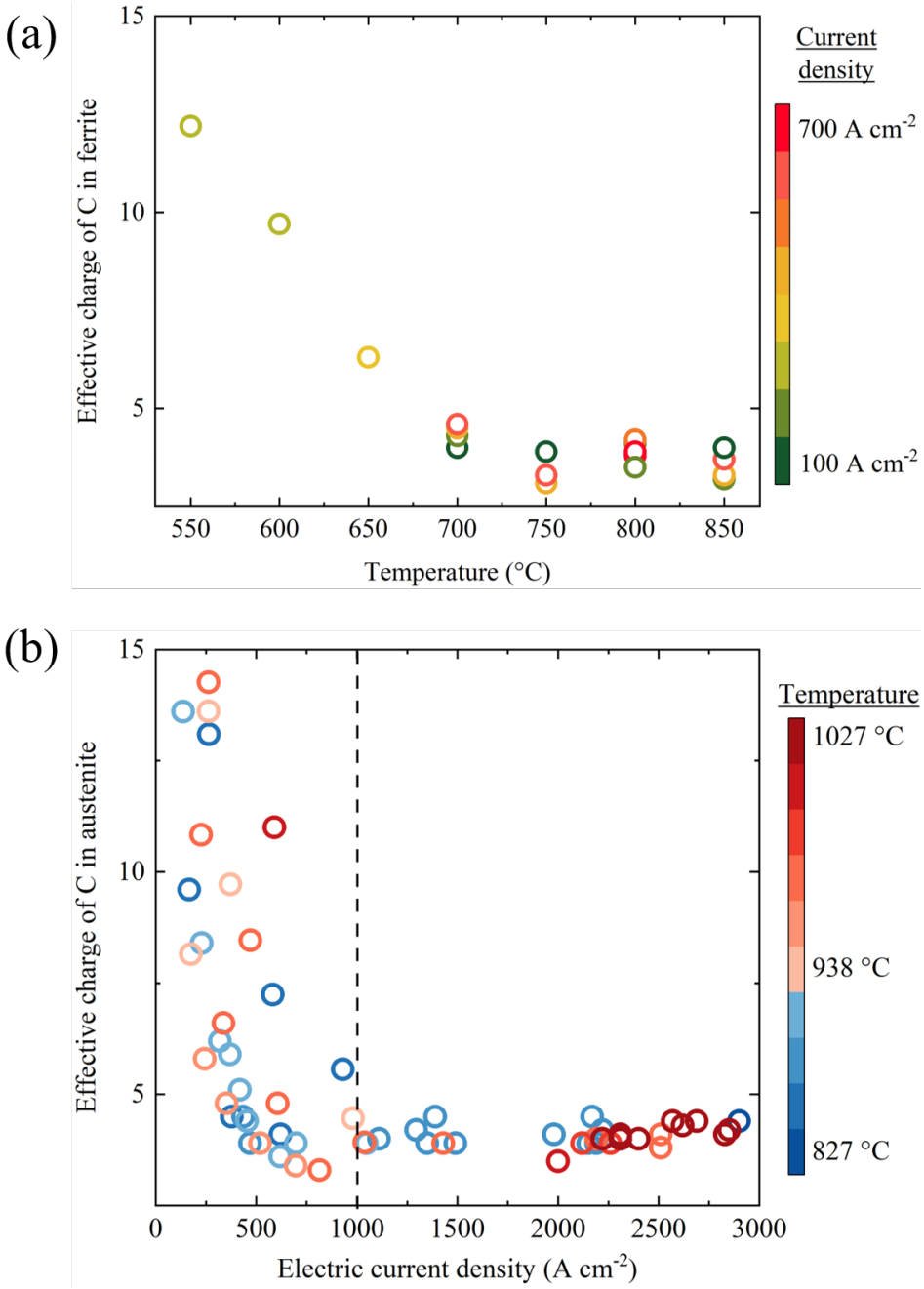


Figure 5: (a) Plot of effective charge of carbon in ferrite, $Z^*_\alpha$, vs. temperature T, at different electric current densities (represented with a color scale). (b) Plot of effective charge of carbon in austenite, $Z^*_\gamma$, vs. electric current density ($1 \times 10^2$ to $3 \times 10^3$ A cm$^{-2}$), at different temperature levels (represented with a color scale). The dotted curves are a guide for the eyes, data from Okabe *et al.* [OKA 70, OKA 73], Nakajima *et al.* [NAK 77, NAK 78], Falquero and Youdelis [FAL 70].

# Objectives of the PhD and outline

This PhD thesis is part of the ECUME (interactions of Electric CUrrents and Microstructures Evolutions) project, supported by a grant from the French National Research Agency (ANR-18-CE08-0008). The main objective of the ECUME project is to build a modelling framework at the scale of the microstructure to answer the need for a quantitatively predictive tool to describe the electrical processing of materials. Its strength is to bring together groups with an expertise on both resistivity measurement and electromigration, and a group developing variational models of microstructure evolution in multiphase metallic alloys. By performing dedicated experiment on well-chosen systems and the corresponding simulations, this project will be able to propose the first quantitative prediction of the electrical processing of multiphase materials.

The ECUME project involves three academic partners around three work packages:

Academic partners

- Laboratoire d'Etude des Microstructures (LEM) laboratory in Châtillon, France.
- Institut Jean Lamour (IJL) in Nancy, France.
- Matériaux : Ingénierie et Sciences (MatéIS) laboratory in Villeurbanne, France.

Work packages

1. Formulation of a model accounting for the coupling bewteen electric currents and microstructure evolutions (LEM + IJL + MatéIS)
2. Monitoring of phase transformations by electrical resistivity measurements (IJL + LEM)
3. Changing microstructures by electric current (MatéIS + LEM)

This PhD-work was carried out in MatéIS laboratory. Thus, it was involved in work packages 1 and 3, dealing with electrical processing of the Fe-C interstitial alloy, and microstructural characterization and modelling. The design and realization of a new electromigration experimental set-up was required to manage the temperature level and electric current in the samples independently. This work reports experiences focusing on determining the impact of an applied current on the diffusion of carbon atoms in iron and on the ferrite-austenite phase transformation.

It aims at describing and understanding of microstructural evolutions in the Fe-C system during an isothermal holding stage using Joule heating with continuous or pulsed electric current. The manuscript is composed of 4 chapters organised in the following manner:

1. **Chapter 1** proposes a state-of-the-art of the microstructural evolutions occurring during the electrical processing of metallic materials. The theories of electric-induced mass transfer are introduced with the mechanisms of diffusion in metals. The iron allotropic phase transformations and their modelling are then described. The literature review ends with discussions about the effects of electric current on phase transformations.
2. **Chapter 2** describes the initial state of the ARMCO iron used during this PhD thesis. Experimental methods and facilities used for thermal treatments and sample characterisation are then presented. This chapter also includes a modelling work on C diffusion accounting for the $\alpha/\gamma$ transformation kinetics and the electromigration of C in iron. The sensitivity analysis of the model parameters is used to set up a methodological approach to identify diffusion and electromigration parameters for experimental results.
3. **Chapter 3** is devoted to the determination of the influence of Direct Current (DC) on the $\alpha/\gamma$ transformation kinetics. C diffusion in ARMCO iron has been studied in the intercritical domain. In this temperature range, the ferrite transforms into austenite when the C concentration increases. Thermal treatments have been carried out with and without electric current. The samples' microstructures have been characterised to reveal the phase change's fronts position and the C concentration profiles. Numerical simulations have been performed to identify the main parameters of the model and to capture the physics behind the phenomena induced by the electric current.
4. **Chapter 4** investigates the possible influence of the pulsed current compared to a DC current on C electromigration and on the $\alpha/\gamma$ transformation kinetics. For a given temperature, the comparison is done for the same Joule heating due to either pulsed or direct current. These experiments will be used to in combination with numerical simulations to discuss the model parameters for pulsed current.

 

# Chapter 1

# State of the art

This chapter provides a literature review concerning the physical phenomena that have been accounting for in this study. In the first section, the ElectroMiGration (EMG) and the physical description of this phenomenon is introduced. The allotropic phase transformations occurring during the heat treatment of iron are presented in Section 1.2. It also includes some modelling tools developed to describe such microstructure evolutions. Then, Section 1.3 concerns the effects of the electric current on the microstructural transformations in metals. Finally, last Section 1.4 focuses on the existing studies of electromigration in the Fe-C system reported in the literature.

## Contents


**1.1 The electromigration phenomenon . . . . . 3**

1.1.1 Diffusion in solid crystals . . . . . 3

1.1.2 Diffusion under external forces . . . . . 5

1.1.3 Diffusion in the presence of an electric current . . . . . 7

**1.2 Iron allotropic phase transformations . . . . . 10**

1.2.1 Allotropes of iron . . . . . 10

1.2.2 Modelling tools for phase transformation . . . . . 11

**1.3 Effect of electric current on microstructural transformations in metals . . . . . 16**

1.3.1 Effect on InterMetallic Compound (IMC) growth . . . . . 16

1.3.2 Effect on recovery and recrystallization . . . . . 18

**1.4 Effect in the Iron-Carbon system . . . . . 19**
**1.5 Conclusions . . . . . 20**

## 1.1 The electromigration phenomenon

As explained in the Introduction, both the electric field and the electrons carried by the electric current are assumed to contribute to the electromigration of metal atoms diffusing in the lattice. First is described below the physics of the diffusion of atoms in metals. Then the influence of the electric current on the diffusion of metal atoms is discussed.

### 1.1.1 Diffusion in solid crystals

The perfect crystal of metals does not exist for temperature higher than the absolute zero. The crystal lattice presents point defects (illustrated in Figure 1.1) such as vacancies (missing atoms), substitutional atoms, impurities, boundaries between crystal of different orientation (grains), dislocations, etc. Crystal imperfections have strong influence upon many properties of crystals, such as strength, electrical conductivity and hysteresis loss of ferromagnets. Thus, some important properties of crystals are controlled by the density of imperfections and by the nature of the host crystals.

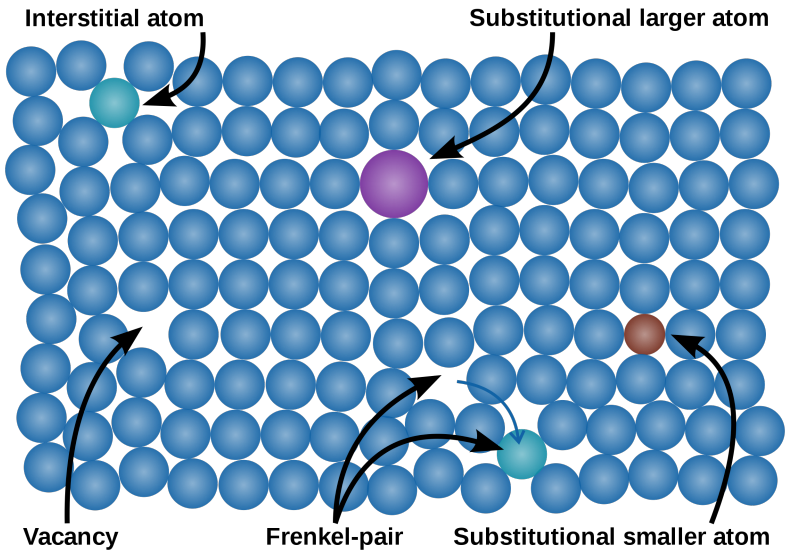


Figure 1.1: Point defects in crystal structures. (figure created under Creative Commons license)

Moreover, the atoms vibrate around their positions of equilibrium at a given frequency $\nu_0$ (Debye frequency) with an amplitude depending on the thermal energy of the atoms. If this amplitude is high enough, the atoms can overcome the energy barrier $\Delta G_m$ which is the free enthalpy of migration of atoms or vacancies. $p$ is the probability for an atom to migrate into a neighbouring vacancy, which is associated with $\Delta G_f$, the Gibbs energy of formation of the vacancy:

$$p = \exp\left(-\frac{\Delta G_f}{k_B T}\right) \tag{1.1}$$

with $k_B$ the Boltzmann constant and $T$ the absolute temperature (K).

The diffusion is the material transport by atomic motion. It is only possible if the atoms can shift and rearrange themselves in the lattice. It is through this succession of elementary jumps, from one position of equilibrium to another, that an atom can move in the material. The driving force of diffusion is the composition inhomogeneity of the material. It is a thermal activated phenomenon as it needs a temperature high enough to overcome energy barriers to atomic motion; the diffusion is also faster as the temperature increases. Then, the migration of an atom depends on the fraction of intrinsic point defects in thermodynamic equilibrium, which is expressed as a function of the free enthalpy of formation $\Delta G_f$ of a defect:

$$\frac{n_e}{N} = \exp\left(-\frac{\Delta G_f}{k_B T}\right) \tag{1.2}$$

where $n_e$ is the defect concentration in thermodynamic equilibrium and $N$ is the number of crystal atoms.

From the two previous equations 1.2 and 1.1, the jump frequency of vacancies $\Gamma$ in a crystal can be written:

$$\Gamma = \nu_0 \exp\left(-\frac{\Delta G_f}{k_B T}\right) \exp\left(-\frac{\Delta G_m}{k_B T}\right) \tag{1.3}$$

Then, the expression of the diffusion coefficient $D$ characteristic of a species is:

$$D = D_0 \exp\left(-\frac{\Delta H}{k_B T}\right) \tag{1.4}$$

$$D_0 = \beta a^2 \nu_0 \exp\left(-\frac{\Delta S}{k_B}\right) \tag{1.5}$$

The equation 1.4 shows the temperature dependence of the diffusion coefficient as it follows the Arrhenius dependence law, with $\Delta G = \Delta G_m + \Delta G_f$ the activation energy of the diffusion phenomenon. In the equation 1.5, $D_0$ includes the terms independent of the temperature, where $a$ is the lattice parameter, $\beta$ is a factor of correlation depending on the crystalline structure ($\beta$=1 for body-centred cubic and face-centred cubic structures) and $\Delta S$ is the entropy.

### 1.1.2 Diffusion under external forces

At equilibrium, the mean thermal diffusion of atoms or vacancies is null. The potential energy of a crystal at equilibrium is represented in Figure 1.2(a). The energy barrier is the same for all neighbouring free lattice sites and there is no preferred direction for diffusion. The movement of atoms would need a concentration gradient and/or the lowering of an energy barrier in a certain direction thanks to the work of an external force.

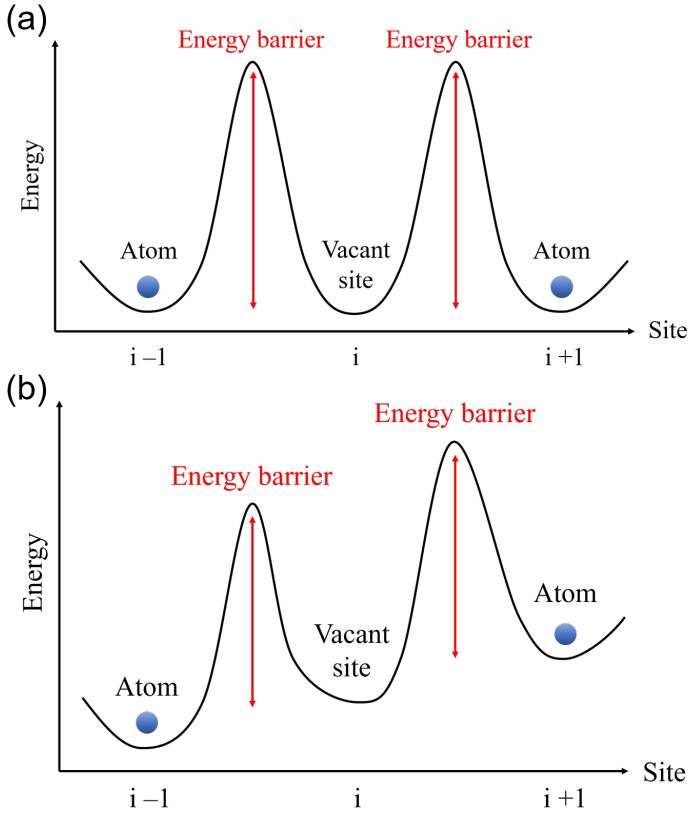


Figure 1.2: Schematic of potential energy in a crystal (a) without any force (b) under an external force.

Under the influence of an external force, the potential energy of a crystal is modified (see Figure 1.2(b)). The probability of jump to a given vacant site is higher with a lower energy barrier. Thus, the matter moves in a preferred direction with a drift velocity $v_d$. The matter moved under the effect of a force induces a concentration gradient which generates a second flow in the opposite direction. The total flow is then the sum of the one induced by the concentration gradient of which the expression is given by the first Fick's law, and the one caused by the action of the external force:

$$J = -D\frac{\partial C}{\partial x} + v_d C \tag{1.6}$$

where $C$ is the concentration of the migrating species, $D$ is its diffusion coefficient and $x$ is the position.

The Nernst-Einstein law relates the drift velocity $v_d$ of charge carriers with their diffusion coefficient $D$ under the applied force $F_{ext}$ and the thermal agitation energy, in the form of the product of the Boltzmann constant $k_B$ and the absolute temperature $T$:

$$v_d = \frac{F_{ext} D}{k_B T} \tag{1.7}$$

### 1.1.3 Diffusion in the presence of an electric current

**Note:** A more detailed development of the final equations can be found in the Appendix A.

A small transport of atoms occurs in addition to the transport of electrons when an electric field is applied to a conductor. As described in the previous subsection, this atomic transfer is induced by the effect of an external force. The metal atoms are regarded as cations as they might lose electrons due to high electric current and/or "electron gas" at high temperature. By analogy with ions during an electrolysis, it is assumed that they are subjected to two forces: the direct electrostatic force and a drag force resulting from the ion/electron collisions. If all the atoms of a metal are considered to be positively charged owing to the loss of electrons to the "electron gas", the resultant force produced by an electric field on a metal alloy may be expressed as:

$$F = \sum_i n_i Z_i eE - n_e eE = 0 \tag{1.8}$$

where $n_i$ and $n_e$ are the number of ions or atoms of component $i$ and electrons respectively, per unit volume, $e$ is the charge of an electron, $Z_i$ is the valence of component $i$ (the electron valence is taken as -1) and $E$ is the electric field intensity. There is no net charge within the metal in thermodynamic equilibrium, thus this force must necessarily be zero.

The frictional force $F_{ei} = \delta_{ei}E$ of the electrons upon component $i$ is proportional to the electric field E and $\delta_{ei}$ is a friction coefficient. In combination with equation 1.8:

$$n_e eE = \sum_i n_i \delta_{ei} E = \sum_i n_i Z_i eE \tag{1.9}$$

$$\sum_i n_i eE(Z_i - \frac{\delta_{ei}}{e}) = 0 \tag{1.10}$$

Then, the net force on component $i$ of charge $Z_i$ must be:

$$F_i = eE(Z_i - \frac{\delta_{ei}}{e}) \tag{1.11}$$

The true charge on a component $Z_i$ can be obtained only if the frictional coefficient $\delta_{ei}$ can be determined independently, or vice versa. The bracketed term in equation 1.11 is generally referred to as **the effective charge** (or valence) $Z_i^*$. Consequently, equation 1.11 can be written in the following simple form:

$$F_i = eEZ_i^* \tag{1.12}$$

The direction of transport of component $i$ is predicted by the sign of $Z_i^*$ in solid metals and metallic alloys. A negative sign indicates that electron-friction forces predominate and transport occurs towards the anode. On the opposite, a positive effective charge means that the field force is stronger than the friction force and the transport is directed towards the cathode. Theoretical treatments (Bosvieux and Friedel [BOS 62], Klemm [KLE 62]) aimed to develop an expression for $\delta_{ei}$ which then allowed the determination of $Z_i$ from experimental measurements. The difficulties in identifying atomistic mechanisms lead to the use of the effective charge $Z_i^*$ which rather describes experimentally observable behaviour.

Since the early investigations of the EMG phenomenon, theoretical treatments of electrotransport in metals do not really succeed in explaining experimental data. Some theories neglected to account for the frictional force, apparently because of its complexity. The existing models originate from Fiks [FIK 59] and Huntington and Grone [HUN 61] first mathematical formulations who treated the electron wind force with a ballistic approach (collisions between mobile points defects and charge carriers). They came up with the following Equation (1.13) which gives the atomic flux $J$ induced by a current density $j$ [SAK 11]:

$$J = \frac{NDZ^*}{RT} F\rho j \tag{1.13}$$

with the electrical resistivity $\rho$, the atomic density $N$, the diffusion coefficient $D$, the ideal gas constant $R$, the temperature $T$ and the Faraday constant $F = eN_A$, that is defined as the product of the Coulomb charge $e$ and the Avogadro constant $N_A$.

Accounting for this electric current induced atomic flux, the derivation of the mass conservation leads to the Nernst-Einstein law (Equation (1.7)) which describes the drift velocity $v_{d,i}$ induced by the electric current to the atoms $i$ if the external force is the resultant force written in Equation 1.12:

$$v_{d,i} = \frac{D_i Z_i^*}{RT} F\rho j \tag{1.14}$$

The continuity equation associated with the Fick's law gives the diffusion equation in 1D describing the distribution of a species $i$ [CHE 14]:

$$\frac{\partial C_i}{\partial t} = -\frac{\partial J_i}{\partial x} = \frac{\partial}{\partial x}(C_i \frac{D_i}{RT} \frac{\partial \mu_i}{\partial x}) \tag{1.15}$$

where $C_i$ is the concentration of component $i$, $J_i$ its atomic flux, $D_i$ its diffusion coefficient and $\mu_i$ its electrochemical potential, $T$ is the temperature, $x$ is the distance and $R$ is the ideal gas constant.

At a given temperature, the electrochemical potential $\mu_i$ of $i$ in a dilute solution submitted to an electric field is dependent on the activity $a_i = \gamma_i C_i$ with $\gamma_i$ the activity coefficient, and the local electrostatic potential $\phi$. We assume that the solution is ideal and $\gamma_i = 1$ in this case. In molar units, the electrochemical potential can be written as [ALB 13]:

$$\mu_i = \mu_i^0 + RT \ln C_i + F Z_i^* \phi \tag{1.16}$$

$$\frac{\partial \mu_i}{\partial x} = \frac{\partial \mu_i^0}{\partial x} + RT \frac{1}{C_i} \frac{\partial C_i}{\partial x} + F \frac{\partial (Z_i^* \phi)}{\partial x} \tag{1.17}$$

The final form of the equation of diffusion in 1D accounting for the electromigration is obtained by combining the equations (1.15) and (1.17) (see A for more details):

$$\frac{\partial C_i}{\partial t} = \frac{\partial}{\partial x}[C_i \frac{D_i}{RT}(\frac{\partial \mu^0}{\partial x} + RT \frac{1}{C_i} \frac{\partial C_i}{\partial x} + F \frac{\partial (Z_i^* \phi)}{\partial x})] \tag{1.18}$$

$$\frac{\partial C_i}{\partial t} = D_i \frac{\partial^2 C_i}{\partial x^2} + \left[ \frac{\partial \mu^0}{\partial x} + F \frac{\partial \left( Z_i^* \phi \right)}{\partial x} \right] \frac{D_i}{RT} \frac{\partial C_i}{\partial x} \tag{1.19}$$

## 1.2 Iron allotropic phase transformations

Allotropic phase transformations correspond to a rearrangement of the crystal lattice of a material when it is thermally or mechanically stressed. They induce the coexistence of two phases and an interface in-between, the phase change's front. Iron is a very interesting material which presents two main allotropes at ordinary pressures, depending on the temperature.

### 1.2.1 Allotropes of iron

Below 912 °C, iron has a body-centred cubic (bcc) structure known as $\alpha$-iron or ferrite $\alpha$. It is thermodynamically stable and a quite soft phase (50 – 100 $HV_{20}$ hardness), with ferromagnetic properties below its Curie point of 770 °C and paramagnetic above this temperature. The maximum solubility of C in $\alpha$-iron is about 0.02 wt.% C at 727 °C [BHA 17]. Ferrite is a solid solution of carbon but the term ferrite is often used to indicate $\alpha$-iron itself.

At ambient temperature, the initial microstructure of iron and steel is generally a mixture of ferrite ($\alpha$) and pearlite. Pearlite consists of ferrite $\alpha$ and cementite $Fe_3C$, an iron carbide, often arranged as a lamellar structure. When heated above the eutectoid equilibrium temperature $A_{e1}$, this initial microstructure undergoes a solid-state transformation. It becomes a ferrite-austenite mixture in the intercritical

domain ($A_{e1} < T < A_{e3}$) and a fully austenitic structure above $A_{e3}$. The start ($A_{e1}$) and end ($A_{e3}$) temperatures of the austenitic transformation depend on the steel's chemical composition [BHA 17].

The second allotropic phase of iron is austenite or $\gamma$-iron, which has a face-centred cubic (fcc) structure and forms above 912 °C for pure iron. It accepts considerably more C atoms than ferrite, up to 2.04 wt% at 1146 °C. Small atoms like C (radius of 0.67 Å) can fit in the interstitial sites of Fe. However, the radii and number of sites available depend on the crystal structure (see Table 1.1). C occupies preferentially octahedral voids in both FCC and BCC due to lesser distortion. There are more but smaller octahedral voids in BCC than in FCC, which explains the difference of maximum solubility of C between ferrite and austenite phases.

| **Iron allotrope** | **Crystal structure** | **Number of tetrahedral sites** | **Radius of tetrahedral sites (Å)** | **Number of octahedral sites** | **Radius of octahedral sites (Å)** |
|---|---|---|---|---|---|
| Ferrite | BCC | 12 | 0.366 | 6 | 0.195 |
| Austenite | FCC | 8 | 0.290 | 4 | 0.534 |

Table 1.1: Characteristics of the iron crystal: structures and interstitial sites

### 1.2.2 Modelling tools for phase transformation

The phase transformation complexity comes from the possibility for austenite to nucleate and grow from several sites in the initial two-phase microstructure (ferrite+cementite), preferentially on C-rich areas and non-equilibrium high-energy defects [SAV 10]. For a constant temperature and pressure, the thermodynamic equilibrium condition for ferrite-austenite phase transformation is characterised by the minimum of the total Gibbs free energy for which is obtained the chemical potential equality between ferrite and austenite for all chemical elements (Fe and C) [GOU 15]. The first definition of equilibrium is the equilibrium state reached after long heat treatments (also called orthoequilibrium, OE).

However, practical applications usually involve or require the achievement of a transient equilibrium. The local equilibrium (LE) is based on the respect of the equilibrium conditions at the $\alpha/\gamma$ interface. It evolves during the phase transformation advancement and it is only valid in ternary systems. The paraequilibrium (PE)

is based on the assumption that the phase transformation is only driven by the C diffusion. Then, only C can diffuse and equalise its chemical potential within ferrite and austenite. PE can only be applied for short treatment times or fast kinetics.

Thus, modelling tools are used to describe and predict metallurgical evolutions. There are many models available in the literature and the main ones are presented in the following.

#### 1.2.2.1 Phenomenological approach

Diffusive transformations are usually described by the Johnson-Mehl-Avrami-Kolmogorov (JMAK) formalism. It gives the evolution of the transformed fraction $Y(T,t)$ (with $0 < Y(T,t) < 1$) as a function of time $t$ and temperature $T$ (K). In isothermal conditions and under several simplifying assumptions, the JMAK law is expressed by the following relation:

$$Y = 1 - \exp\left(-(bt)^n\right) \tag{1.20}$$

where $n$ is the Avrami exponent independent of the temperature for a given transformation and $b$ is the rate constant (in $s^{-1}$) defined as follows:

$$b = b_0 \exp\left(-\frac{Q}{RT}\right) \tag{1.21}$$

where $b_0$ is a constant, $Q$ is the activation energy of the transformation ($\mathrm{J\,mol^{-1}}$), $R$ is the gas constant and $T$ the temperature (K).

After determining the values of the three parameters $n$, $Q$ and $b_0$ from experimental kinetics, this type of modelling is efficient to predict any additional kinetics under isothermal or non-isothermal conditions. The JMAK law was successfully used to describe many transformations in iron such as ferrite recrystallisation [HUA 04, LI 13, KUL 13, KUL 14], ferrite-to-austenite transformation [KUL 13, KUL 14] and austenite-to-ferrite transformation [ASH 17]. However, it describes one transformation at a time and it does not predict the influence of changes in chemical compositions (for example the evolution of C distribution) or the influence of additional driving forces.

#### 1.2.2.2 Physically based modelling

The lack of physical assumptions of empirical models makes difficult their generalisations for different temperatures or chemical composition ranges. Different approaches for phase transformation prediction developed in the literature are presented in the following.

**1) Diffusion-controlled model** The phase transformation may be modelled considering only the diffusivity of the transformation [KOP 00]. In this case, the kinetics of the massive transformation are based on the diffusion of elements across a sharp moving interface respecting the local equilibrium conditions on both sides of the interface. The allotropic transformation kinetics is driven by the respect of local equilibrium conditions at the interface. From a practical point of view, the model of migrating interface is based on the numerical resolution of the Fick equation in each phase in a finite difference system with the following relationship:

$$\frac{\partial C_i}{\partial t} = D_{i,j} \frac{\partial^2 C_i}{\partial z^2} \tag{1.22}$$

with $D_{i,j}$ and $C_i$ respectively the diffusion coefficient and the concentration of element $i$ in the phase $j$. The interface motion is obtained supposing the respect of local thermodynamic equilibrium at the interface. The interface velocity $v$ is therefore expressed by a mass balance for each element $i$:

$$v = \frac{dz}{dt} = \frac{J_{i,\gamma} - J_{i,\alpha}}{c_{i,\gamma}^{eq} - c_{i,\alpha}^{eq}} \tag{1.23}$$

where $J_{i,\alpha}$ and $J_{i,\gamma}$ are fluxes of $i$ at ferrite and austenite side of the interface. $c_{i,\gamma}^{eq}$ and $c_{i,\alpha}^{eq}$ are the solubility limits of $i$ element which are determined thanks to thermodynamics.

Diffusion-controlled models were successfully used in the case of binary, ternary or even quaternary systems. Additional driving forces can be included in the diffusion equation to be solved. However, modelling of complex systems or scenarios leads necessarily to longer simulation time and increasing numerical problems.

**2) Mixed mode model** Mixed-mode models overcome the problem of solving complex multiple element diffusion profiles by introducing the concept of interface mobility, with its own kinetics [CHR 02]. They were initially developed for the

austenite-ferrite transformation [KRI 97, SIE 04, BOS 07, BOS 09]. Supposing a finite interface mobility, authors have implemented an algorithm allowing a deviation from the equilibrium at the interface. The transformation kinetics is hence managed by the interface velocity $v$ as expressed below:

$$v = M \times \chi(T) \times \left(C_{C,\gamma}^{Int} - C_{C,\gamma}^{Eq}\right) \tag{1.24}$$

with $C_{C,\gamma}^{Int}$ and $C_{C,\gamma}^{Eq}$ corresponding respectively to the interfacial and equilibrium carbon content in austenite. $\chi(T)$ is a temperature dependent parameter. The interface mobility $M$ is usually supposed to obey to an Arrhenius-like law:

$$M = M_0 \exp\left(-\frac{Q}{RT}\right) \tag{1.25}$$

with $Q$ the activation energy and $M_0$ a mobility constant. This approach makes it possible to reproduce experimental kinetics. However, the mobility applied to take into account the interaction of other elements has no physical meaning. Thus, it limits the predictive capacities of such models. Mecozzi *et al.* applied such an approach for ferrite-to-austenite transformation [MEC 15]. They realised a comparative study between the diffusion-controlled, interface-controlled and the mixed-mode model changing both the holding temperature and mobility values. Despite this, they did not validate this model with an experimental database.

**3) Gibbs Energy Minimization (GEM) model** Mathevon *et al.* [MAT 21] developed a model based on the prediction of (i) concentration profiles for all elements in ferrite, cementite and austenite, and (ii) interface migration, thanks to the minimisation of the total Gibbs energy in the entire system (*i.e.* phase field approach). Assuming the energy of a multi-component system (*e.g.* Fe$XY$) the linear combination of the energy of each binary systems (Fe$X$ + Fe$Y$), the total Gibbs energy is the weighted sum of the Gibbs energies over all nodes expressed as:

$$G^{tot} = \sum_i \left(\mu_{\mathrm{Fe},j}^0 + \sum_k \left[\mu_{\mathrm{Fe},j}^B(X_k) \cdot (1 - X_k) + \mu_{k,j}^B(X_k) \cdot X_k - \mu_{\mathrm{Fe},j}^0\right]\right) \tag{1.26}$$

where $\mu_{\mathrm{Fe},j}^0$ is the chemical potential of pure iron in phase $j$, $\mu_{\mathrm{Fe},j}^B(X_k)$ and $\mu_{k,j}^B(X_k)$ are the chemical potentials of iron and element $k$ in a binary Fe/$k$ system of composition $X_k$ in phase $j$ ($\alpha$ or $\gamma$).

The GEM model aims at solving a unique diffusion profile within 3 phases (*i.e.* cementite, austenite and ferrite). It was applied to model the $\alpha + (\mathrm{Fe}, \mathrm{Mn}, \mathrm{Cr})_3 C \rightarrow \gamma$ phase transformation over complex thermal cycles for Fe-C-Mn and Fe-C-Cr systems with cementite dissolution and $\alpha \leftrightarrow \gamma$ phase transformation. It provides the kinetics of $\alpha \rightarrow \gamma$ and $\gamma \rightarrow \alpha$ transformations without imposing any type of equilibrium conditions at the interface while including diffusion within the interface. This numerical approach respects mass balance and leads to drastic reduction of the computation times compared to existing models.

## 1.3 Effect of electric current on microstructural transformations in metals

### 1.3.1 Effect on InterMetallic Compound (IMC) growth

In most cases, the polarity effect of EMG is experimentally visible: the diffusion of species $i$ is enhanced in the direction of the DC current if their effective charge is negative ($Z_i^* < 0$), or in the opposite direction which is the electron flow if $Z_i^* > 0$. When two metals are in contact, one can diffuse into the other and form intermetallic compound(s). Chen et al. studied the electric current effects upon various interfacial reactions [CHE 98, LIU 98, CHE 99, CHE 00]. The passage of electric current ($500\,\mathrm{A\,cm^{-2}}$) can either enhance or retard the growth of IMC in the Sn-Ag and Sn-Ni systems depending upon the flow direction of electrons. They determined the effective charge of tin to be $Z_{Sn}^* = -90$. They also reported a dramatic increase of the growth rate of $Al_3Ni_2$ at the interface of the Al/Ni couple with the passage of a $10^3\,\mathrm{A\,cm^{-2}}$ electric current, clearly visible on Figure 1.3. They suggested that the electric current may have enhanced the growth rate of the intermetallic layer by boosting its nucleation rate.

Gan and Tu also observed the polarity effect of EMG on kinetics of Cu-Sn IMC formation [GAN 05]. With current densities of $4 \times 10^3\,\mathrm{A\,cm^{-2}}$ to $4 \times 10^4\,\mathrm{A\,cm^{-2}}$, the growth of the IMC layer was faster at the anode and hindered at the cathode, in comparison with the case without current.

Some studies reported the influence of the electric current on the IMC growth kinetics without visible asymmetry due to current direction. In the work of Chen *et al.* in the Bi-Ni system, the growth of $NiBi_3$ phase was enhanced at 150 °C and 170 °C, but there was no visible influence of the direction of the electron flow. The authors suggested that the current may enhance the diffusivity of both atoms to a degree proportional to their atomic ratio in the product and that this could lead to a symmetric growth even though EMG is operative. Garay *et al.* published different studies on the effect of high DC currents (up to $2.5 \times 10^3\,\mathrm{A\,cm^{-2}}$) in interfacial reactions in the Al-Au and Ni-Ti systems [GAR 03, BER 01, BER 02]. The applied current was found to significantly increase the growth rate of the intermetallic layers. The current may induce changes in the growth mechanisms through the increase of the mobility or the concentration of point defects over the thermal equilibrium values.

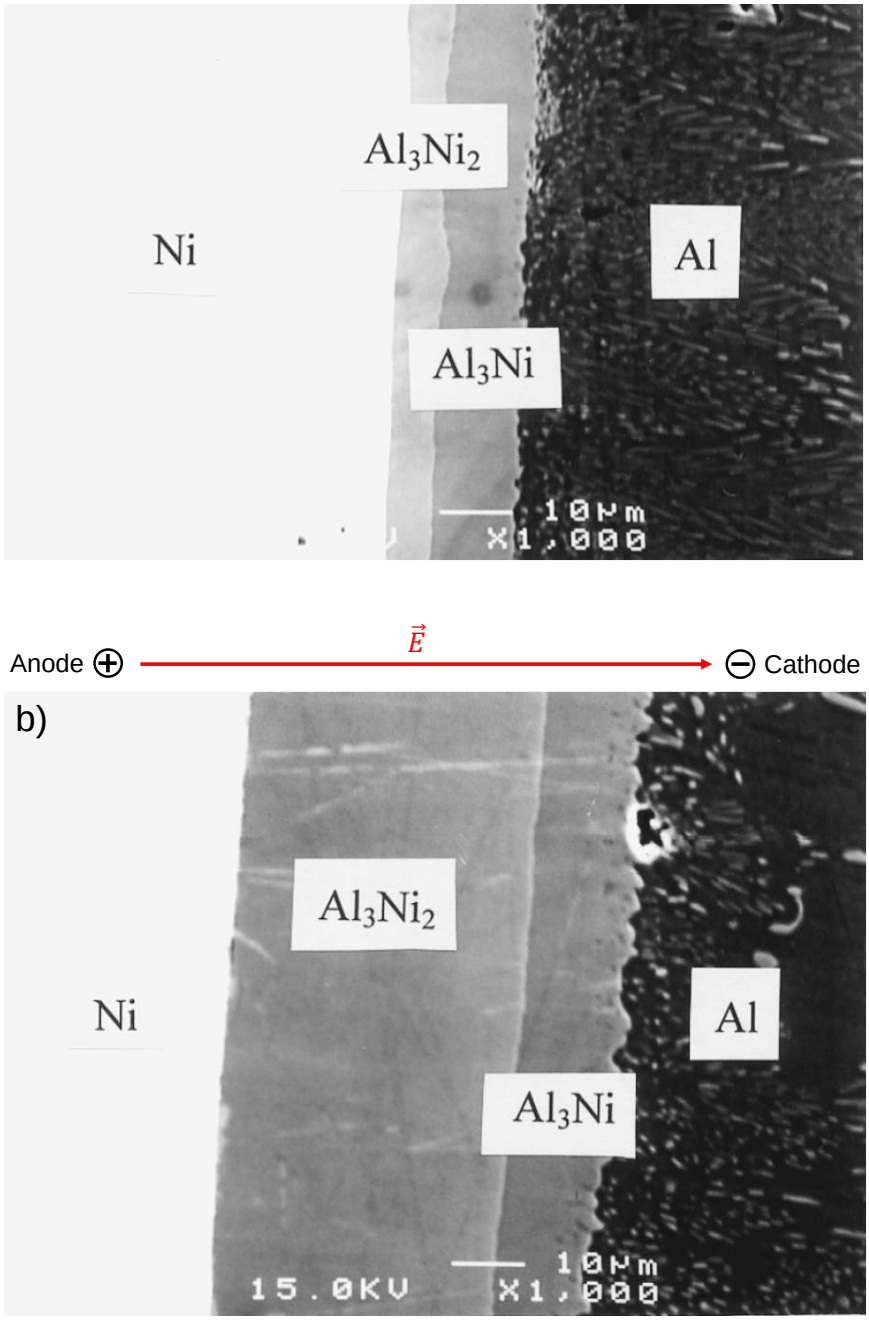


Figure 1.3: The interface of the Al/Ni couple annealed at 400 °C for 336 h (a) without passage of electric currents (b) with the passage of a $10^3$ A cm$^{-2}$ electric current.

### 1.3.2 Effect on recovery and recrystallization

Conrad reviewed the effects of electric current on recrystallization of cold-worked metals and alloys [CON 00b]. A continuous DC current of $10^3\,\mathrm{A\,cm^{-2}}$ enhances the recrystallization rate of cold worked $\alpha$-Ti and gave a finer recrystallized grain size. It was also accelerated in a number of cold worked metal wires (Cu, Al and $Ni_3Al$) with application of high-density pulsed DC current ($10^5\,\mathrm{A\,cm^{-2}}$, 100 µs pulse duration) during annealing. The largest influence of the current appeared to be at the beginning of the process, which is the nucleation stage. The electropulsing mainly increased the pre-exponential factor of the Arrhenius equation for the recrystallization rate, with only little influence on the activation energy. This suggests that the effect of the electric current is to increase the Debye frequency $\nu_0$ of the atoms involved in the thermally-activated process and/or the activation entropy $\Delta S$ in $D_0$ rather than the barrier height $Q$ (Equation 1.5). On the contrary, electropulsing retarded the subsequent rate of grain growth, independently of the frequency and the duration of the pulses. For identical annealing times, the samples treated with electropulses presented a more advanced stage of recovery with a significantly lower dislocation density. The current pulsing may increase the mobility of dislocations and their annihilation, hindering the grain growth.

Fabrègue *et al.* [FAB 14] investigated the influence of an applied pulsed current on the recovery and recrystallization of pure extruded Cu rods. They showed that these phenomena are greatly accelerated by the electric current. A Joule heating treatment of 10 min at 300 °C with electric current density of 500 to $600\,\mathrm{A\,cm^{-2}}$ was sufficient to obtain fully recrystallized microstructures, when the same treatment without current in salt baths only leads to a partial recovery. Both the accelerated recovery and the accelerated nucleation of recrystallization are qualitatively consistent with a current enhanced vacancy concentration.

The EP and AC treatments usually follow a hard working pre-treatment, such as rolling and drawing. The effectiveness of the electrical methods for the microstructure and property manipulation depends on the dislocations and high strain energy produced. Recent studies have shown that the DC treatment can be applied for inducing microstructure and property variations in metals without the need of a hard working pre-treatment for inducing dislocations [SHU 20], recrystallization [LIA 17b] and property variations [LIA 17a].

## 1.4 Effect in the Iron-Carbon system

As mentioned in the Introduction, this PhD work focuses on the Fe-C system with the objective of better understanding the influence of electric current on a diffusion process, as well as the kinetics of a phase transformation.

The electromigration involves diffusion of species in a metal lattice submitted to an electric current. In the Fe-C system, only the diffusion of C in the Fe lattice is considered. The self-diffusion of iron depends on its phase and its crystal structure, but it is much slower than the diffusion of C in ferrite ($10^{-12}$ to $10^{-9}\,m^2\,s^{-1}$) or austenite ($10^{-12}$ to $10^{-11}\,m^2\,s^{-1}$) in the intercritical domain (736 to 911 °C). For comparison, values of self-diffusion coefficients of iron phases are plotted in Figure 1.4, with the intercritical domain filled in orange.

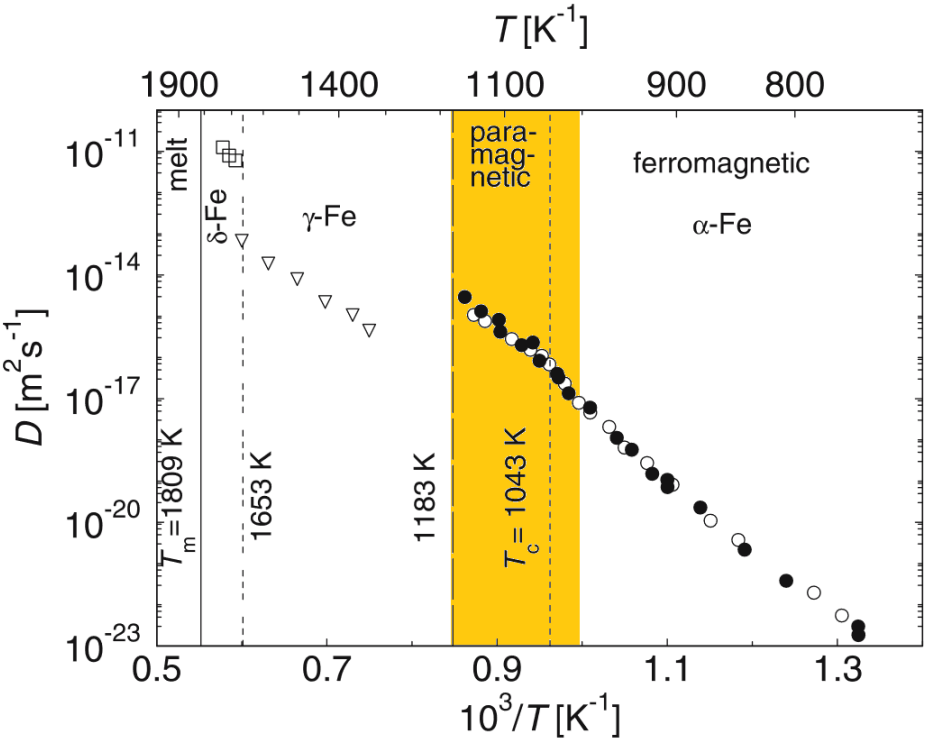


Figure 1.4: Self-diffusion coefficients of iron phases in their solid state, with the intercritical domain filled in orange (736 to 911 °C = 1009 to 1184 K) [MEH 07].

The diffusion of carbon in iron controls the kinetics of many transformations of major importance for the steel industry: cementite precipitation, martensite tempering, massive austenite-ferrite transformation and bainite formation. The effective charge is the main parameter governing the EMG phenomenon because it depicts

the behaviour of metallic atoms diffusing under the influence of an electric current. However, as mentioned in the Introduction, few data are found in the literature for C in iron or carbon steels, and only for single phase materials (ferrite or austenite). The effective charge of C in single phase ($\alpha$ or $\gamma$) Fe was experimentally determined many years ago by Okabe and Guy [OKA 70, OKA 73] and Nakajima *et al.* [NAK 77, NAK 78]. They both used the steady-state method to determine its value in either ferrite or austenite, at several temperature levels and electric current densities.

Nakajima *et al.* [NAK 77] determined the value of $Z^*$ in Fe-$\alpha$ for temperature between 550 °C and 850 °C and for current densities between 100 A cm$^{-2}$ and 900 A cm$^{-2}$. Its value drops from +12.2 at 550 °C to +3.5 at 850 °C. For temperatures higher than 700 °C, $Z^*_\alpha$ scatters between +3 and +4. The uncertainty on the data values is ± 0.5 because of the small influence of electric current density on $Z^*_\alpha$.

The effective charge of C in austenite $Z^*_\gamma$ at different electric current densities have also been measured for temperatures between 920 °C and 1000 °C. Its values significantly depend on electric current density, dropping from +14 for low current densities to values around +4 for high current densities. The effect of the temperature level on these values is not clear, especially for current densities below 1000 A cm$^{-2}$ where reported values of $Z^*_\gamma$ are scattered between +3.5 and +14.3. Only one value of $Z^*_\gamma$ is reported in the intercritical domain (736 to 911 °C): [OKA 73] calculated an effective charge of +4.4 for carbon in austenite at 827 °C.

## 1.5 Conclusions

The effect of an electric current on the Fe-C system mainly involves the electromigration of C in the iron lattice. The equation of diffusion 1.19 describes the evolution of the C concentration accounting for this phenomenon. The atomic flow induced by the presence of the electric current is described by a drift velocity (Equation 1.14). The main parameters are the diffusion coefficient $D$ and the effective charge $Z^*$ of carbon in iron.

Iron undergoes an allotropic transition from a bcc structure (ferrite or $\alpha$-Fe) to a fcc structure (austenite or $\gamma$-Fe) at 911 °C. The kinetics of this phase transformation has been extensively studied [PHI 04, ZUR 09]. Among the different modelling tools available in the literature, the Gibbs Energy Minimization (GEM) model appears

to be practical to describe the $\alpha/\gamma$ phase transformation and the electromigration of C in iron (thanks to the drift velocity in the diffusion equation). The influence of an electric field on the diffusion of C has already been studied in iron single phases, both in $\alpha$-Fe [NAK 77] and in $\gamma$-Fe [OKA 70]. However, the effective charge of C is yet to be determined in the case of iron phase transformation. In fact, it is important to consider as the electric current is already used for thermal treatments of iron and steels who request to control the phase transformation involve

# Chapter 2

# Material and methods

This chapter aims at describing the experimental and numerical methods developed to study the EMG of C in iron. The initial chemical composition and microstructural state will be detailed for the ARMCO iron used in this PhD-work. The experimental conditions and characterisation methods are then described. The GEM model is adapted to account for the electromigration of C in iron. It is used to produce simulations of electric current heat treatments whose typical results are described.

## Contents


**2.1 Experimental strategy . . . . . 24**

2.1.1 Material: ARMCO iron . . . . . 24

2.1.2 Heat treatments performed . . . . . 25

**2.2 Experimental techniques . . . . . 26**

2.2.1 Sample preparation before heat treatment . . . . . 26

2.2.2 Thermal treatments . . . . . 26

2.2.3 Sample characterisation . . . . . 32

**2.3 Model and simulation . . . . . 38**

2.3.1 Carburisation simulation configuration . . . . . 38

2.3.2 Example of results from the model . . . . . 42

2.3.3 Model parameters sensitivity study . . . . . 44

2.3.4 Key points . . . . . 47

# 2.1 Experimental strategy

## 2.1.1 Material: ARMCO iron

The material used in the present work is an ARMCO ingot iron as-drawn rod (50 mm diameter, 99.8 % purity) from *Goodfellow*. The announced impurities concentrations are Mn < 0.08 wt.%, C < 0.02 wt.%, P < 0.02 wt.% and S < 0.015 wt.%. They are in agreement with the composition measured by electron microprobe (EPM) and energy-dispersive X-ray spectroscopy (EDXS) (Table 2.1).

| **Element** | **C** | **Mn** | **P** | **S** | **Fe** |
|---|---|---|---|---|---|
| **wt.%** | 0.02 | 0.04 | 0.02 | 0.02 | bal. |
| **at.%** | 0.09 | 0.04 | 0.04 | 0.03 | bal. |

Table 2.1: Bulk composition of the ARMCO iron obtained by EPM and EDXS analyses

The microstructure of as-received state (Figure 2.1) is composed of ferrite grains of heterogeneous size 44 ± 25 µm, due to the as-drawn condition. Very small dark inclusions (MnS, MnO) are visible. They precipitate in the cooling melt iron during the solidification and the purification steps of the elaboration process. They are then deformed and fragmented when the iron rod is drawn.

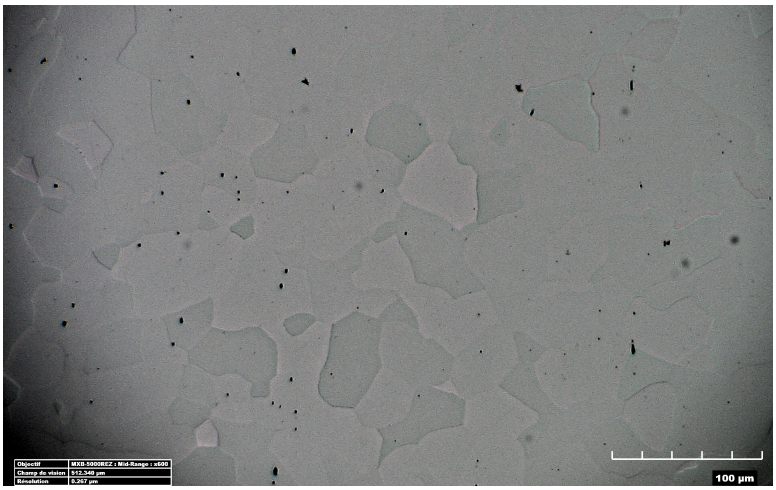


Figure 2.1: Optical micrograph of the as-received ARMCO iron microstructure (colloidal suspension final polishing). Ferrite grains heterogeneous in size and small (MnS, MnO) inclusions are observed.

### 2.1.2 Heat treatments performed

Carburisation (*i.e.* voluntary diffusion of C in iron) has been performed during heat treatments in the intercritical domain of temperature (orange area on Figure 2.2(a)). The intercritical domain is delimited by $Ae_1$ and $Ae_3$, respectively the start and the end temperatures of austenite formation. These temperatures depend on the C concentration. As illustrated on Figure 2.2(b), the ARMCO iron samples were heated from room temperature to the target temperature (775 °C, 825 °C or 875 °C) at the heating rate of 100 °C min$^{-1}$. The samples are in contact with graphite sheets (Papyex) and it is expected that carbon diffuses from the graphite into the iron. Once the target temperature is reached, the carburisation duration that would lead to a significant diffusion thickness and a significant difference between the front positions is evaluated to several hours (it has been fixed to 7 hours for all the experiments). This duration is necessary to ensure a large diffusion depth and to induce a significant ferrite-to-austenite transformation.

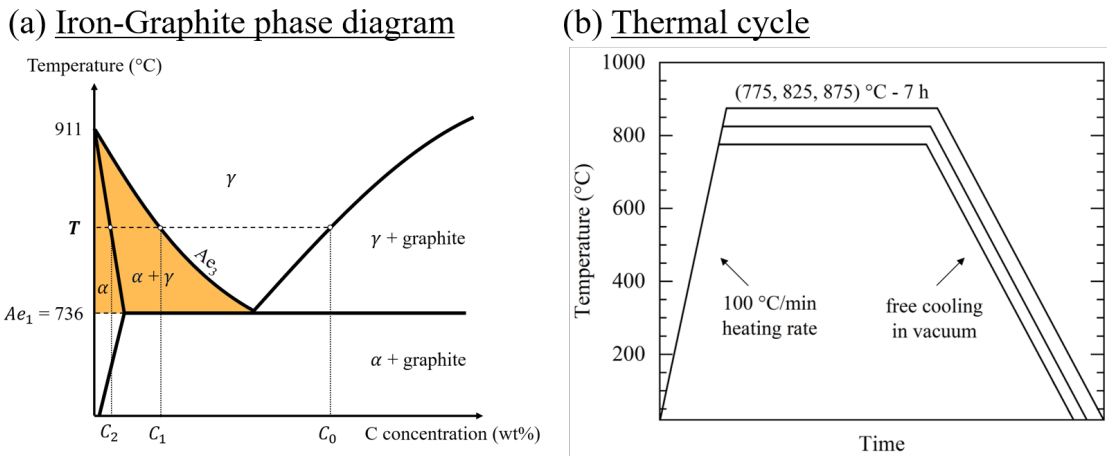


Figure 2.2: (a) Schematic Iron-Carbon phase diagram. The boundary condition $C_0$ of the C concentration at the interface is determined by the equilibrium concentration between C and Fe at a given temperature $T$. The intercritical domain of temperature $Ae_1 < T < Ae_3$ is filled in orange. (b) Thermal cycle used to study the electromigration of C in ARMCO iron during the ferrite-austenite phase transformation.

Considering the Fe-C thermodynamic diagram (Figure 2.2(a)), C might significantly diffuse in iron for temperature higher than $Ae_1 = 736$ °C. In the intercritical domain (area in orange), C diffusion promotes ferrite to austenite transformation

that gives rise to a difference of microstructure between the transformed region and the initial ferrite. Then, the front transformation position is a good indication of the C diffusion. Above 912 °C, all the initial ferrite is transformed into austenite and the C diffuses only in austenite. Performing the carburisation in the intercritical domain allows a convenient observation of the samples' microstructure after each heat treatment. After cooling, the prior austenite grains will transform into pearlite or a mixture of pearlite and ferrite depending on the C concentration. The final microstructure is easily observed after polishing and Nital etching.

## 2.2 Experimental techniques

### 2.2.1 Sample preparation before heat treatment

To ensure C diffusion from graphite to iron during the carburisation experiments, the contacting surfaces have to be polished. The samples are gradually polished using SiC polishing papers (P-320, P-800, P-1200, P-2500 and P-4000) and polishing cloths with polycrystalline diamond MetaDi Supreme suspensions of 6 µm, 3 µm and 1 µm.

Papyex graphite sheets are then stuck to the two polished sample surfaces thanks to conducting carbon cement (Leit-C, *Sigma-Aldrich*). After drying Leit-C solvent (xylene) overnight, the samples are ready to use.

### 2.2.2 Thermal treatments

The thermal treatments conducted in this work were performed thanks to two different facilities : a Spark Plasma Sintering (SPS) apparatus and an AET furnace. The SPS is used to apply pulsed electric current through a sample. The target temperature is reached thanks to Joule heating and it is controlled only by the current density. On the contrary, the AET furnace is able to either heat the sample by radiation alone, or by an additional Joule heating with continuous (DC: Direct Current) current provided by an external generator.

#### 2.2.2.1 Spark Plasma Sintering (SPS)

A Spark Plasma Sintering apparatus (HPD25 model from *FCT Systeme GmbH*) was used to apply a pulsed DC current through a sample during thermal treatment. The

temperature of the sample increases due to Joule heating. The temperature level is controlled varying the current density. The maximum heating power is 60 kW, with an intensity and a tension up to 8 kA and 8 V respectively. The current in the sample is pulsed: it is equal to $I_{peak}$ during a part $\Delta t$ of the period $\tau$ of the pulse. It is then possible to calculate the mean equivalent continuous current crossing the sample: $I_{moy} = \dfrac{I_{peak}\Delta t}{\tau}$. For all the experiments in SPS, a pulsed current with a duty ratio $\dfrac{\Delta t}{\tau} = \dfrac{2}{3}$ and a frequency of 667 Hz was used.

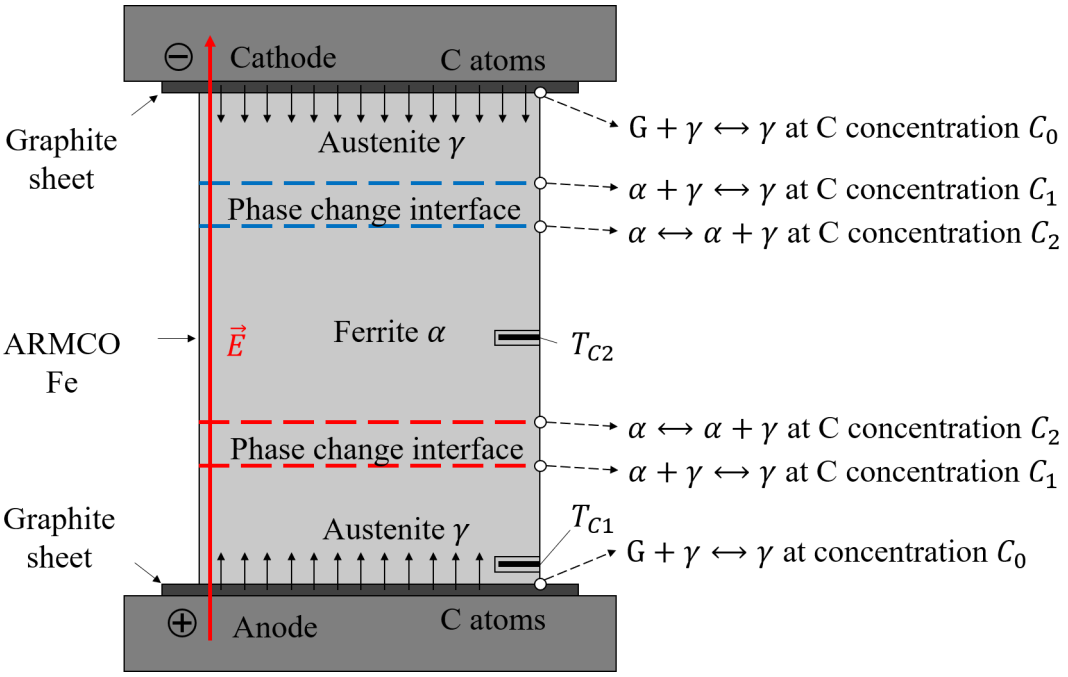


Figure 2.3: Principle of carburisation during SPS thermal treatment with phase transformation inside an ARMCO iron sample. The cross-section of an ARMCO iron ring is represented (vertical axis symmetry) and stretched for more clarity. C concentrations $C_0$, $C_1$ and $C_2$ are linked to the Fe-C phase diagram (Figure 2.2(a)).

Figure 2.3 presents the principle of experimental set-up and the phenomena induced by C diffusion inside the sample. The ARMCO iron sample is placed between the upper and the lower water-cooled graphite punches. Papyex graphite sheets are put in-between them. Carbon glue is used to stick the graphite sheets onto the iron sample. Two type K thermocouples 1 mm in diameters are placed in holes 2.5 mm in depth, one near the interface ($T_{C1}$) and another one ($T_{C2}$) in the middle of the sample. A vacuum of $\sim 10^{-4}$ mbar is applied in the chamber to minimise the oxygen content in the atmosphere of treatment and thus, to avoid sample oxidation. From

the ambient temperature, the sample is heated via the Joule effect to the target temperature in the intercritical domain with a heating rate of $100\,°C\,min^{-1}$. The electric current density is regulated in order that temperature $T_{C1}$ follows the imposed thermal cycle. The temperature difference between $T_{C1}$ and $T_{C2}$ is maximum and equal to 15 °C at the beginning of the heating phase and then decreases and does not exceed 2 °C after 2 hours. Therefore, the temperature gradient between the interface and the middle of the sample is not significant. $I_{moy}$ varies between 1.6 to 1.3 kA during the holding stage. This variation is due to creep deformation which reduces the sample height variation (up to 2.5%) depending on the temperature level during the experiment and due to the sample electrical resistivity change. Creeping is unavoidable since to ensure a good electric contact the force between the two punches of the SPS has to be set to the minimum value of 5 kN. In the intercritical domain, iron is not anymore elastic and deforms continuously under the force applied between the punches [FEL 53]. Using creeping characteristics, we determined that if the sample section is larger than $7\,cm^2$ the deformation becomes lower than 10% at 950 °C during 7 hours holding time.

The heat source due to Joule effect induces temperature gradients in the sample. To minimize these temperature gradients, the sample has the shape of a hollow cylinder which inner, outer diameters and height are respectively $d_i = 40\,mm$, $d_o = 50\,mm$ and $h = 6\,mm$. In the intercritical domain the creeping did not exceed 2.5 % for the 5 kN force applied equivalent to a pressure of 7 MPa. The peak current density through the sample is therefore between 360 to $400\,A\,cm^{-2}$, depending on the temperature of treatment.

The diagram of the experimental set-up used in the SPS is illustrated in Figure 2.3. Due to the C diffusing from the two graphite sheets into the samples, there will be two diffusion fronts: from the cathode and from anode interfaces. The electric current and the C electromigration might lead to a different front position from these two interfaces. Unlike the oxidation, the decarburisation in our samples can not be avoided in the areas in contact with the atmosphere. However, the thickness of the samples ($d_o - d_i = 10\,mm$) weakens its impact. The microstructural observations were conducted in the middle section of each sample as well.

#### 2.2.2.2 AET furnace

The society *AET Technologies*, specialised in developing industrial and laboratory furnaces, was requested to build a new thermal treatment equipment. It is able to heat samples by conventional heating (here by radiation) and/or *via* Joule heating, in a controlled atmosphere. The purpose of this equipment is to manage the temperature level and current density independently.

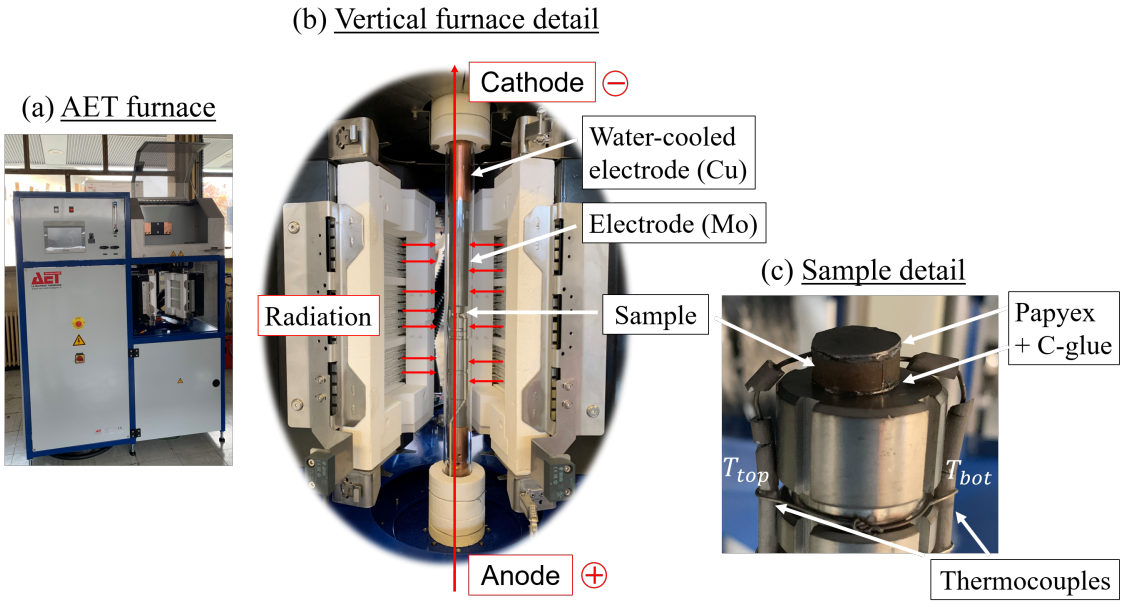


Figure 2.4: (a) Overall picture of the AET furnace. (b) Vertical furnace: the sample is placed inside a quartz tube, in between two electrodes (anode and cathode) both in two parts made of two different materials, molybdenum and copper. The heating is obtained by radiation (symbolised by the small red arrows) with halogen lamps and/or *via* Joule heating with an external generator. (c) The sample made of ARMCO iron is glued with Papyex (graphite) sheets thanks to C-glue. Two type K thermocouples $T_{top}$ and $T_{bot}$ are inserted to measure the temperature in the sample's core.

The heating in the vertical furnace (Figure 2.4(b)) is divided in three zones of halogen lamps able to work at 1000 °C. Two identical type S thermocouples are positioned near the lamps to prevent the overheating. Samples are placed in a airtight system made of:

- a vertical hermetic quartz tube of diameter 40 mm in the center of the furnace
- two hermetic heads assuring the tube airtightness.

A *Leybold* pumping system (membrane primary pump + DN63 turbomolecular pump) assures a high-quality secondary vacuum. It is also possible to inject nitrogen to purge the atmosphere of the tube or to obtain a $N_2$ atmosphere. Samples are placed in-between two vertical electrodes in the quartz tube. These electrodes come in two parts: one half exposed to the heating source is made of molybdenum ; the other half is made of copper and water-cooled.

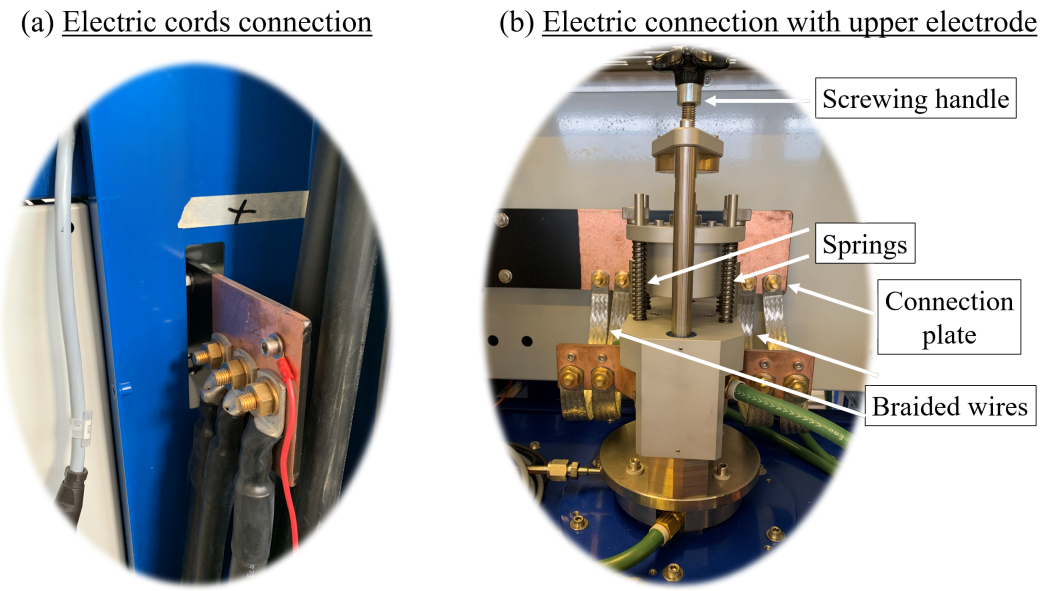


Figure 2.5: (a) Electric cords connecting the lower electrode (anode) copper plate with the power supply. (b) Two braided wire leads connect each electrode with its copper plate.

To perform heat treatments assisted by electric current, an external power supply *Acore Industrie* RGT 763 provides a DC current up to 500 A of intensity under a 30 V voltage. This allows the ARMCO iron samples (diameter 13 mm and height 6 mm cylinders) to be crossed by electric current densities up to 382 A cm$^{-2}$. This maximum value is comparable with the peak current densities used in the SPS (360

to 400 A cm$^{-2}$). As seen on Figure 2.5, each electrode is connected to the power supply by three electric cords (section = 95 mm$^2$, total length = 26 m) screwed to two copper plates (one on top for the cathode and one at the bottom for the anode) which length, width and thickness are 160 mm, 100 mm and 10 mm respectively. Each plate is connected to its corresponding electrode thanks to two braided wire leads made of soft copper. A potentiometer allows to adjust the intensity of the electric current delivered by the power supply. The temperature $T$ (in °C) of the sample heated *via* Joule effect depends on the electric current density (in A cm$^{-2}$) obeying the following equation (determined experimentally):

$$\forall\ j \in [200, 500]\ \ \mathrm{A\,cm^{-2}},\ T = 1.7615\,^{\circ}\mathrm{C\,cm^2\,A^{-1}} \times j - 87.8\,^{\circ}\mathrm{C} \tag{2.1}$$

The copper part of electrodes are water-cooled. Thus, the utility of the AET furnace is that it decouples the temperature level from the current density. The sample used in this furnace has been designed so that the temperature reaches 600 °C when it is submitted to the maximum current intensity (500 A cm$^{-2}$). In this way, as illustrated on 2.2(b), the ferrite-austenite phase transformation is not prompted by Joule heating alone. The sample is then heated to the target temperature in the intercritical domain with a heating rate of 100 °C min$^{-1}$ by radiation in the vertical furnace. The heating power is regulated in order that the temperature $T_{bot}$ follows the imposed thermal cycle. The temperature difference between $T_{top}$ and $T_{bot}$ is maximum and equal to 50 °C at the beginning of the heating phase and then decreases and does not exceed 10 °C after 30 min. The cooling kinetics at the end of the experiment is not controlled but it is measured thanks to the thermocouples; the cooling stage lasts around 10 min.

The ARMCO iron sample used in AET furnace is a small cylinder of diameter $d_o$= 13 mm and height $h$ = 6 mm. It is sandwiched between two Papyex graphite sheets sticked with carbon glue. The sample is then placed on top center of the lower electrode. Two type K thermocouples $T_{top}$ and $T_{bot}$ 1.1 mm in diameter are inserted in holes 5 mm in depth, one 1 mm from the top and one 1 mm from the bottom of the sample. The whole column with the sample on top is elevated inside the quartz tube from the bottom hole. The upper electrode is then put in contact with the sample using an endless screw compressing four springs. It is also used to set the compression force onto the sample. To ensure a good electric contact, the value of the force between the two electrodes is set to 70 N equivalent to a pressure

of 0.5 MPa. It is lower than in SPS so the creeping is limited in this set-up. A vacuum of $\sim 10^{-5}$ mbar is applied in the quartz tube to avoid the sample oxidation. From the ambient temperature, the sample is heated to the target temperature in the intercritical domain with a heating rate of 100 °C min$^{-1}$. The heating power is regulated in order that the temperature $T_{bot}$ follows the imposed thermal cycle. The temperature difference between $T_{top}$ and $T_{bot}$ is maximum and equal to 40 °C at the beginning of the heating phase (overshoot) and then decreases and does not exceed 10 °C after 30 min. Therefore, the temperature gradient within the sample should not be too significant during the holding stage.

### 2.2.3 Sample characterisation

The microstructure of samples before and after heat treatment was characterised at different scales. After cooling, the samples are cut in half along the vertical direction and they are polished to observe their middle section.

#### 2.2.3.1 Sample preparation for metallography

When the sample has cooled down after the carburisation treatment, the samples are cut in half in order to observe their core cross-section. The metallographic observation requires a careful preparation. Samples are mounted in bakelite so that only their cross-section to observe is visible.

Mechanical preparation is the most common method of preparing materialographic specimens for microscopic examination. Thereby, samples are ground using different SiC abrasives (P-320, P-800, P-1200, P-2500 and P-4000). The direction of grinding is changed from paper to paper and specimens are washed between each step. Then, polishing is carried out on cloths with polycrystalline diamond MetaDi Supreme suspensions of 6 µm, 3 µm and 1 µm as abrasive products.

For electron microscopy observations, colloidal silica MasterMet suspension (0.06 µm) is also used for advanced surface preparation by vibratory polishing.

#### 2.2.3.2 Optical microscopy (OM)

The observation of the microstructure with OM requires the etching of samples. The mechanism of etching multiphase alloys is essentially electrochemical in nature. Because of a difference in potential between the structural components, a preferential

dissolution occurs causing roughness, especially at the boundaries. When observed microscopically, shadow effects are seen and the various structural features are delineated. Nital 4% etching solution (4 mL nitric acid + 96 mL ethanol - 10 s) was used to reveal the microstructure of our samples. An example of microstructure obtained after chemical etching is shown in Figure 2.6.

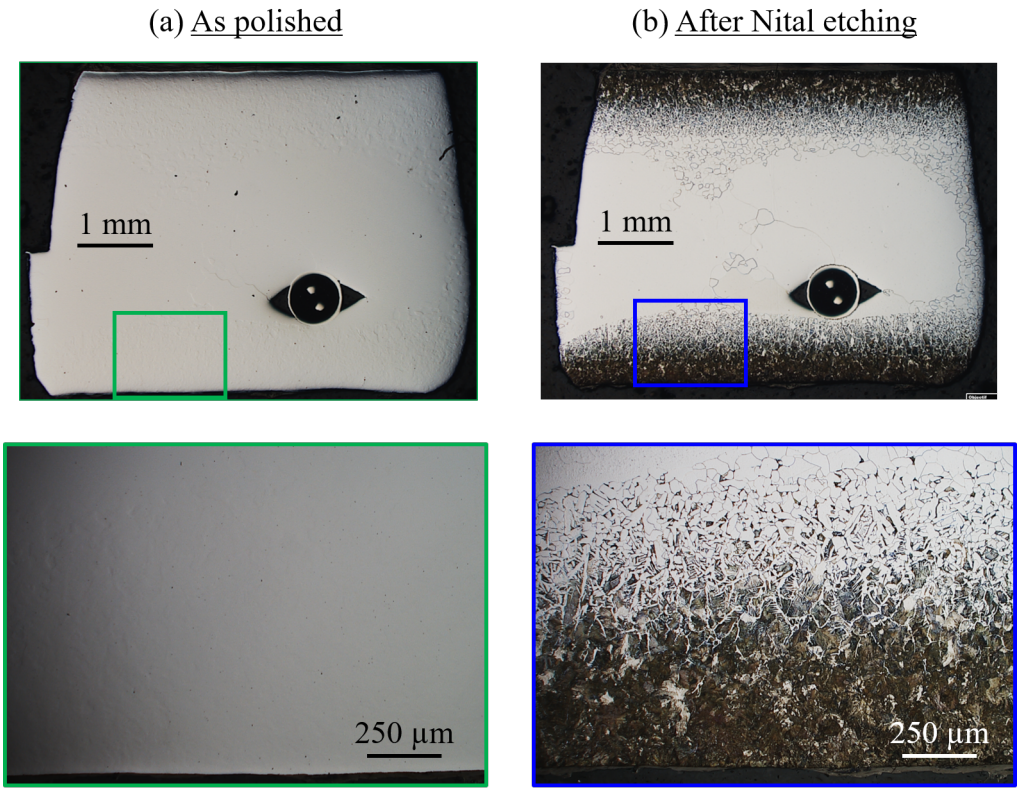


Figure 2.6: Optical micrograph of a sample's cross-section (a) as polished; or (b) after Nital etching: pearlite (ferrite + cementite $Fe_3C$) appears black while ferrite is white.

A 3D digital microscope *HIROX RH-2000* was used to take pictures of the various microstructures obtained. The experimental phase fractions and C concentration profiles were then quantified from ferrite and pearlite phases distribution using *Fiji* (Fiji Is Just ImageJ) software. Figure 2.7 shows the result of thresholding a metallography. This is achieved by calibrating the image, correcting its brightness, converting it to grey scale and globally thresholding the image using the Otsu method. After that the image shows a number of black pixels with a value of 255 (pearlite) and white pixels with a value of 0 (ferrite). The ratio of the average pixel value on

a horizontal line to the maximum pixel value (255) gives the corresponding perlite fraction. Plotting the evolution of this fraction in the vertical direction (direction of carbon diffusion) allows to establish the profile related to the microstructure of the sample. Figure 2.8 illustrates such pearlite quantification method and a typical distribution profile.

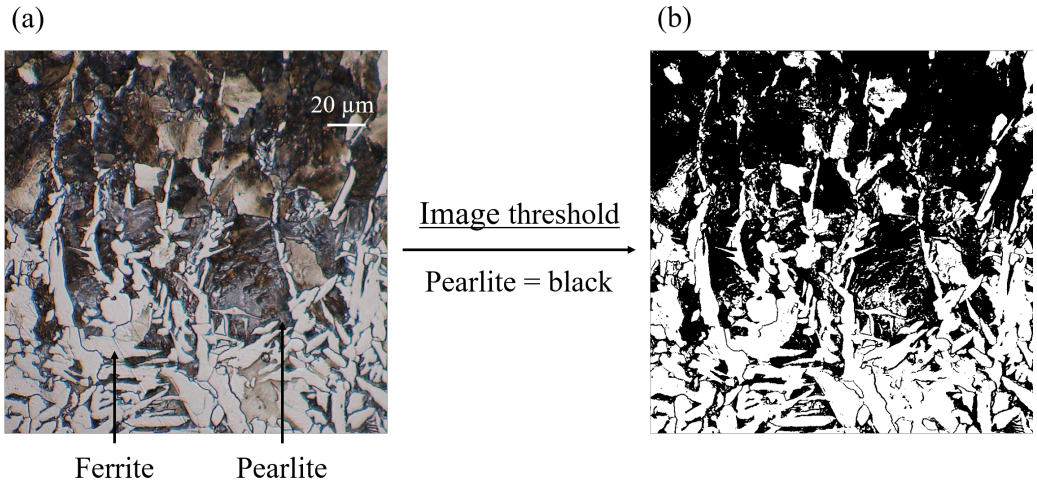


Figure 2.7: (a) Optical micrograph after Nital etching: pearlite appears brown or black while ferrite is white. The result from thresholding this image is given in (b) where pearlite is black (grey value = 255) and ferrite is white (grey value = 0).

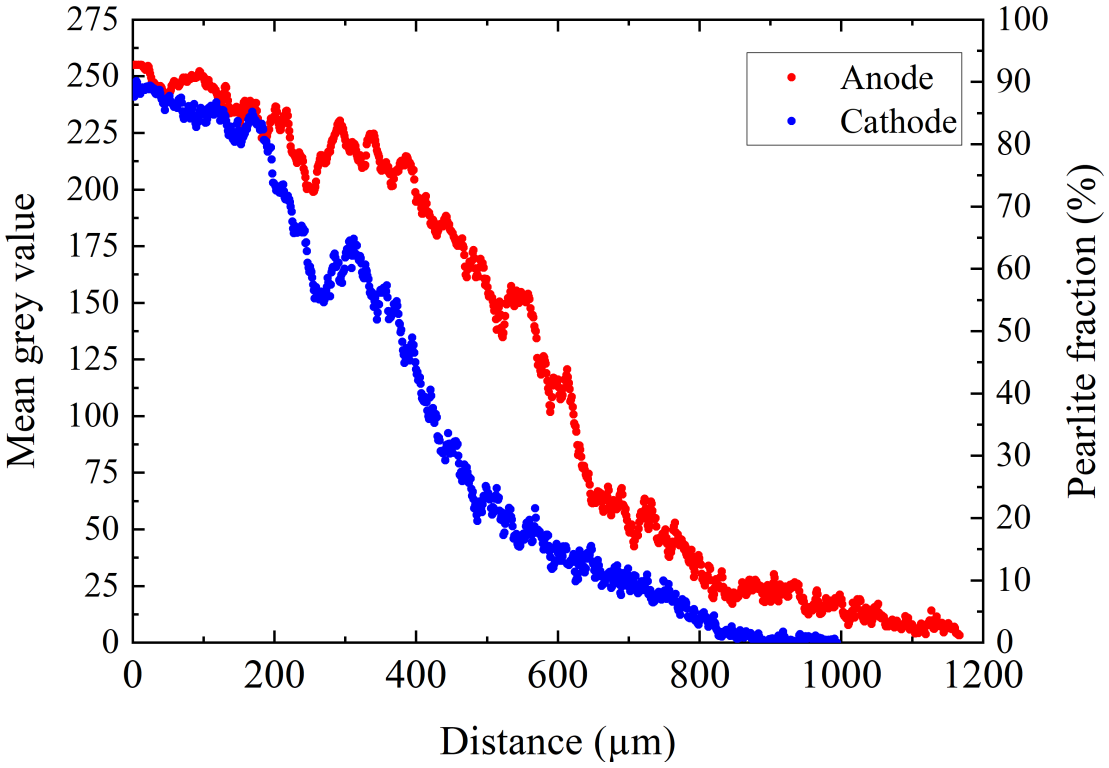


Figure 2.8: Typical result from phase quantification procedure using *Fiji*. The mean grey value profile allows to quantify the evolution of the fraction of pearlite with the depth of diffusion.

#### 2.2.3.3 Microhardness indentation

Vickers hardness measurements have been performed with a 0.2 kg load on a *Buehler* machine. Hardness profiles are obtained by indentation along two staggered rows with a 25 µm step (Figure 2.9). Typical standard deviation was determined to be ± 10 $HV_{0.2}$ for 80 measurements.

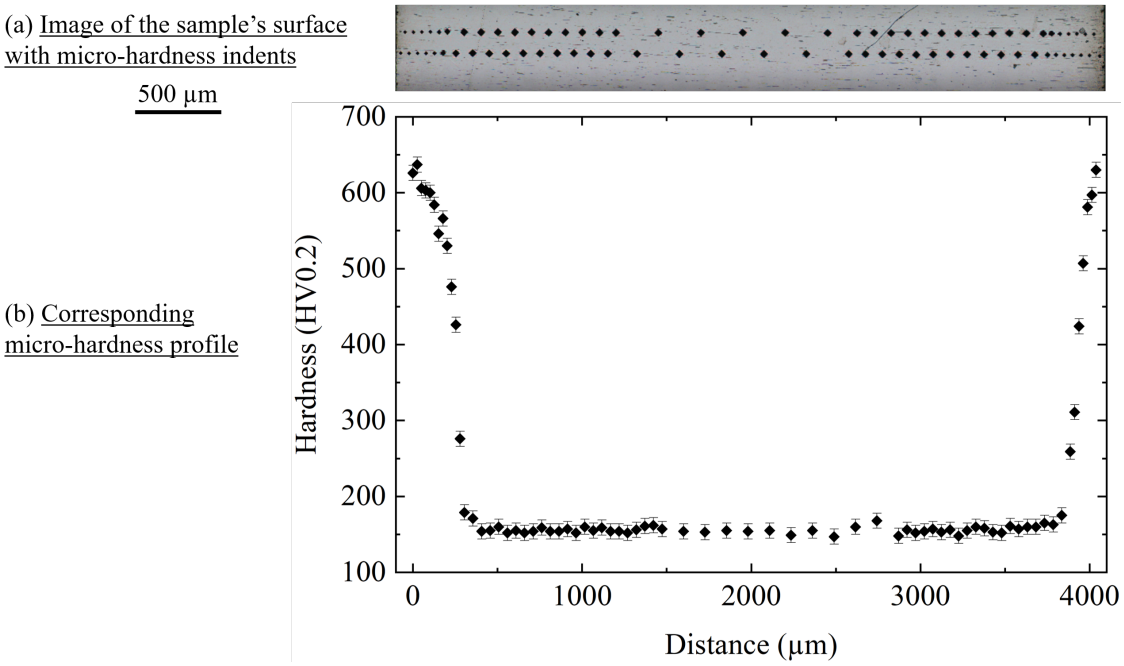


Figure 2.9: (a) Example of micro-hardness indentation along two staggered rows and (b) the hardness profile obtained.

#### 2.2.3.4 Electron Probe MicroAnalysis (EPMA)

Samples heat treated in SPS have been analysed by wavelength-dispersive X-ray spectroscopy (WDXS or WDS) thanks to an electron microprobe *Cameca SX100* at the CMTC technology platform (INP Grenoble, France). This non-destructive analysis method is used to determine the chemical composition of small volumes of solid materials. It is based on the identification of photons resulting from electron beam interaction with the target, with the wavelength of the photons being characteristic of the atoms excited by the incident electrons.

The objective here is to quantify C (K$\alpha$ line) and Mn concentrations of our SPS samples. They have been mounted and polished down to 1 µm. A final polishing with alumina (0.3 µm) is performed right before their introduction in the analysis chamber. The analyses have been conducted in punctual probe mode with an acceleration voltage of 15 kV and acquisition time of 40 s for each measurement. Therefore, a typical 2 mm-long concentration profile is obtained in 2 hours of time.

The calibration was carefully carried out to assure quantitative results. The Mn element was simply calibrated on a pure control. However, the calibration for the C element is more difficult.

In order to reduce carbon contamination under the electron beam, a liquid nitrogen anti-contamination trap and an oxygen micro-leak were used. In addition, the controls and samples were cleaned and re-polished (1 µm alumina) just prior to their introduction into the microprobe. The calibration of the C element consists of determining a calibration line from various steel control samples of known carbon composition (C mass content varying between 0.2 and 1 wt.% C) [ROB 06]. The coefficients of the linear regression line are calculated from the intensities acquired during 40 s at the position of the C K$\alpha$ line on the different carbon controls. As the C is a very light chemical element, its quantitative analysis is difficult for concentrations lower than 0.5 wt.% C. The results of microprobe analysis (in Chapter 4) will hence be presented for concentrations higher than 0.5 wt.% C. The standard deviations on concentrations determined by EPMA in this study are ± 0.02 wt.% for element C and ± 0.003 wt.% for element Mn.

## 2.3 Model and simulation

A recently developed model has been proposed by Mathevon *et al.* [MAT 21] to predict austenite-ferrite transformation kinetics in steels. It is based on the prediction of concentration profiles for all elements in iron in the whole domain, including the phase transformation interface volume. The ferrite/austenite interface displacement is obtained minimizing the total Gibbs energy of the entire system. The Gibbs energy is calculated as a function of C concentration and temperature thanks to a thermodynamic database made with Thermodynamic Calculation Interface (TQ) on Thermocalc TCFE6 database.

To account for the influence of the electric current on the C diffusion the drift term has been added to the diffusion equation (Equation 1.19). Moreover, a sensitivity study of the influence of the different numerical model parameters has been carried out and its results are presented in this section. A better understanding of the model allowed the further adjustment of these parameters to describe the experimental kinetics of diffusion and phase transformation.

### 2.3.1 Carburisation simulation configuration

The initial microstructure of the rectangular cross-section ARMCO iron samples is assimilated to a 1-D system, composed of ferrite and austenite (see Figure 2.10). The numerical solution of the model has been implemented for two migrating interfaces to simulate iron carburisation as experimented in SPS and AET furnace. The electric current is directed along the increasing abscissae $x$. The anode corresponds to abscissa $x = 0$ and the cathode is at abscissa $x = L$, with $L$ the length of the cross-section of the samples. The austenite fraction will grow as the carbon diffuses through the existent austenite, reaches the interface and enriches the ferrite.

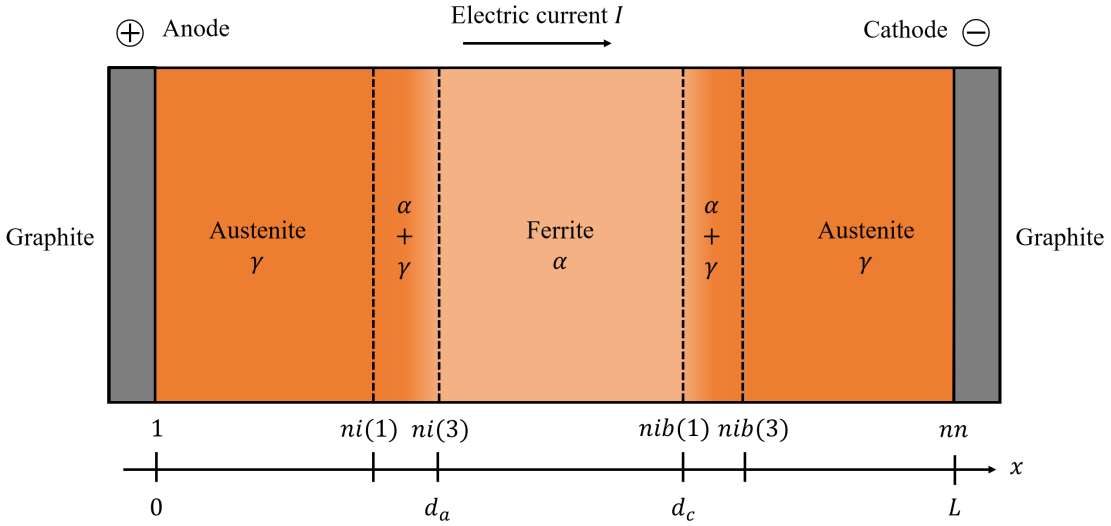


Figure 2.10: Schematic carburisation simulation configuration with 2 migrating ferrite/austenite interfaces.

The diffusion equation (see Equation (2.2)) is solved using 1-D implicit Finite Difference scheme with the following discretized equation for nodes $j = 2\ ..\ nn-1$:

$$\frac{\partial C_i}{\partial t} = \left[\frac{\partial \mu^0}{\partial x} + F\frac{\partial (Z_i^* \phi)}{\partial x}\right] \frac{D_i}{RT}\frac{\partial C_i}{\partial x} + D_i \frac{\partial^2 C_i}{\partial x^2} \tag{2.2}$$

$$\begin{aligned}\frac{C_j^{t+\Delta t} - C_j^t}{\Delta t} = &\frac{D_j\left(C_{j+1}^{t+\Delta t} - C_j^{t+\Delta t}\right) + D_{j-1}\left(C_{j-1}^{t+\Delta t} - C_j^{t+\Delta t}\right)}{\Delta x^2} \\ &+ \frac{D_{j+1}C_{j+1}^{t+\Delta t}\left(\mu_{j+1}^0 - \mu_j^0\right) - D_j C_j^{t+\Delta t}\left(\mu_j^0 - \mu_{j-1}^0\right)}{2RT\Delta x^2} \\ &+ \frac{D_{j+1}C_{j+1}^{t+\Delta t}F\left(Z_{j+1}^*\phi_{j+1} - Z_j^*\phi_j\right) - D_j C_j^{t+\Delta t}F\left(Z_j^*\phi_j - Z_{j-1}^*\phi_{j-1}\right)}{2RT\Delta x^2}\end{aligned} \tag{2.3}$$

**Note:** A more detailed development of these equations can be found in the Appendix A.

This discretization coupled with the boundary conditions makes it necessary to solve the following system:

$$\begin{bmatrix} C_1^{t+\Delta t} \\ C_2^{t+\Delta t} \\ C_3^{t+\Delta t} \\ \vdots \\ \vdots \\ C_{nn-1}^{t+\Delta t} \\ C_{nn}^{t+\Delta t} \end{bmatrix} = \begin{bmatrix} b_1 & c_1 & 0 & \cdots & \cdots & \cdots & 0 \\ a_2 & b_2 & c_2 & \ddots & & & \vdots \\ 0 & a_3 & b_3 & \ddots & \ddots & & \vdots \\ \vdots & \ddots & \ddots & \ddots & \ddots & \ddots & \vdots \\ \vdots & & \ddots & \ddots & b_{nn-2} & c_{nn-2} & 0 \\ \vdots & & & \ddots & a_{nn-1} & b_{nn-1} & c_{nn-1} \\ 0 & \cdots & \cdots & \cdots & 0 & a_{nn} & b_{\ nn} \end{bmatrix}^{-1} \begin{bmatrix} C_0 \\ C_2^t \\ C_3^t \\ \vdots \\ \vdots \\ C_{nn-1}^t \\ C_0 \end{bmatrix} \tag{2.4}$$

with the generic expression of each term $a_j$, $b_j$, $c_j$ and the 4 boundary conditions terms:

$$\text{for } j = 1,\ b_1 = 1 \text{ and } c_1 = 0 \tag{2.5}$$

$$\text{for } j = 2 \,..\, nn-1,$$

$$a_j = -\frac{\Delta t}{\Delta x^2}\left(D_j^t - \frac{D_{j-1}^t\left(\mu_j^0 - \mu_{j-1}^0 + F(Z_j^*\phi_j - Z_{j-1}^*\phi_{j-1})\right)}{2RT}\right)$$

$$b_j = 1 + \frac{\Delta t}{\Delta x^2}\left(2D_j^t - \frac{D_j^t\left(\mu_{j+1}^0 + \mu_{j-1}^0 - 2\mu_j^0 + F(Z_{j+1}^*\phi_{j+1} + Z_{j-1}^*\phi_{j-1} - 2Z_j^*\phi_j)\right)}{2RT}\right)$$

$$c_j = -\frac{\Delta t}{\Delta x^2}\left(D_j^t + \frac{D_{j-1}^t\left(\mu_{j+1}^0 - \mu_j^0 + F(Z_{j+1}^*\phi_{j+1} - Z_j^*\phi_j)\right)}{2RT}\right) \tag{2.6}$$

$$\text{for } j = nn,\ a_{nn} = 0 \text{ and } b_{nn} = 1 \tag{2.7}$$

$C_0$ in Equation 2.4 is the imposed concentration at abscissas $x = 0$ and $x = L$ where a graphite sheet is in contact with the iron sample in our simulations. We assume that $C_0$ is the maximum C concentration in austenite, as C continuously diffuses from graphite into $\gamma$-iron at thermodynamic equilibrium, as represented on Figure 2.2(a).

The effective charge of C in iron $Z_j^*$ is equal to $Z_\gamma^*$ in austenite and to $Z_\alpha^*$ in ferrite. Different but constant values are considered in each phase. It is assumed that the effective charge of carbon in iron does not depend on the carbon concentration. Within the austenite/ferrite interfaces, the standard chemical potential $\mu_j^0$

is supposed to vary linearly between $\mu_\gamma^0$ and $\mu_\alpha^0$, the values in austenite and ferrite respectively. The effective charge of C in the interface is $Z^*_{\alpha+\gamma} = \frac{Z^*_\alpha + Z^*_\gamma}{2}$. The electrostatic potential $\phi$ can be calculated with the local Ohm law $E = \left\| -\overrightarrow{grad}(\phi) \right\| = \rho \frac{I}{S}$ using the experimental parameters. The electric current $I$ and the sample section $S$ are directly measured before the experiment, where the electric resistivity of iron $\rho$ is calculated thanks to the equation (2.8) proposed by Yafei *et al.* [YAF 09].

$$\rho(T, C) = \alpha + b_1 T + b_2 T^2 + b_3 C^{1/4} \tag{2.8}$$

with $\rho$ in $10^{-6}\,\Omega\,\mathrm{m}$, the carbon concentration $C$ in weight percent, the temperature $T$ in °C, $\alpha = 6.51 \times 10^{-2}\,\Omega\,\mathrm{m}$, $b_1 = 4.74 \times 10^{-4}\,\Omega\,\mathrm{m}\,^\circ\mathrm{C}^{-1}$, $b_2 = 8.89 \times 10^{-7}\,\Omega\,\mathrm{m}\,^\circ\mathrm{C}^{-2}$ and $b_3 = 1.22 \times 10^{-1}\,\Omega\,\mathrm{m}$.

The diffusion coefficients $D_j$ depend on the temperature and the carbon concentration. They are calculated at each node from the equations (2.9) and (2.10) proposed by Ågren [ÅGR 82, ÅGR 86] in ferrite and austenite:

$$\begin{aligned} D^\alpha = {} & 0.02\,\mathrm{m^2\,s^{-1}} \exp\left\{ -\frac{10\,115\,\mathrm{K}}{T} \right\} \\ & \exp\left\{ 0.5898 \left[ 1 + \frac{2}{\pi} \arctan\left( 1.4985 - \frac{15\,309\,\mathrm{K}}{T} \right) \right] \right\} \end{aligned} \tag{2.9}$$

$$\begin{aligned} D^\gamma = {} & 4.53 \times 10^{-7}\,\mathrm{m^2\,s^{-1}} \left[ 1 + y_C\,(1 - y_C)\,\frac{8339.9\,\mathrm{K}}{T} \right] \\ & \exp\left\{ -\left[ \frac{1}{T} - 2.221 \times 10^{-4}\,\mathrm{K^{-1}} \right] (17767 - 26436 y_C) \right\} \end{aligned} \tag{2.10}$$

where $D^\alpha$ and $D^\gamma$ are in $\mathrm{m^2\,s^{-1}}$ with $y_C = \frac{x_C}{1 - x_C}$, $x_C$ being the mole fraction of C, and the temperature $T$ in °C.

As illustrated in Figure 2.10, there are three different domains in our simulation configuration. In the ferrite's domain ($j = ni(3) + 1$ .. $nib(1) - 1$), the diffusion coefficient $D_j$ is $D^\alpha$ (Equation 2.9). In the austenite's domains ($j = 1$ .. $ni(1) - 1$ and $j = nib(3) + 1$ .. $nn$), the diffusion coefficient $D_j$ is $D^\gamma$ (Equation 2.10). In the migrating interfaces ($j = ni(1)$ .. $ni(3)$ and $j = nib(1)$ .. $nib(3)$), the diffusion coefficient $D_j$ is $D^\alpha$ (Equation 2.9) to allow a fast diffusion of C atoms within the interface [MAT 21].

### 2.3.2 Example of results from the model

Figure 2.11 shows an example of modelling ferrite-austenite phase transformation kinetics obtained at 775, 825 and 875 °C. The dashed curves and the plain curves represent the simulated kinetics without electric current and with an electric current ($\sim 300\,\mathrm{A\,cm^{-2}}$) respectively. $d_a$ and $d_c$ are the displacements of phase change's fronts from the anode and from the cathode respectively. Their mean value $\langle d \rangle$ and their difference $\sigma_d$ are calculated as follows:

$$\langle d \rangle = \frac{d_a + d_c}{2} \tag{2.11}$$

$$\sigma_d = d_a - d_c \tag{2.12}$$

| Model parameters | Value or range | Reference |
|---|---|---|
| $D_\alpha$ | $8.32 \times 10^{-11}$ to $4.15 \times 10^{-10}\,\mathrm{m^2\,s^{-1}}$ | [ÅGR 82] |
| $D_\gamma$ | $1.21 \times 10^{-12}$ to $4.61 \times 10^{-11}\,\mathrm{m^2\,s^{-1}}$ | [ÅGR 86] |
| $Z^*_\alpha$ | +3.5 | [NAK 77] |
| $Z^*_\gamma$ | +7.5 | [FAL 70, NAK 78, OKA 70] |

Table 2.2: Nominal values of model parameters (diffusion coefficients and effective charges).

Simulations curves of the $\alpha/\gamma$ phase transformation kinetics plotted in Figure 2.11 are obtained with the nominal values of model parameters obtained in the literature and resumed in Table 2.2. A value range is indicated for the diffusion coefficients as they depend on the carbon concentration and the temperature. The effective charge of C in ferrite and austenite was chosen from the data available in the literature for the temperature range (775 to 875 °C) and the electric current density ($\sim 300\,\mathrm{A\,cm^{-2}}$) considered.

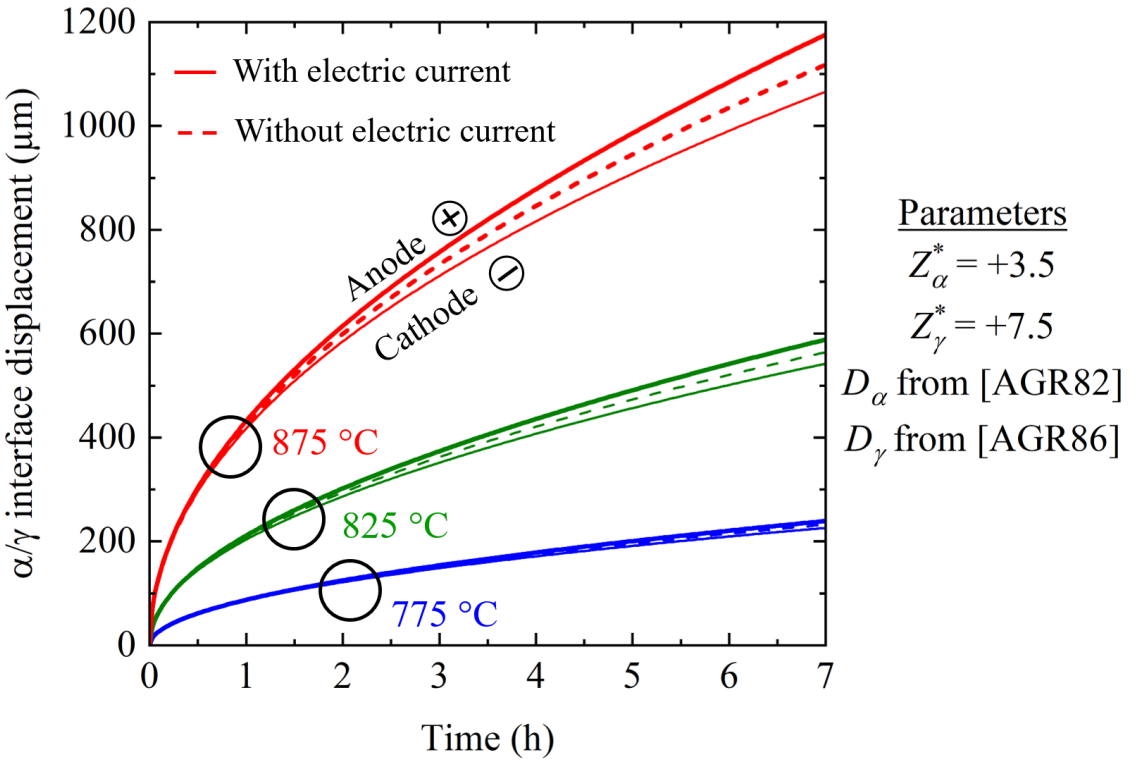


Figure 2.11: Ferrite-austenite phase transformation kinetics described by the displacement of the phase change's fronts (anode and cathode) over time. The dashed curves and the plain curves represent the simulated kinetics without electric current and with an electric current respectively.

### 2.3.3 Model parameters sensitivity study

The influence of our model parameters (the values of the effective charges and the diffusion coefficients of C in iron phases) was examined. Tables 2.3 and 2.4 gathers the results of the "One-At-a-Time" sensitivity study on the influence of these parameters on the phase change kinetics obtained for 7h carburisation simulated at 775, 825 and 875 °C. Simulations were first done with initial input parameters as described previously and the resulting mean displacement $\langle d \rangle$ and difference of displacement $\sigma_d$ of the two $\alpha/\gamma$ interfaces are recorded as nominal output values. When one input parameter ($D^\alpha$, $D^\gamma$, $Z^*_\alpha$ or $Z^*_\gamma$) is modified, the output values may change consequently. The impact of the model parameters on the carburisation kinetics simulated are expressed by the sensitivity coefficients. They are calculated as follows:

$$\frac{\partial\left(\frac{\Delta OUT}{\overline{OUT}}\right)}{\partial\left(\frac{\Delta IN}{\overline{IN}}\right)} \tag{2.13}$$

where $\Delta OUT$ is the variation of one output value (mean $\langle d \rangle$ or difference of displacement $\sigma_d$, in µm) stemmed from $\Delta IN$ the variation of one input parameter (for example the diffusion coefficient of C in ferrite $D^\alpha$), when $\overline{OUT}$ and $\overline{IN}$ are the nominal values of the output and input parameters respectively.

The sensitivity study is used to identify the model parameters (diffusion coefficients and effective charges) that have the greatest impact on the C diffusion and phase transformation kinetics resulting from simulation. The first conclusion from the sensitivity coefficients in Table 2.3 is that only the diffusion coefficient in austenite $D_\gamma$ has a significant influence on the mean displacement of the interfaces $\langle d \rangle$. Indeed, for all temperature studied, $\langle d \rangle$ is 50% larger when $D_\gamma$ is doubled. Diffusion kinetics on both anode and cathode sides are faster with a higher $D_\gamma$ allowing C to reach quicker the migrating interfaces (where phase change occurs). The diffusion of C in austenite is critical for the carburisation kinetics because C atoms have to diffuse from the surface of the sample through austenite first to reach the interface and then to enrich ferrite.

| Inputs | Temperature (°C) | 775 | 825 | 875 |
|---|---|---|---|---|
| (IN) | Equation 2.13 with OUT = $\langle d \rangle$ | Values of sensitivity coefficients | | |
| $D_\alpha$ | $\frac{\partial\left(\frac{\Delta\langle d\rangle}{\langle d\rangle}\right)}{\partial\left(\frac{\Delta IN}{IN}\right)}$ | $1.4 \times 10^{-4}$ | $9.5 \times 10^{-3}$ | $8.6 \times 10^{-4}$ |
| $D_\gamma$ | | $5.0 \times 10^{-1}$ | $5.0 \times 10^{-1}$ | $5.0 \times 10^{-1}$ |
| $Z^*_\alpha$ | | $-2.9 \times 10^{-4}$ | $6.5 \times 10^{-4}$ | $1.6 \times 10^{-3}$ |
| $Z^*_\gamma$ | | $2.4 \times 10^{-3}$ | $2.8 \times 10^{-3}$ | $4.0 \times 10^{-3}$ |

Table 2.3: Sensitivity coefficients of the model parameters (diffusion coefficients and effective charges) on the mean displacement value $\langle d \rangle$.

Secondly, it appears in Table 2.4 that all the model parameters ($D^\alpha$, $D^\gamma$, $Z^*_\alpha$,'$Z^*_\gamma$) have a significative influence on the difference of displacement $\sigma_d$ between anode and cathode interfaces. The sensitivity coefficients for the diffusion coefficient in ferrite $D_\alpha$ and the effective charge of C in ferrite $Z^*_\alpha$ are negative; and they are positive for the diffusion coefficient in austenite $D_\gamma$ and the effective charge of C in austenite $Z^*_\gamma$. The drift velocity of carbon $v_d$ is proportional to the product of $D$ and $Z^*$ (Equation 3). On one hand, higher values of the parameters in ferrite lead to a smaller $\sigma_d$ due to a greater drift velocity of carbon in ferrite $v_{d,\alpha}$. It allows more C to migrate from the anode to the cathode sides and emphasizes the phase transformation kinetics on the cathode. On the other hand, higher values of the parameters in austenite lead to a wider $\sigma_d$. In this case, both the diffusion and the electromigration of C in austenite are enhanced (through $v_{d,\gamma}$). Thus, C atoms reach quickly the $\alpha/\gamma$ interface on the anode side and the phase transformation is enhanced.

| Inputs | Temperature (°C) | 775 | 825 | 875 |
|---|---|---|---|---|
| (IN) | Equation 2.13 with OUT = $\sigma_d$ | Values of sensitivity coefficients | | |
| $D_\alpha$ | $\frac{\partial\left(\frac{\Delta\sigma_d}{\sigma_d}\right)}{\partial\left(\frac{\Delta IN}{IN}\right)}$ | -1.4 | $-7.0 \times 10^{-1}$ | $-4.0 \times 10^{-1}$ |
| $D_\gamma$ | | 2.6 | 1.6 | 1.4 |
| $Z^*_\alpha$ | | -1.4 | $-6.0 \times 10^{-1}$ | $-4.0 \times 10^{-1}$ |
| $Z^*_\gamma$ | | 2.7 | 1.6 | 1.4 |

Table 2.4: Sensitivity coefficients of the model parameters (diffusion coefficients and effective charges) on the difference of interfaces' displacement $\sigma_d$.

In the expression of the drift velocity as a function of the electric current density (Equation 1.14), the variables are: the diffusion coefficient, the effective charge and the electrical resistivity. The latter slightly varies with the temperature and the carbon concentration, from $9.67 \times 10^{-7}$ to $1.28 \times 10^{-6}\,\Omega\,\mathrm{m}$ [YAF 09]. To model the electromigration of C in iron, we chose to adjust the drift velocity of C in austenite $v_{d,\gamma}$ by changing the value of its effective charge $Z^*_\gamma$. There are several reasons for this choice:

1. In our carburisation experiments, the phenomena in austenite appear to be critical in the global kinetics as C atoms have to diffuse from the graphite sheets through austenite to reach the ferrite.
2. The diffusion coefficient of C in austenite will already be set for the mean diffusion of C observed in our experiments.
3. As detailed in the Introduction and the State-of-the-art (Chapter 1) the values of $Z^*_\gamma$ reported in the literature are really scattered for electric current densities lower than $1000\,\mathrm{A\,cm^{-2}}$, which gives us some freedom to adjust this parameter for our experimental conditions.
4. On the contrary, the values of $Z^*_\alpha$ reported in the literature are bounded between +3 and +4 in the intercritical domain.

The conclusion of this study is that the diffusion coefficient of C in austenite $D_\gamma$ is the critical parameter to regulate the carburisation kinetics in our model. In our methodology to compare the model with our experimental results, it is the first parameter to adjust based on the mean value of interface displacement $\langle d \rangle$ to reproduce the experimental kinetics. Then, we chose to adjust the effective charge of C in austenite $Z^*_\gamma$ to model the electromigration of C during our carburisation experiments with electric current based on the difference of interface displacement $\sigma_d$.

### 2.3.4 Key points

- The Gibbs Energy Minimization model developed by Mathevon *et al.* [MAT 21] was adapted to include the effect of the electric current. This model provides the kinetics of carburisation of iron during an isothermal heat treatment assisted by electric current, accounting for the $\alpha \rightarrow \gamma$ transformation and the electromigration of C in iron.
- The diffusion of C in austenite appears to be decisive in the carburisation kinetics as C atoms have to diffuse through austenite to reach the ferrite.
- The **diffusion coefficient of C in austenite** $D_\gamma$ is the critical parameter. In our approach, it is the first parameter to adjust to model the diffusion of C during our experiments based on the mean value of interface displacement $\langle d \rangle$.
- Among the parameters in the expression of the drift velocity, we will focus on the **effective charge of C in austenite** $Z^*_\gamma$ to model the influence of the electric current on the C diffusion and phase transformation kinetics. It will be adjusted according to the difference of interface displacement $\sigma_d$.

# Chapter 3

# Effect of continuous electric current

This chapter aims to study the electromigration of C related with phase transformation in iron submitted to continuous electric current. Heat treatments were performed in AET furnace at three different temperature levels in the intercritical domain. They were first conducted without electric current, and then with intermediate ($\sim 310\,\mathrm{A\,cm^{-2}}$) and maximum ($382\,\mathrm{A\,cm^{-2}}$) current densities. Most of experiments consisted of an isothermal holding of 7 h. Nonetheless, shorter treatments were also performed to compare the evolution of microstructure after 1, 3 and 5 h. These latter tests were conducted without electric current and with maximum current density ($382\,\mathrm{A\,cm^{-2}}$). Details are given for the AET experiments made at 875 °C only. Then, all experimental results are gathered and discussed.

## Contents


**3.1 Experimental ferrite-austenite phase transformation kinetics in the intercritical domain . . . . . 51**

3.1.1 7-hour isothermal holding treatments . . . . . 51

3.1.2 Kinetics study of carburisation at 875 °C . . . . . 56

**3.2 Comparison between simulation and experimental results . 57**

3.2.1 Numerical ferrite-austenite phase transformation kinetics . . 57

3.2.2 C concentration profiles . . . . . 63

**3.3 Discussion . . . . . 65**

3.3.1 Determination of activation energy of C thermal diffusion in austenite . . . . . 65
3.3.2 C diffusion in austenite with electric current . . . . . 67
**3.4 Conclusions . . . . . 70**

## 3.1 Experimental ferrite-austenite phase transformation kinetics in the intercritical domain

### 3.1.1 7-hour isothermal holding treatments

The treated samples are small cylinders of diameter 13 mm and height 6 mm made of ARMCO iron. The contact surfaces of the sample with the electrodes were prepared as described in Section 2.2.3.1. Samples were heated from room temperature to the target temperature (775 °C, 825 °C or 875 °C) at the heating rate of 100 °C/ min. Once the target temperature is reached, it is maintained for one to several hours. Table 3.1 gathers details of the matrix of the different experiments realised in AET furnace.

| **Temperature** (°C) | **Holding time** (h) | **Electric current density** ($A\,cm^{-2}$) |
|---|---|---|
| 775 | 7 | 0<br>314<br>382 |
| 825 | 7 | 0<br>296<br>382 |
| 875 | 1 | 0<br>382 |
| | 3 | 0<br>382 |
| | 5 | 0<br>382 |
| | 7 | 0<br>327<br>382 |

Table 3.1: Experimental conditions of the heat treatments performed in AET furnace

The samples are then cooled freely in vacuum. After cooling, they are cut in half along their height to observe their rectangular cross-section. To look at the microstructure after heat treatment, the samples need to be carefully polished as

described in Section 2.2.3.1. Figure 3.1 shows the microstructure near the cathode and the anode interface respectively, obtained after seven-hour-long treatments at 875 °C, (a) without electric current and (b) with 382 A cm$^{-2}$. On the first look, the two pictures are similar as they are composed of two different zones: one near the interface with a fine dark microstructure, and a central zone made of large ferrite grains. The NITAL chemical etching has revealed the microstructure of the iron samples and a clear separation corresponding to the austenite-ferrite transformation front before cooling can be observed. Thus, the positions of the fronts gives good information on the ferrite-to-austenite phase transformation kinetics. In both cases, the microstructure consists of a mixture of pearlite and ferrite. The cooling rates are rather slow ($\sim$ 60 °C min$^{-1}$) and they depend on the temperature of holding. Thus, no residual austenite or martensite is observed, as ARMCO iron contains few impurities (99.98 % pure).

The fronts' positions measured by image analysis are equal to (670 $\pm$ 40) µm and (560 $\pm$ 40) µm, from the anode and the cathode respectively, without electric current. They are equal to (1050 $\pm$ 40) µm from the anode and (825 $\pm$ 40) µm from the cathode, after heat treatment with 382 A cm$^{-2}$. The influence of the electric current during the holding stage is directly shown by the difference of fronts' positions between the two images.

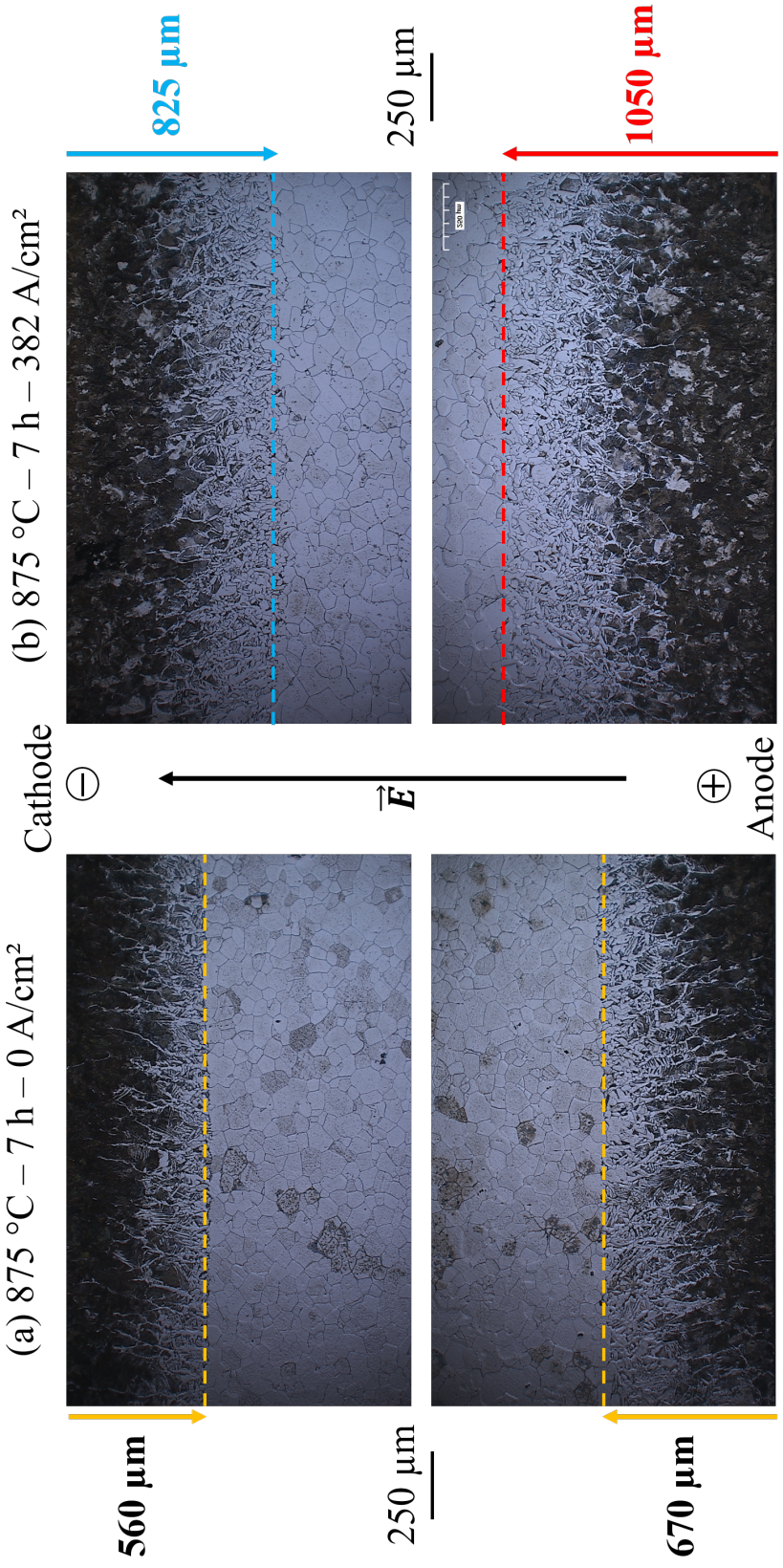


Figure 3.1: Metallography of the sample microstructure perpendicular to the C diffusion direction after a thermal treatment in AET furnace at 875 °C for 7 hours (a) without electric current and (b) with 382 A cm$^{-2}$.

Table 3.2 gathers the measurements of phase change front positions from all 7 hours isothermal holding time heat treatments performed in AET furnace. $d_a$ and $d_c$ are the positions of phase change front measured on the anode side and on the cathode side respectively. Their mean value $\langle d \rangle$ and their difference $\sigma_d$ are calculated as follows:

$$\langle d \rangle = \frac{d_a + d_c}{2} \tag{3.1}$$

$$\sigma_d = d_a - d_c \tag{3.2}$$

| **Temperature** (°C) | 775 | | | 825 | | | 875 | | |
|---|---|---|---|---|---|---|---|---|---|
| **Electric current density** ($\mathrm{A\,cm^{-2}}$) | 0 | 314 | 382 | 0 | 296 | 382 | 0 | 327 | 382 |
| **Cathode front displacement** $d_c$ (µm) | 60 | 150 | 190 | 280 | 390 | 470 | 670 | 550 | 825 |
| **Anode front displacement** $d_a$ (µm) | 130 | 190 | 240 | 185 | 460 | 555 | 560 | 780 | 1050 |
| **Mean value** $\langle d \rangle$ (µm) | 95 | 170 | 215 | 232.5 | 425 | 512.5 | 615 | 665 | 937.5 |
| **Difference** $\sigma_d$ (µm) | 70 | 40 | 50 | -95 | 70 | 85 | -110 | 230 | 225 |

Table 3.2: Experimental phase change front displacements (± 40 µm) measured after 7 hours isothermal holding time heat treatments in the intercritical domain. $\langle d \rangle$ is the mean value of the fronts' displacement (Equation 3.1) and $\sigma_d$ is the difference between the anode and the cathode front displacements (Equation 3.2), in µm.

Looking at the experimental phase change front displacements in Table 3.2, the length of carbon diffusion is larger for higher temperature, as expected as the diffusion is thermally activated (Equations 2.9 and 2.10). Without any electric current, the position mean value $\langle d \rangle$ equals to (95 ± 40) µm at 775 °C and increases up to (615 ± 40) µm at 875 °C. For the heat treatments performed with an electric current density of 382 $\mathrm{A\,cm^{-2}}$, $\langle d \rangle$ grows from (215 ± 40) µm at 775 °C to (937.5 ± 40) µm at 875 °C.

The displacements of the phase change fronts measured from the anode and from the cathode are different for all experimental conditions. Unexpectedly, the difference $\sigma_d$ is not null without electric current. As only thermal diffusion of C occurs in these experiments, the first explanation possible concerns the temperature control during the isothermal holding stage. The deviation observed might be due to a difference of temperature between the top (cathode) and the bottom (anode) of the sample. From our simulations performed for different temperature levels around

825 °C, a deviation of 20 °C leads to a difference of 75 µm in the positions of the $\alpha/\gamma$ interfaces. Yet the two thermocouples measured only 5 °C of difference during the holding stage at 775 °C but $\sigma_d$ is equal to 70 µm. Then, we assume that the initial microstructure of our samples might also contribute. The contact quality between the graphite sheets and the polished surface of the samples can vary too. The phase change front position is clearly visible as the boundary between light initial ferrite and dark mixture of pearlite and ferrite. However, the boundary is not straight and the measurement of its position on the whole sample cross-section can lead to a deviation up to ± 40 µm.

Similar microstructures were observed for each temperature, with a visible gradient of C concentration from pearlite on one side to ferrite in the middle of each sample. The main conclusions from the experimental observations are the following:

- Our experiments showed that the ferrite to austenite phase transformation kinetics is faster in the direction of the electric current (from the anode to the cathode) and hindered in the opposite direction. This is expected with the electromigration phenomenon since the drift velocity is in the same direction as the electric current and the effective charge of C in iron $Z^*$ is positive.

- The mean values of the front displacements $\langle d \rangle$ increase with higher temperature due to increase of the diffusion coefficient. They mainly depend on the value of the diffusion coefficient of C in austenite $D_\gamma$.

- The mean interfaces' displacement $\langle d \rangle$ also increases with higher electric current densities. As seen in Chapter 2, in our model only the diffusion coefficient in austenite $D_\gamma$ has a significant influence on $\langle d \rangle$. Thus, it means that the electric current has an influence on the diffusion of C in austenite. In other words, $D_\gamma$ would be dependent of the current density.

- The difference of front displacements from anode and cathode $\sigma_d$ also increases when the temperature increases. This is expected since this difference is mainly due to the drift velocity which is proportional to the diffusion coefficient (Equation 1.14). The positions of these fronts on the anode and the cathode sides reveals the influence of the electric current on the C diffusion during the heat treatment with Joule effect.

### 3.1.2 Kinetics study of carburisation at 875 °C

The kinetics of ferrite-austenite phase transformation was also studied through shorter heat treatments (1, 3 and 5 h). These latter tests were conducted without electric current and with maximum current density (382 A cm$^{-2}$). Table 3.3 gathers the measurements of phase change front positions after 1 to 7 h isothermal holding time heat treatments performed in AET furnace.

| **Temperature** (°C) | 875 | | | | | | | |
|---|---|---|---|---|---|---|---|---|
| **Time** (h) | 1 | | 3 | | 5 | | 7 | |
| **Electric current density** (A cm$^{-2}$) | 0 | 382 | 0 | 382 | 0 | 382 | 0 | 382 |
| **Cathode front displacement** $d_c$ (µm) | 285 | 325 | 470 | 625 | 590 | 650 | 670 | 825 |
| **Anode front displacement** $d_a$ (µm) | 330 | 395 | 560 | 720 | 650 | 810 | 560 | 1050 |
| **Mean value** $\langle d \rangle$ (µm) | 307.5 | 360 | 515 | 672.5 | 620 | 730 | 615 | 937.5 |
| **Difference** $\sigma_d$ (µm) | 45 | 70 | 90 | 95 | 60 | 160 | -110 | 225 |

Table 3.3: Experimental phase change front positions (± 40 µm) measured after 1 to 7 hours isothermal holding time heat treatments at 875 °C. $\langle d \rangle$ is the mean value of the fronts' displacement (Equation 3.1) and $\sigma_d$ is the difference between the anode and the cathode front displacements (Equation 3.2), in µm.

Table 3.3 reveals that the depth of carbon diffusion is always larger with electric current. After 1 hour of isothermal holding, the position mean value $\langle d \rangle$ equals to (360 ± 40) µm versus (307.5 ± 40) µm at 875 °C, with and without electric current respectively. This gap increases with the duration of heat treatment, reaching (937.5 ± 40) µm versus (615 ± 40) µm after 7 hours with and without current. The difference $\sigma_d$ is not null without electric current. As explained previously, this is due to the experimental conditions including the initial microstructure of ARMCO iron.

## 3.2 Comparison between simulation and experimental results

### 3.2.1 Numerical ferrite-austenite phase transformation kinetics

Tables 3.4 and 3.5 gather the values of our model parameters ($D_\gamma$ and $Z^*$) identified to simulate the isothermal holding heat treatments performed in AET furnace. They were adjusted based on the sensitivity coefficients introduced previously. As the diffusion coefficient of C in austenite $D_\gamma$ depends on the temperature and also the C concentration [ÅGR 86], we indicate the ratio between the identified value and the value predicted by the equation 2.10 given by Ågren. It was adjusted based on the results for 7 hours holding time heat treatments. The measurement uncertainty ($\pm$ 40 µm) leads to various uncertainties on the model parameters' values. Longer treatment times would allow to measure larger C diffusion lengths and to reduce this uncertainty, especially at 775 °C.

| **Temperature** (°C) | 775 | | | 825 | | | 875 | | |
|---|---|---|---|---|---|---|---|---|---|
| **Electric current density** ($A\,cm^{-2}$) | 0 | 314 | 382 | 0 | 296 | 382 | 0 | 327 | 382 |
| **Mean value** $\langle d \rangle$ (µm) | 95 ± 40 | 170 ± 40 | 215 ± 40 | 232.5 ± 40 | 425 ± 40 | 512.5 ± 40 | 615 ± 40 | 665 ± 40 | 937.5 ± 40 |
| **Difference** $\sigma_d$ (µm) | 70 ± 40 | 40 ± 40 | 50 ± 40 | -95 ± 40 | 70 ± 40 | 85 ± 40 | -110 ± 40 | 230 ± 40 | 225 ± 40 |
| **Identified** $\frac{D_\gamma}{D_{Ågren}}$ | 0.17 ± 0.07 | 0.55 ± 0.13 | 0.85 ± 0.16 | 0.18 ± 0.03 | 0.57 ± 0.05 | 0.82 ± 0.06 | 0.31 ± 0.02 | 0.36 ± 0.02 | 0.80 ± 0.03 |
| **Identified** $Z^*_\gamma$ | - | +24 ± 24 | +16 ± 13 | - | +18 ± 10 | +12 ± 6 | - | +36 ± 6 | +16 ± 3 |

Table 3.4: Values of the model parameters that have been fitted from the results of heat treatments 7 hours isothermal holding time heat treatments at 775 °C, 825 °C and 875 °C.

| **Time** (h) | 1 | | 3 | | 5 | | 7 | |
|---|---|---|---|---|---|---|---|---|
| **Electric current density** ($\mathrm{A\,cm^{-2}}$) | 0 | 382 | 0 | 382 | 0 | 382 | 0 | 382 |
| **Mean value** $\langle d \rangle$ (µm) | 307.5 ± 40 | 360 ± 40 | 515 ± 40 | 672.5 ± 40 | 620 ± 40 | 730 ± 40 | 615 ± 40 | 937.5 ± 40 |
| **Difference** $\sigma_d$ (µm) | 45 ± 40 | 70 ± 40 | 90 ± 40 | 95 ± 40 | 60 ± 40 | 160 ± 40 | -110 ± 40 | 225 ± 40 |
| **Identified** $\frac{D_\gamma}{D_{\mathring{A}gren}}$ | 0.43 ± 0.06 | 0.83 ± 0.09 | 0.42 ± 0.03 | 0.87 ± 0.05 | 0.39 ± 0.03 | 0.74 ± 0.04 | 0.31 ± 0.02 | 0.80 ± 0.03 |
| **Identified** $Z^*_\gamma$ | - | +30 ± 17 | - | +15 ± 6 | - | +16 ± 4 | - | +16 ± 3 |

Table 3.5: Values of the model parameters that have been fitted from the results of 1 to 7 hours isothermal holding time heat treatments at 875 °C.

Firstly, as described in 2.3.3, the diffusion coefficient of C in austenite is the first model parameter to be adjusted. It was identified by fitting $\langle d \rangle$ the mean value of the final phase change front positions. The resulting values of diffusion coefficient of C in austenite $D_\gamma$ are different of the ones predicted by Ågren for all experimental conditions. With these values, there is less than 2% of difference between the experimental and predicted (simulation) values of the phase change fronts mean positions. This point is important to ensure the correct description of the thermal diffusion of C in iron. The lowest ratios of $D_\gamma / D_{\mathring{A}gren}$ are 0.17 ± 0.07 at 775 °C, 0.18 ± 0.03 at 825 °C and 0.31 ± 0.02 at 875 °C without any electric current. The diffusion of C in our ARMCO iron samples is apparently slower than the one predicted by Ågren. This could be due to different microstructures. The initial ferrite grain boundaries can rapidly be saturated in carbon, and then the diffusion would occur in the bulk which is much slower. Moreover, the expression for the diffusivity of C in binary Fe-C austenite proposed by Ågren was in fact based on the measurements from Wells *et al.* [WEL 50] in steels containing various concentrations of alloying elements (such as Mn, Si, Cu and Ni). Thus, it is not surprising to find that diffusion coefficient of C in austenite $D_\gamma$ is very different for our experiments (but still in the same order of magnitude).

Furthermore, the diffusion coefficient is increasing with the electric current density for the same temperature level. The ratios of $D_\gamma / D_{\mathring{A}gren}$ for heat treatments with $382\,\mathrm{A\,cm^{-2}}$ are larger than 0.80, which means the identified values are close

to the ones predicted by Ågren. The diffusion of C in iron is clearly enhanced by the presence of electric current, which leads to higher diffusion coefficients of C in austenite $D_\gamma$.

Secondly, the effective charge of C in austenite is identified for all experimental conditions (temperature and electric current density) by fitting $\sigma_d$ the difference between the final phase change front positions. As reported in several studies in the literature, higher electric current densities are associated with lower effective charges of C in austenite $Z^*_\gamma$. For example, it was identified to be $+36 \pm 6$ for $327\,\mathrm{A\,cm^{-2}}$ and $+16 \pm 3$ for $382\,\mathrm{A\,cm^{-2}}$ at 875 °C. However, we cannot conclude about the effect of the temperature on $Z^*_\gamma$. For an electric current density of $327\,\mathrm{A\,cm^{-2}}$, its value remains about the same between $+24 \pm 24$ at 775 °C and $+18 \pm 10$ at 825 °C but it rises to $+36 \pm 6$ at 875 °C.

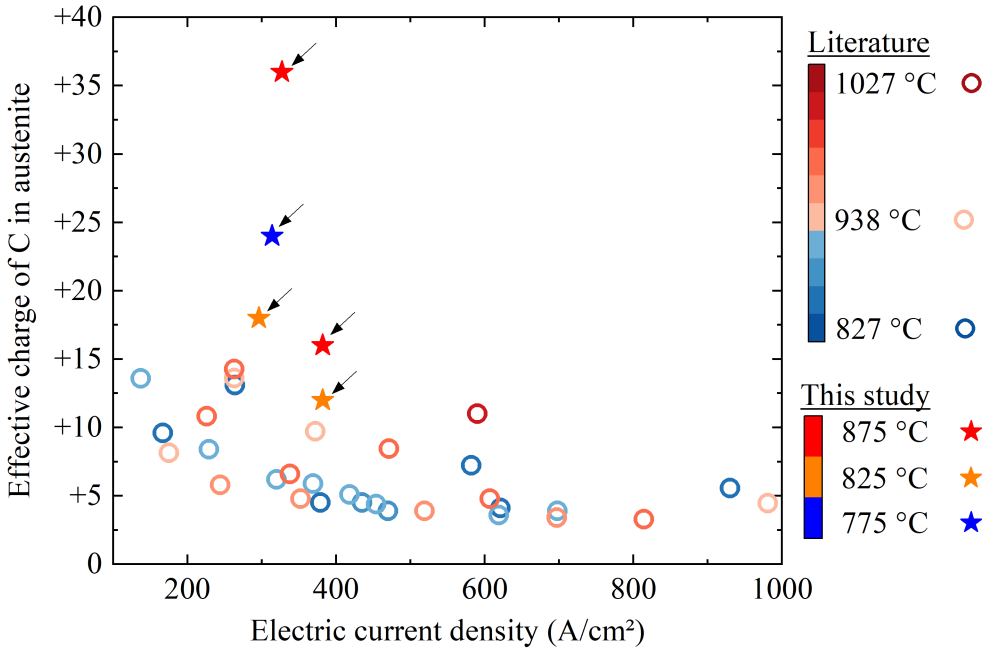


Figure 3.2: Plot of effective charge of carbon in austenite $Z^*_\gamma$ vs. electric current density ($1 \times 10^2$ to $1 \times 10^3\,\mathrm{A\,cm^{-2}}$), at different temperature levels (represented with a color scale). Data from Okabe *et al.* [OKA 70, OKA 73], Nakajima *et al.* [NAK 77, NAK 78], Falquero and Youdelis [FAL 70] are reported as hollow rings. The effective charges we determined based on our experimental results are plotted as solid stars (topped by an arrow).

Figure 3.2 compare our values of effective charge of C in austenite with the val-

ues reported in the literature. We identified an effective charge of $+16 \pm 13$ and $+16 \pm 3$ at 775 °C and 875 °C and $+12 \pm 6$ at 825 °C with an electric current density of $382\,\mathrm{A\,cm^{-2}}$. They are similar to the values +14.3, +13.6 and +13.1 calculated by Falquero and Youdelis [FAL 70] and Nakajima and Hirano [NAK 78]. We also identified $Z_\gamma^*$ to be $+24 \pm 24$, $+18 \pm 10$ and $+36 \pm 9$ at 775 °C, 825 °C and 875 °C respectively with an electric current density around $310\,\mathrm{A\,cm^{-2}}$. The measurements of $Z_\gamma^*$ reported for an electric current density below $1 \times 10^3\,\mathrm{A\,cm^{-2}}$ are really scattered and fluctuate from +7 to +15 for a similar current density. Their dependence on the temperature and the electric current density is uncertain. Moreover, the data available in the literature concerns fully austenite or fully ferrite specimens, whereas our study concerns iron transforming from ferrite to austenite. The effective charge of C is indeed "effective" as it is a physical parameter to represent the apparent behaviour of C submitted to an external electrical force. It is shown to depend on the crystallography, the temperature and the electric current density. The experimental conditions are important to consider as well.

Figure 3.3 compares simulated interfaces positions and C diffusion kinetics versus time at 775 °C, 825 °C and 875 °C with the experimental results. The plain curves represent the simulated kinetics: in black without electric current, in red and green with an electric current density of around $300\,\mathrm{A\,cm^{-2}}$ and $382\,\mathrm{A\,cm^{-2}}$ respectively. Experimental measurements are displayed with the same colour code according to the temperature and the electric current density of heat treatment. Only one point of the kinetics is displayed at the end of the thermal treatment (7 h): plain triangles pointing either up or down are for the final phase change front positions at the anode and at the cathode respectively. Simulations results are obtained with the fitted model parameters $D_\gamma$ and $Z_\gamma^*$ based on the 7-hour-long experiments (Table 3.4).

There is a good agreement between our simulations and experiments results for the three temperature levels. Similar to the experimental observations, the $\alpha/\gamma$ interface on the anode side is always faster than on the cathode side. The difference of their displacement after 7 hours is close to the experimental measurements. A closer look is taken on the figure 3.3(c) which compares the experimental and numerical kinetics at 875 °C. With a ratio of $0.80 \pm 0.03$ for $D_\gamma/D_{\text{Å}gren}$ the diffusion is underestimated for isothermal heat treatments shorter than 7 hours. Adjusted diffusivity ratios have been determined for 1 h, 3 h and 5 h to adjust the intermediate

time kinetics, as shown in Table 3.5.

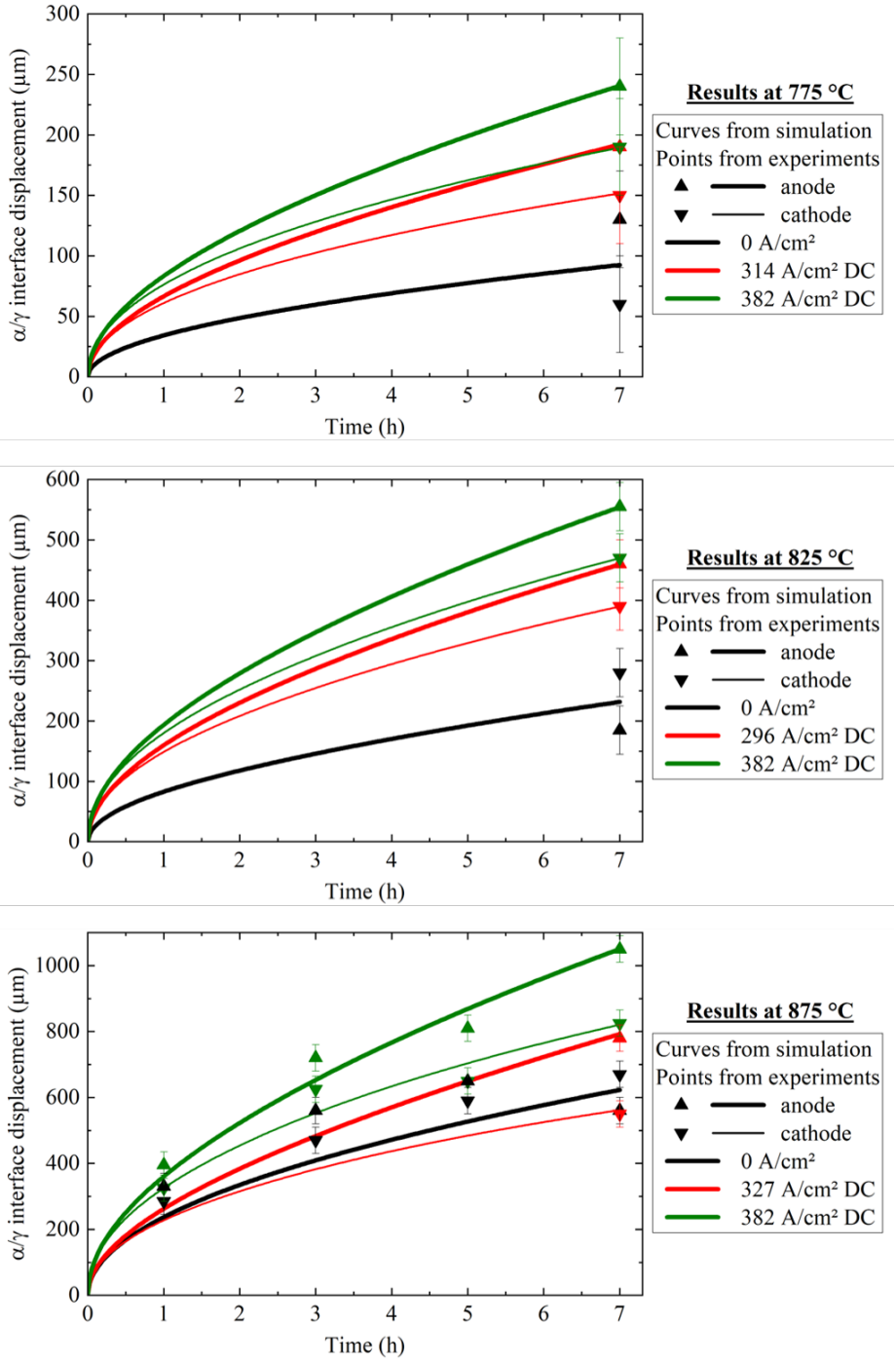


Figure 3.3: Comparison of simulation predicted kinetics (curves) and experimental AET results (triangles) after 7 hours, from the anode and from the cathode. Results for heat treatments without electric current are displayed in black. Thicker lines are used to discriminate the anode's phase change front from the cathode's one.

### 3.2.2 C concentration profiles

The C diffusion profiles obtained from simulation of carburisation at 875 °C between 1-hour and 7-hours are shown on Figure 3.4. Different linestyles are used to represent the profiles obtained at the different times (1, 3 and 5 h). Carburisation with thermal diffusion alone (without electric current) is represented by the black curves. Electric-assisted carburisation is depicted by the red curves for an electric current density of $382\,\mathrm{A\,cm^{-2}}$. The positions of the ferrite/austenite phase transformation interfaces correspond to the C concentration gaps, dropping from around 0.1 to 0.004 wt.% C. These results show a C saturation of the ferrite taking place between 1 hour and 3 hours. When the ferrite is saturated, the front phase change position at the anode moves faster than at the cathode. C diffusion in ferrite is really fast and the influence of electromigration has a much smaller influence during this period. It can be noticed that, without electric current, the ferrite is already saturated after 1 hour of isothermal holding time at 875 °C. In this case, the increase of C concentration near the $\alpha/\gamma$ interface is limited due to a slow diffusion in austenite. Therefore, the phase transformation is also restrained. For this reason, C has more time to enrich ferrite and the saturation happen earlier than when an electric current is applied.

When the ferrite is full of carbon, the C diffusion is mainly driven by its diffusion in austenite, which is 100 times slower than in ferrite. Then the electromigration has a significant influence on the C diffusion and the directional effect arises. Due to the EMG phenomenon, the C diffusion is faster in the direction of the electric current and it is hindered in the opposite. After 7 hours at 875 °C, C has diffused from the anode 510 µm deeper than without electric current. On the other side, C has diffused from the cathode only 155 µm deeper than without electric current. In our experiments, carbons atoms are assumed to behave as metallic cations submitted to an electric force. They are forced to migrate from the anode to the cathode due to the electric current imposed in the electrodes through the sample. Thus, the electric current helps the C diffusion occurring on the anode side but it is opposed to the C diffusing from the cathode.

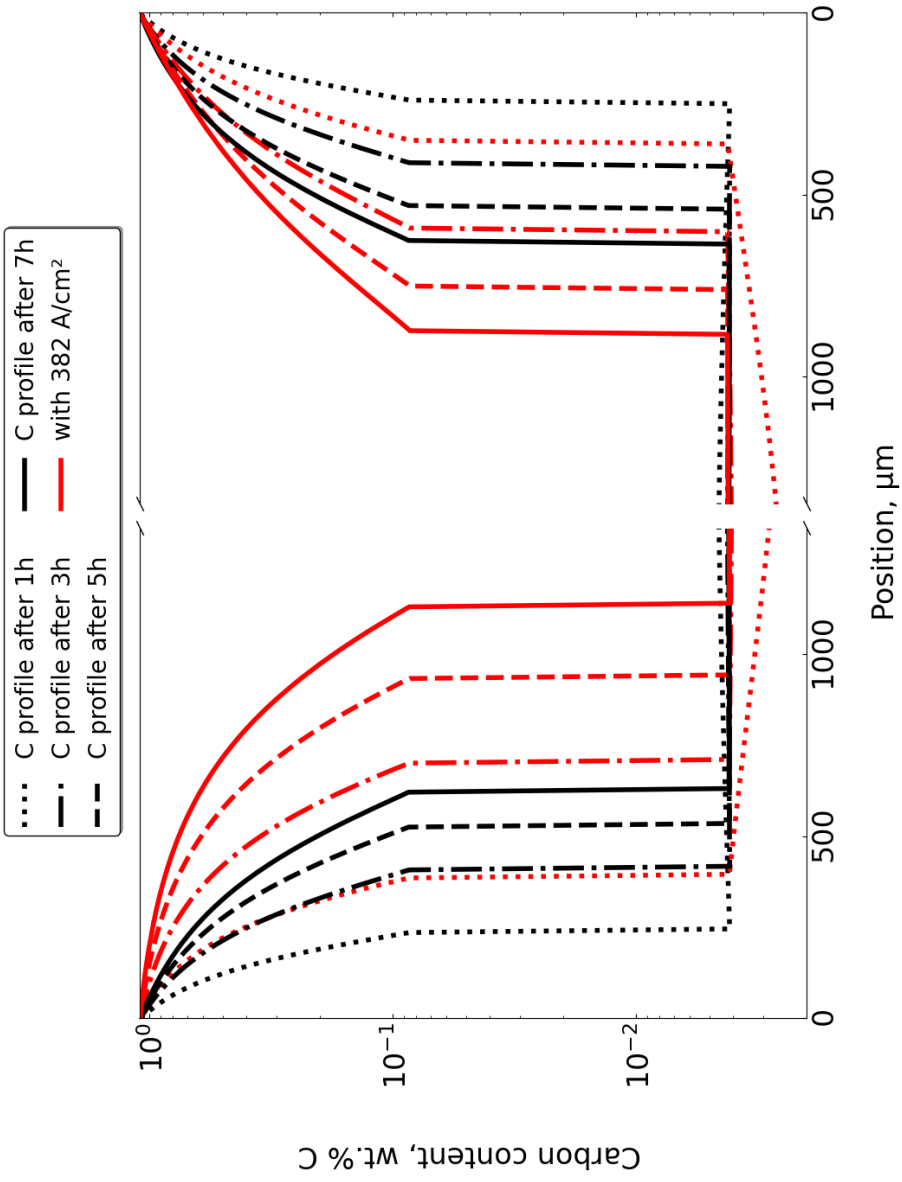


Figure 3.4: Carbon concentration profiles from simulations of carburisation at 875 °C. Different linestyles are used to represent the profiles obtained at different times (1, 3 and 5 h). Black and red lines draw profiles without electric current and with an electric current density of 382 A cm$^{-2}$ respectively.

## 3.3 Discussion

### 3.3.1 Determination of activation energy of C thermal diffusion in austenite

In order to have a better understanding of the physics behind the electromigration of C in iron, it is interesting to study the diffusion in our experiments. The temperature dependence of the diffusion coefficient of carbon in ferrite or austenite can be described by an Arrhenius equation:

$$D = D_0 \exp\left(-\frac{Q}{RT}\right) \tag{3.3}$$

$$\ln(D) = \ln(D_0) - \frac{Q}{RT} \tag{3.4}$$

where $D_0$ is the frequency pre-factor (in $\mathrm{m^2\,s^{-1}}$) and $Q$ the activation energy (in $\mathrm{J\,mol^{-1}}$) for diffusion of C in iron. The latter represents the energy barrier for C atoms to overcome to diffuse in one direction. Its energy level depends on the mechanism of diffusion involved. One way to determine $Q$ is to plot $\ln(D_\gamma)$ vs $1/T$ (Arrhenius plot), which is a straight line if the activation energy $Q$ and the frequency pre-factor $D_0$ are independent of temperature. Its slope gives the value of $-Q/R$ and the activation energy $Q$ can be calculated, knowing that $R$ equals to $8.314\,\mathrm{J\,mol\,K^{-1}}$. The activation energy $Q$ can be converted in eV to compare the energy levels for the diffusion of one atom of C:

$$Q\ (\mathrm{eV}) = \frac{Q\ (\mathrm{J\,mol^{-1}})}{(1.6 \times 10^{-19}\,\mathrm{eV})\,(6.022 \times 10^{23}\,\mathrm{mol^{-1}})} \tag{3.5}$$

In Figure 3.5 are compared the temperature dependence of the diffusion coefficients of C in austenite at 775 °C, 825 °C and 875 °C. First are displayed the values predicted by Ågren (Equation 2.10) [ÅGR 86]. They are calculated for three different carbon concentrations (0.1, 0.5 and 0.89 wt.% C) within the C concentration gradient we observed in austenite (Figure 3.4). Then, the diffusion coefficients based on our experiments without electric current are calculated from the ratios identified previously (Table 3.4). The slopes of the curves associated to the diffusion coefficients of C in austenite $D_\gamma$ predicted by Ågren's equation is clearly different from the ones of the linear regressions based on our data. Then, the calculated activation energies $Q$ are summarised on the right hand side of Figure 3.5.

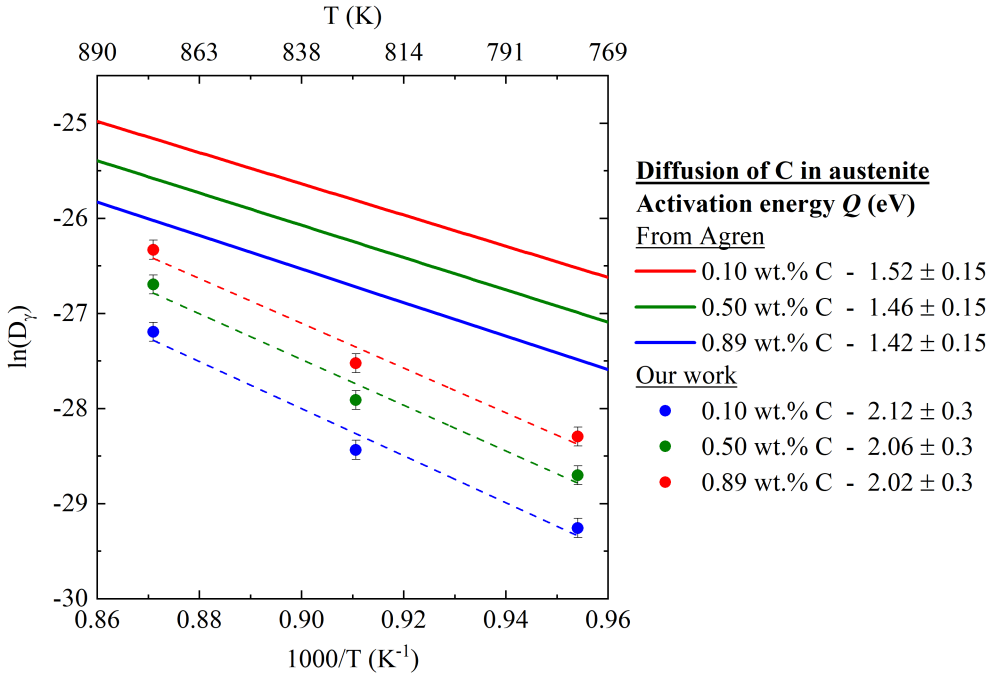


Figure 3.5: Temperature dependence of diffusion coefficient of carbon in austenite. $\ln(D_\gamma)$ is plotted versus $1/T$ to calculate the activation energy $Q$ as given in Equation 3.4. For three different carbon concentrations (0.1, 0.5 and 0.89 wt.% C), the curves plot the values predicted by Ågren (Equation 2.10) [ÅGR 86], while the dots are the values identified in our work with the associated linear regressions as dotted curves.

The activation energy $Q$ based on Ågren's diffusion coefficient of C in austenite $D_\gamma$ via interstitial sites is between $(1.42 \pm 0.15)$ eV and $(1.52 \pm 0.15)$ eV, depending on the carbon concentration. The activation energy of diffusion of C in austenite has been determined by Wells *et al.* [WEL 50] between 1.40 eV and 1.51 eV. Similar values have been reported by Falquero [FAL 70] who calculated an energy of 1.47 eV. However, the temperature dependence of the diffusion coefficients identified from our experimental results is different. Indeed, the slope of the linear regression gives values of activation energies between $(2.02 \pm 0.30)$ eV and $(2.12 \pm 0.30)$ eV. An higher energy barrier means that the diffusion of C is more difficult. There are several explanations for this difference:

- The diffusion coefficients of C in austenite proposed in the literature are ob-

tained from precise diffusion calculations and meticulous experiments. They encompass the diffusion in the volume (bulk) and in the grain boundaries. The diffusion in grain boundaries is faster than the one in the volume. Thus, it leads to a lower energy barrier.

- In fact, the GEM model supposes that the interface mobility is only limited by the C diffusion [MAT 21]. This leads to phase change strongly influence by the C diffusion coefficient in austenite (see the sensitivity study section 2.3.3).However the reconstruction time of the iron lattice during the ferrite-austenite phase transformation and the energy needed for the phase transformation (linked with Fe self diffusion coefficient) are neglected. As the values for the activation energy of Fe self-diffusion are higher than 2.6 eV [MAT 21, ZHA 14, VAS 11, HEU 68], thus the self-diffusion of Fe atoms could contribute indirectly in the activation energy $Q$ that has been determined for carbon diffusion, clearly higher than the value of C diffusion alone.

### 3.3.2 C diffusion in austenite with electric current

Now that we determined the activation energy for diffusion of C in austenite in our samples without electric current, we can compare it with the case of Joule heating. In the present work, the large values of $Z^*_\gamma$ are all positive and they suggest that the electrostatic force is predominant during the electromigration of C in iron. The carbon atoms would not be very sensitive of collisions with the electrons. Then, we determine and discuss the activation energies of diffusion with DC current in the frame of our experimental conditions.

#### 3.3.2.1 Determination of activation energy of C diffusion in austenite with DC current

We consider that the identified ratios of $D_\gamma/D_{Agren}$ for Joule heating treatments is representative of the diffusion of C in austenite enhanced by the electric current (thanks to the EMG). It is very likely to be true since these values are fitted on the results for 7 hours holding time heat treatments with DC current. Then, the previous calculation method (Arrhenius plot) can be used to determine the activation energies $Q_{DC}$ for diffusion of C in $\gamma$-iron with DC current. In Figure 3.6 are compared the calculated activation energies $Q_{DC}$ for diffusion of 0.5 wt.% C in $\gamma$-iron with DC current (up to 382 A cm$^{-2}$) and without any current.

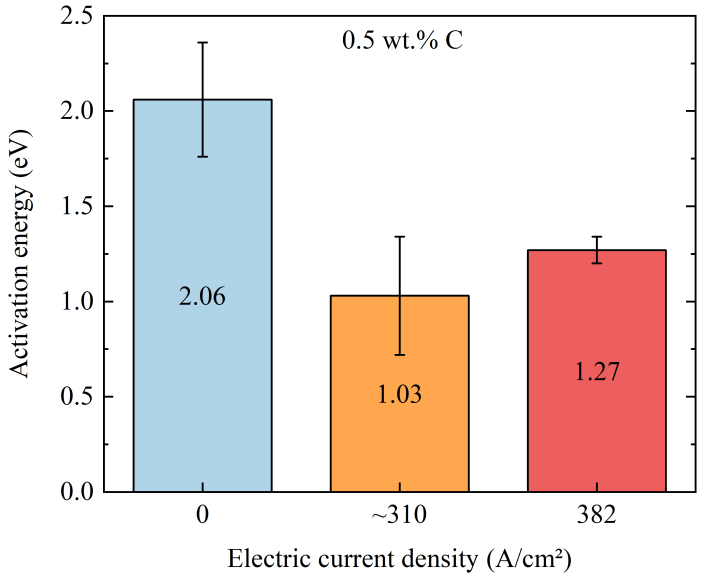


Figure 3.6: Activation energies of carbon (0.5 wt.% C) diffusion in austenite calculated in the case of DC current Joule heating. Data is displayed for the two electric current density ($\sim$ 310 and 382 A cm$^{-2}$) used during our experiments (Table 3.1) and compared with the values calculated for diffusion without electric current.

We found that the activation energy $Q_{DC}$ for C diffusion in austenite with DC current is decreased in presence of DC current, dropping from (2.06 $\pm$ 0.30) eV without electric current to (1.03 $\pm$ 0.31) eV with $\sim$310 A cm$^{-2}$ DC current. Consequently, Joule heating with DC current involves faster C diffusion and $\alpha/\gamma$ phase transformation kinetics because of lower activation barriers for C diffusion in austenite. The increase of current density (up to 382 A cm$^{-2}$) leads to a higher activation barrier. Indeed, a higher electric current density induces a larger electron flow, causing a higher probability of collisions between electrons and C atoms. This could explain a more difficult diffusion of C in austenite as the electric current density intensifies, linked with a larger activation energy barrier. It is confirmed by the identification of lower effective charges $Z^*$ for our experiments involving the highest current densities (Table 3.4).

#### 3.3.2.2 Mechanism of electromigration of C in iron during ferrite-austenite phase transformation

The previous values of activation energies for C diffusion in austenite in presence of DC current are lower than the energy range for interstitial diffusion, determined to be between 1.40 and 1.51 eV [WEL 50, FAL 70, ÅGR 86]. Thus, the electromigration of C in austenite might involve a different mechanism. It already has been proved that the electromigration of Al and Cu atoms involve different contributions: (1) bulk electromigration, (2) grain boundary electromigration, (3) grain/bulk electromigration, (4) defect electromigration, and (5) surface electromigration [SCH 81]. Nakajima and Hirano determined the activation energy of electromigration from the drift velocity for current densities lower than 500 $\mathrm{A\,cm^{-2}}$ [NAK 78]. Then, its value (167.4 kJ/mol = 1.74 eV) indicates that the migration of carbon-vacancy complex contributes to the electromigration of C in $\gamma$-iron. Unfortunately, it was not confirmed by any other author. Hereafter, we discuss possible contributions to C electromigration mechanisms.

**Grain boundary mechanism** Grain boundaries (GB) are known to provide easy paths for mass transport in materials since the energies of defect formation and migration inside them tend to be lower than in the bulk lattice [HUM 17]. It is the most commonly observed route for solute migration in polycristalline materials. It is also the case in the Fe-C system where C preferentially enriches the grain boundaries of ferrite and austenite. At the atomic level, carbon diffuses through the void spaces in regular Fe host lattice by interstitial diffusion in austenite whereas in GB, C diffuses through regular or irregular spaces between Fe atoms by interstitialcy mechanism (jumping to an already occupied interstitial site) [SØR 00]. The diffusivity of C along grain boundaries of $\alpha$-iron is three to four times higher than inside the grain [BOK 61]. Nevertheless, the solubility of C in ferrite grains and their boundaries is very limited. Then the $\alpha/\gamma$ phase transformation occurs and new austenite grains are formed. We assume that the heat treatments we performed are long enough for austenite grain boundaries to be also saturated. Then, the grain boundary mechanism should not be the main mechanism for C electromigration.

**Dislocation mechanism** The diffusion of C into $\gamma$-iron can induce lattice strain and the edge dislocations are created in order to relax the strain. Dislocations are

usually believed to significantly accelerate solute diffusion [HOC 96]. Even at low temperature, the diffusion coefficients along dislocation cores are several orders of magnitude higher than those for bulk lattice diffusion in a perfect crystal. It is known as the dislocation pipe diffusion, which is attributed to a reduced activation barrier of diffusion [LOV 64, BAL 70], less than 50% of the initial energy for diffusion of interstitial elements. It would be due to the distorted atomic structure or the presence of vacancies at the dislocation core [HUA 89], which may reduce the binding energy of C atoms with the surrounding atoms and increase the atomic jump frequency. However, the dislocations initially present in our as-drawn ARMCO iron samples rapidly disappear during the heat treatment in the intercritical domain. And we assume that the C concentration gradient within our samples is not enough to induce lattice strain in austenite grains.

**Carbon-vacancy complex mechanism** Vacancies are point defects in a crystal where atoms are missing in the lattice. They occur naturally in all crystalline materials, with no exception of iron and steels. According to the measurement reported by Maringer *et al.*, the activation energy for migration of carbon-vacancy complex is 1.74 eV [NAK 78] (without details about the iron phase considered). Poletaev *et al.* showed with the molecular dynamics method that the migration energy of a vacancy with C in a f.c.c. structure is equal to 0.99 eV [POL 20]. However, Rosato showed with the same method of calculations that the interaction energy of C with a lattice vacancy in $\gamma$-iron is negative (-7 eV) [ROS 89]. This highly negative value indicates the tendency of C to remain in the interstitial position rather than in the substitutional one.

## 3.4 Conclusions

In the present chapter, the effect of continuous (DC) electric current on the C diffusion in iron and the ferrite-austenite phase transformation kinetics was studied in the intercritical domain. Carburisation of ARMCO iron experiments were performed in a dedicated furnace with two heating sources (radiation and Joule heating) in order to uncorrelate the temperature level from the electric current. Isothermal holding treatments were carried out at 775 °C, 825 °C and 875 °C with an electric current density up to 382 A cm$^{-2}$ for 7 hours.

We showed that the ferrite-austenite phase transformation depends mainly on

the carbon diffusion in austenite and its coefficient $D_\gamma$. As expected, it is faster for higher temperature since the diffusion is a thermally activated phenomenon. Thanks to the electromigration, the depth of C diffusion is increased in presence of electric current. Based on the final positions of $\alpha/\gamma$ interfaces, we concluded that the phase transformation kinetics is faster on the anode side, in the direction of the electric current. It is hindered in the opposite direction, on the cathode side. A higher current density increases this difference of kinetics.

The objective of the model developed in this work accounting for the electromigration of C in iron and the ferrite-austenite phase transformation was to determine the values of $D_\gamma$ and $Z^*_\gamma$ based on our experimental results. The diffusion coefficient of C in austenite $D_\gamma$ is increasing with the electric current density for the same temperature level of heat treatment. The effective charge of C in austenite $Z^*_\gamma$ depends on the temperature and the electric current density. It was found equal to $+24 \pm 24/+18 \pm 10/+36 \pm 6$ for DC current density of $\sim 310\,\mathrm{A\,cm^{-2}}$ at 775 °C, 825 °C and 875 °C, respectively. Its value decreases for a higher current density, as $Z^*_\gamma$ is $+16 \pm 13/+12 \pm 6/+16 \pm 3$ at 775 °C, 825 °C and 875 °C for $382\,\mathrm{A\,cm^{-2}}$ DC current. There is a good agreement between our simulations and experiments results for the three temperature levels considered in the intercritical domain, in terms of prediction of $\alpha/\gamma$ phase transformation kinetics and resulting C concentration distribution.

The temperature dependence of $D_\gamma$ identified accounting for our experiments was studied. We found that the activation energy for C diffusion in austenite is decreased in presence of DC current, dropping from $(2.06 \pm 0.30)$ eV without electric current to $(1.03 \pm 0.31)$ eV with $310\,\mathrm{A\,cm^{-2}}$. The increase of current density ($382\,\mathrm{A\,cm^{-2}}$) leads to a higher energy barrier $(1.27 \pm 0.07)$ eV. As the probability of collisions between electrons and C atoms grows, the diffusion of C in austenite is more difficult in the direction of electric current. This is related to the lower effective charges $Z^*_\gamma$ for our experiments involving the highest current densities. However, we could not associate the calculated activation energies of C diffusion with a specific mechanism of C electromigration (assumed to be interstitial).

# Chapter 4

# Electric current's nature effect: Pulsed vs. Direct Current

This chapter aims to compare the effect of Pulsed Direct Current (PDC) and Direct/continuous Current (DC) on the C electromigration related with phase transformation in iron. Heat treatments were performed in SPS at the same three temperature levels (775 °C, 825 °C or 875 °C) in the intercritical domain. The experiments consisted of an isothermal holding of 7 h. Our results are detailed for the experiments made at 825 °C. Then, all experimental results are gathered and discussed.

## Contents


**4.1 Experimental conditions and results . . . . . 74**

**4.2 Comparison between simulation and experimental results . 77**

4.2.1 Numerical ferrite-austenite phase transformation kinetics . . 77

4.2.2 C concentration profiles . . . . . 79

**4.3 Discussion . . . . . 86**

**4.4 Conclusions . . . . . 89**

## 4.1 Experimental conditions and results

The treated samples are rings of inner diameter 40 mm, outer diameter 50 mm and height 6 mm made of ARMCO iron. The contact surfaces of the sample with the electrodes were prepared as described in Section 2.2.3.1. Samples were heated from room temperature to the target temperature (775 °C, 825 °C or 875 °C) at the heating rate of 100 °C min$^{-1}$. Once the target temperature is reached, it is maintained for seven hours. Table 4.1 gathers details of the matrix of the different experiments realised in SPS. We give the root-mean-square (RMS) density of the pulsed electric current used in SPS. It is the value of the DC current that yields the same power dissipation as the time-averaged power dissipation of the PDC current. The RMS value of electric current density is calculated as follows:

$$j_{RMS} = \sqrt{\frac{1}{\tau}\int_0^\tau \left[j(t)\right]^2 dt} \tag{4.1}$$

| **Temperature** (°C) | **Holding time** (h) | **RMS electric current density** (A cm$^{-2}$) | |
|---|---|---|---|
| | | **Pulsed (SPS)** | **Continuous (AET)** |
| 775 | 7 | 311 | 314 |
| 825 | 7 | 293 | 296 |
| 875 | 7 | 324 | 327 |

Table 4.1: Experimental conditions of the 7-hour isothermal holding heat treatments performed with pulsed or continuous current.

At the end of the isothermal holding stage, the samples are then cooled freely in vacuum. After cooling, they are cut in half along their height to observe their rectangular cross-section. To look at the microstructure after heat treatment, the samples need to be carefully polished as described in Section 2.2.3.1. Figure 4.1 shows the microstructure on the cathode and the anode sides obtained after treatments at 825 °C for 7 h (a) with 296 A cm$^{-2}$ DC current and (b) with 293 A cm$^{-2}$ PDC current. The two micrographs are very similar as the microstructure of the samples are both composed of two different zones: one near the interface with a fine dark microstructure, and a central zone made of large ferrite grains. The NITAL chemical etching has revealed the microstructure of the iron samples and a clear separation corresponding to the austenite-ferrite transformation front before cooling can be observed. In both cases, the microstructure consists of a mixture of

pearlite and ferrite and no residual austenite or martensite is observed. The cooling conditions in vacuum are in fact similar in AET furnace and in SPS.

After a 7-hour isothermal holding at 825 °C with 293 A cm$^{-2}$ (PDC), the fronts' positions measured by image analysis are equal to (520 ± 10) µm and (415 ± 10) µm, from the anode and the cathode respectively. They are equal to (460 ± 40) µm from the anode and (390 ± 10) µm from the cathode, after heat treatment with DC current. The difference originated from the electric current's nature used during the holding stage is directly shown by the difference of fronts' positions between the two images. For similar Joule heating (293 A cm$^{-2}$ pulsed current brings the same heating power than 296 A cm$^{-2}$ continuous current) at 825 °C, the $\alpha/\gamma$ phase transformation interface migrates 60 µm and 25 µm deeper with PDC than DC current, from the anode and the cathode respectively.

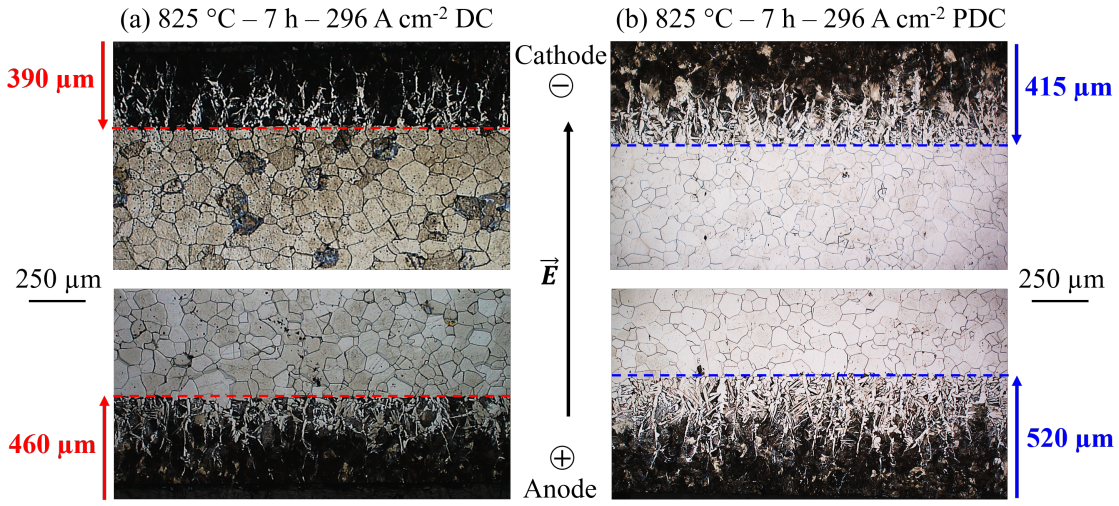


Figure 4.1: Metallography of the samples' microstructures perpendicular to the C diffusion direction after a thermal treatment at 825 °C for 7 h (a) with 296 A cm$^{-2}$ direct current and (b) with 293 A cm$^{-2}$ pulsed current (RMS values of current densities).

Table 4.2 gathers the measurements of phase change front positions resulting from all 7 h isothermal holding time heat treatments performed in AET furnace with DC current and in SPS with PDC current. Three cross-sections of each sample were polished and analysed to measure the fronts' displacement. Once again, in this table, $\langle d \rangle$ is the mean value of the anode front position $d_a$ and the cathode front position $d_c$ , and $\sigma_d$ is their difference.

| **Temperature** (°C) | 775 | | 825 | | 875 | |
|---|---|---|---|---|---|---|
| **Type of electric current** | DC | PDC | DC | PDC | DC | PDC |
| **RMS electric current density** ($A/cm^2$) | 314 | 311 | 296 | 293 | 327 | 324 |
| **Cathode front displacement** $d_c$ (µm | 150 ± 40 | 210 ± 10 | 390 ± 40 | 415 ± 10 | 550 ± 40 | 730 ± 10 |
| **Anode front displacement** $d_a$ (µm) | 190 ± 40 | 255 ± 10 | 460 ± 40 | 520 ± 10 | 780 ± 40 | 1180 ± 10 |
| **Mean value** $\langle d \rangle$ (µm) | 170 ± 40 | 232.5 ± 10 | 425 ± 40 | 467.5 ± 10 | 665 ± 40 | 955 ± 10 |
| **Difference** $\sigma_d$ (µm) | 40 ± 40 | 45 ± 10 | 70 ± 40 | 105 ± 10 | 230 ± 40 | 450 ± 10 |

Table 4.2: Experimental phase change front positions measured after 7 h isothermal holding time heat treatments in the intercritical domain. $\langle d \rangle$ is the mean value of the fronts' displacement (Equation 3.1) and $\sigma_d$ is the difference between the anode and the cathode front displacements (Equation 3.2), in µm.

The thickness of the sample affected by the carbon diffusion is larger for higher temperature, as expected. The diffusion is temperature dependent and the diffusion coefficient of C in iron phases increases with higher temperature levels. Moreover, the position mean value $\langle d \rangle$ with PDC current is always higher than with DC current. It indicates that, for the same temperature of heat treatment, the diffusion of C and the ferrite-austenite phase transformation is faster with PDC current.

The displacements of the phase change fronts measured from the anode and from the cathode are different for all experimental temperatures. Indeed, the difference between the fronts' displacements grows with the temperature. The rise is more pronounced with PDC current, with $\sigma_d$ increasing from (40 ± 10) µm at 775 °C to (450 ± 10) µm at 875 °C.

Similar microstructures were observed for each temperature, with a visible gradient of C concentration from pearlite at the electrode boundary to ferrite in the middle of each sample. The main conclusions from the experimental observations are the following:

- Our experiments showed that the ferrite to austenite phase transformation kinetic is faster in the direction of the electric current (from the anode to the cathode) and hindered in the opposite direction, regardless of the nature of electric current.

- The mean values of the front displacements increase with higher temperature due to increase of the diffusion coefficient. They mainly depend on the value of the diffusion coefficient of C in austenite. For the same electric current density and temperature, $\langle d \rangle$ is higher with pulsed current than with DC current.
- The difference of front displacements from anode and cathode also increases when the temperature increases. This is expected since this difference is mainly due to the drift velocity which is proportional to the diffusion coefficient (Equations (2.9) and (2.10)). It is more pronounced with pulsed current.

## 4.2 Comparison between simulation and experimental results

The simulations described below were carried out with continuous electric current. As described in the experimental conditions at the beginning of this chapter, we assume that the pulsed current of RMS current density (Equation 4.1) induces a Joule effect identical to the direct current of the same density. This choice was made to allow faster simulations because it would constrain the simulation time step too much to reproduce pulsed current with the same frequency as used in SPS experiments (duty ratio 2/3 and frequency 667 Hz). Indeed, a time step of one third of a period ($5 \times 10^{-4}$ s) would be needed.

### 4.2.1 Numerical ferrite-austenite phase transformation kinetics

Table 4.3 gathers the values of our model parameters ($D_\gamma$ and $Z_\gamma^*$) identified to simulate the isothermal holding heat treatments performed in AET furnace with Direct Current (DC) and in SPS with Pulsed Current (PDC). They were adjusted based on the sensitivity coefficients introduced previously. As the diffusion coefficient of C in austenite $D_\gamma$ depends on the temperature and also on the C concentration [ÅGR 86], we indicate the ratio between the identified value and the value predicted by the Equation 2.10 given by Ågren. It was adjusted based on the results for 7 h holding time heat treatments.

Firstly, as described in 2.3.3, the diffusion coefficient of C in austenite is the first model parameter to be adjusted. It was identified by fitting $\langle d \rangle$ the mean

| **Temperature** (°C) | 775 | | 825 | | 875 | |
|---|---|---|---|---|---|---|
| **Type of electric current** | DC | PDC | DC | PDC | DC | PDC |
| **Electric current density** ($\mathrm{A\,cm^{-2}}$) | 314 | 311 | 296 | 293 | 327 | 324 |
| **Mean value** $\langle d \rangle$ (µm) | 170 ± 40 | 232.5 ± 10 | 425 ± 40 | 467.5 ± 10 | 665 ± 40 | 955 ± 10 |
| **Difference** $\sigma_d$ (µm) | 40 ± 40 | 45 ± 10 | 70 ± 40 | 105 ± 10 | 230 ± 40 | 450 ± 10 |
| **Identified** $\frac{D_\gamma}{D_{\text{Å}gren}}$ | 0.55 ± 0.13 | 1.00 ± 0.04 | 0.57 ± 0.05 | 0.69 ± 0.02 | 0.36 ± 0.02 | 0.73 ± 0.01 |
| **Identified** $Z^*_\gamma$ | +24 ± 24 | +17 ± 4 | +18 ± 10 | +25 ± 2 | +36 ± 6 | +39 ± 1 |

Table 4.3: Values of the model parameters that have been fitted from the results of heat treatments 7 h isothermal holding time heat treatments at 775 °C, 825 °C and 875 °C with either pulsed or continuous electric current.

value of the final phase change front positions. The resulting values of $D_\gamma$ are different of the diffusion coefficients predicted by Ågren for almost experimental conditions, except with PDC current at 775 °C. With these values, there is less than 2% of difference between the experimental and predicted (simulation) values of the phase change fronts mean positions. The lowest diffusion coefficients are found for the heat treatments with DC electric current. It is especially marked at 775 and 875 °C where the ratios of $D_\gamma / D_{\text{Å}gren}$ identified for PDC current are almost two times larger than the ones for DC current. The diffusion of C in our ARMCO iron samples is apparently faster with PDC current than with DC current. The initial microstructures are identical and the experimental conditions are similar. Thus, the difference observed should only be due to the electric current's nature. Different mechanisms of diffusion and electromigration C in iron could be involved when PDC current is used to heat the samples.

Secondly, the effective charge of C in austenite $Z^*_\gamma$ is identified for all experimental conditions (temperature, electric current's density and nature) by fitting $\sigma_d$ the difference between the final phase change front positions. The values found for continuous and pulsed current are different at each temperature level; the effective charge $Z^*_\gamma$ identified for PDC current is lower at 775 °C (+17 versus +24) but higher

at 825 and 875 °C. The highest values correspond to the heat treatments at 875 °C with similar values for PDC and DC current. The effective charge of C in austenite clearly increases with a higher temperature level in the case of heat treatments involving pulsed current. The measurements of effective charges of C in austenite $Z^*_\gamma$ reported in the literature for an electric current density below 1000 A cm$^{-2}$ are really scattered and fluctuate from +7 to +15 for a similar current density. Their dependence on the temperature and the electric current density is uncertain. Moreover, the data available in the literature concerns fully austenite or fully ferrite specimens, whereas our study concerns iron transforming from ferrite to austenite. No correlation was found between the nature of electric current used and the value of effective charge.

Figure 4.2 compares simulated interface positions and C diffusion kinetics versus time at 775 °C, 825 °C and 875 °C for heat treatments with pulsed (PDC) or continuous (DC) electric current. Black and coloured curves represent the simulated kinetics without electric current and with an electric current respectively. A colour discrimination is used between results for PDC or DC current. Experimental measurements are displayed with the same colour code according to the temperature and the type of electric current. Only one point of the kinetic is displayed at the end of the thermal treatment (7 h ): plain triangles pointing either up or down are for the final phase change front positions at the anode and at the cathode respectively. Simulations results are obtained with the fitted model parameters ($D_\gamma$ and $Z^*_\gamma$) based on the 7 h experiments (Table 4.3).

There is a good agreement between our simulations and experiments results for the three temperature levels. Similar to the experimental observations, the $\alpha/\gamma$ interface on the anode side is always faster than on the cathode side, for each temperature level. It is more pronounced for heat treatments with pulsed current, where the mean values and the differences of displacement are larger than with continuous current.

### 4.2.2 C concentration profiles

The C diffusion profiles obtained from simulation of carburisation at 825 °C with electric current are shown on Figure 4.3. Different linestyles are used to represent the profiles obtained at different times: dotted lines for 1 hour, dashdotted lines for 3 h, dashed lines for 5 h and solid lines for 7 h. Orange and yellow lines draw

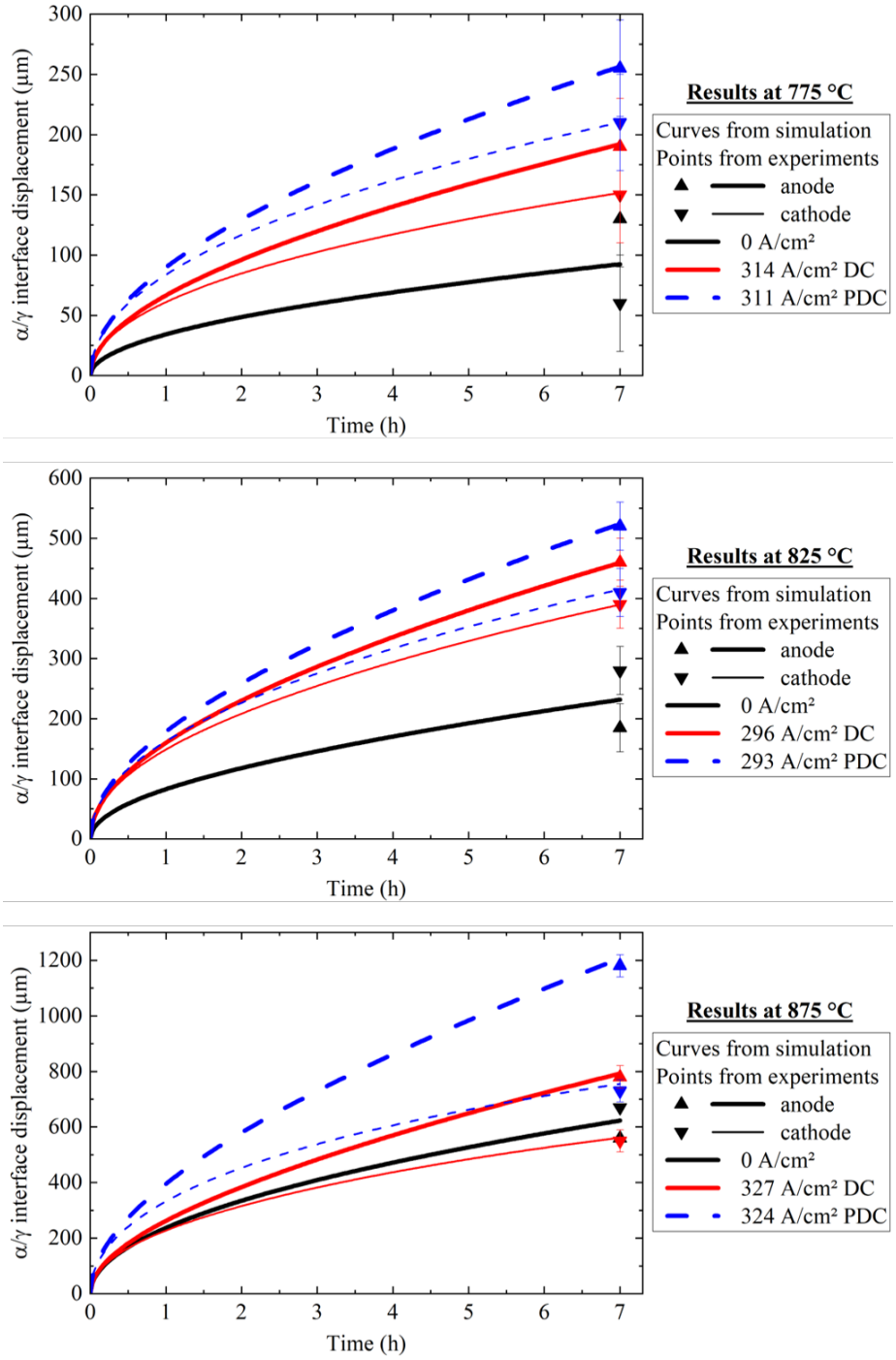


Figure 4.2: Comparison of simulation predicted kinetics (curves) and experimental results (triangles) after 7 h isothermal holding heat treatments with Pulsed Current (PDC) or Direct Current (DC), from the anode and from the cathode. Results for heat treatments without electric current are displayed in black.

profiles with 293 A cm$^{-2}$ DC current and with 296 A cm$^{-2}$ pulsed current density respectively. The positions of the ferrite/austenite phase transformation interfaces correspond to the C concentration gaps, dropping from around 0.25 to 0.01 wt.% C. These results show a C saturation of the ferrite around 3 h. C diffusion in ferrite is really fast and the influence of electromigration has a much smaller influence during this period. When the ferrite is saturated, the front phase change position at the anode moves faster than at the cathode.

Then, the diffusion of C is mainly driven by its diffusion in austenite which is a hundred times slower than in ferrite. Thus, electromigration has a significant influence on the C diffusion and the directional effect arises. It is noticeable on the predicted kinetics in Figure 4.2. The tangent to the curves gives the velocity of the $\alpha/\gamma$ interfaces. It is always higher for the interface on the anode than on the cathode. Moreover, the slope is almost constant between 4 and 7 h for the anode. On the opposite, it slowly decreases for the cathode during this time. Due to the electromigration phenomenon, the C diffusion is faster in the direction of the electric current and it is hindered in the opposite. After 7 h at 825 °C, C from the anode has diffused around 60 µm deeper with pulsed current than with DC current. On the other side, C from the cathode has diffused only 25 µm deeper with pulsed current.

The experimental carbon concentration in samples treated in SPS was estimated in 2 different ways. Image analysis of experimental microstructures was used to quantify pearlite and ferrite phases distribution and calculate the corresponding carbon content, as described in Subsection 2.2.3.2. However, this quantitative method is limited for the highest carbon content near the surfaces of the samples, where cementite can precipitate. In this region, it is difficult to quantify by image analysis because after chemical etching, the cementite lamellas appear as white as ferrite. Electron Probe MicroAnalysis (EPMA) was used to more accurately estimate the C concentration in this region. Vickers micro-hardness measurements were also performed (weight = 0.2 kg, step = 25 µm), as the local hardness is related to the local C concentration.

Figure 4.4 compares the C concentration profiles obtained from simulation (red curves) and from experiment after 7 h of carburisation with electric current at 825 °C. The black diamonds are the micro-hardness measurements also used to observe qualitatively the evolution of the C concentration in the sample. The experimental positions of the ferrite/austenite phase transformation interfaces are easily identified

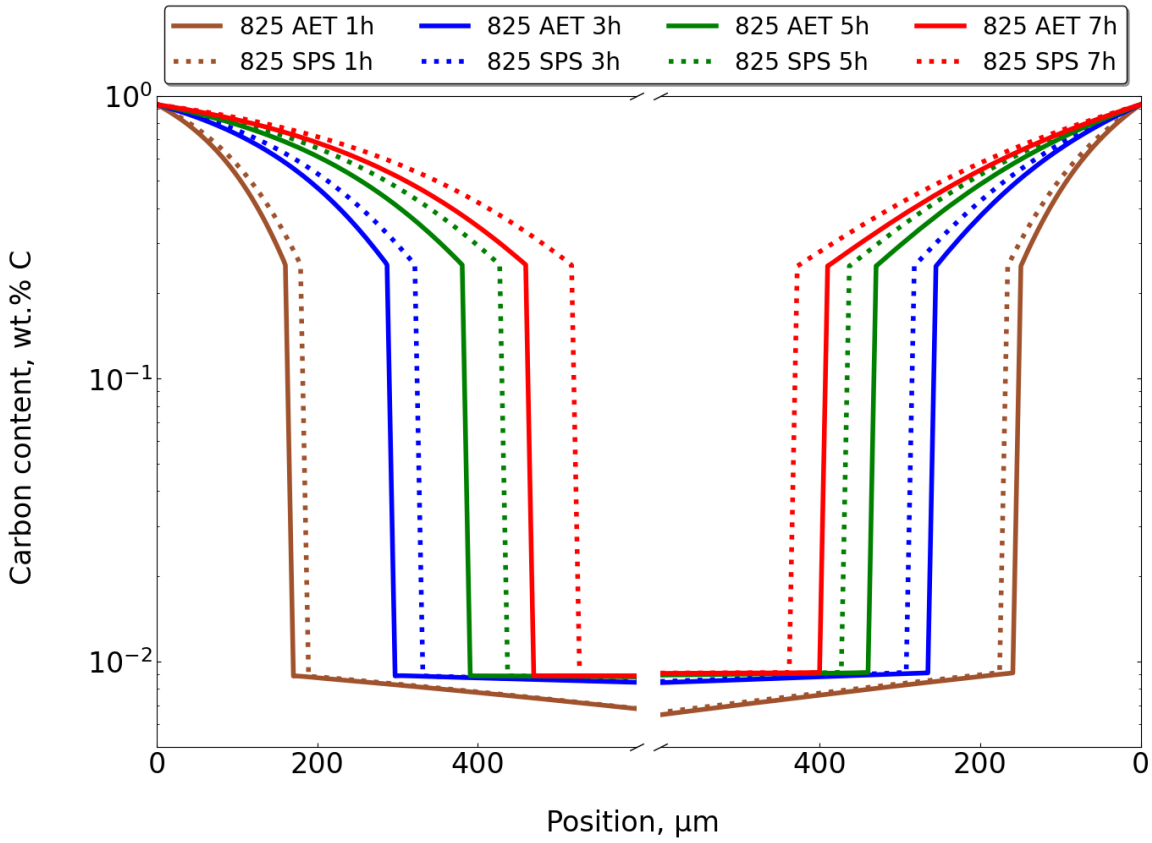


Figure 4.3: Carbon concentration profiles from simulations of carburisation at 825 °C. Different coloured curves are used to represent the profiles obtained at different times (1 h, 3 h, 5 h and 7 h). Solid and dashed lines draw profiles with DC (in AET furnace) and PDC (in SPS machine) currents respectively.

| $T$ (°C) | $C_0$ | $C_0^{'}$ (EPMA) | $D_\gamma/D_{\text{Å}gren}$ | $D_\gamma^{'}/D_{\text{Å}gren}$ | $Z_\gamma^*$ | $Z_\gamma^{*'}$ |
|---|---|---|---|---|---|---|
| 775 | 0.787 | 0.733 ± 0.023 | 1 ± 0.04 | 1.10 ± 0.05 | +17 ± 4 | +14 ± 3 |
| 825 | 0.930 | 0.797 ± 0.023 | 0.69 ± 0.02 | 0.76 ± 0.02 | +25 ± 2 | +25 ± 2 |
| 875 | 1.091 | 0.921 ± 0.023 | 0.78 ± 0.01 | 0.82 ± 0.01 | +39 ± 1 | +41 ± 1 |

Table 4.4: New values of model parameters ($D_\gamma^{'}/D_{\text{Å}gren}$ and $Z_\gamma^{*'}$) with the new boundary condition $C_0^{'}$.

by the C concentration gap dropping from around 0.25 to 0.01 wt.% C, as well as the micro-hardness gap dropping from around (150 ± 40) to (90 ± 40) $HV_{0.2}$. The combination of EPMA (brown square dots) and phase quantification (brown curves) gives quantitative information about the carbon concentration distribution after heat treatment. Simulation and experimental C-profiles are very similar after 7 h. The positions of the $\alpha/\gamma$ interfaces predicted by our model correspond well with the gap of concentration and hardness found experimentally. As expected, the micro-hardness profile in the ferrite in the middle of the sample is flat around (98 ± 40) $HV_{0.2}$. It is in good agreement with the flat C-profile in ferrite predicted by simulation. The ferrite seems also saturated as the hardness value is quite high (typical hardness between 80 and 100 $HV_{0.2}$ for ferrite). The evolution of the carbon content with the depth is comparable between numerical and experimental results.

The microprobe analysis is consistent with the presence of cementite $Fe_3C$ at the electrode boundaries, as the carbon concentration reaches 0.80 wt.% C (higher than 0.77 wt.% C in pearlite alone). As seen in the Fe-C phase diagram (Figure 2.2(a)), when the austenite contains more than 0.77 wt.% C cementite will precipitate during cooling before pearlite appears. The EPMA results could lead us to modify the boundary condition $C_0$ in our simulations, initially set as the maximum C concentration in austenite in contact with graphite (0.93 wt. % C at 825 °C). A slightly lower boundary condition $C_0$ reduces the C concentration gradient and diffusion speed. Thus, the ferrite-austenite phase transformation would be slower. In that case, the model parameters $D_\gamma$ and $Z^*$ identified to match the experimental results might be modified. We expect that $D_\gamma/D_{\text{Å}gren}$ would be increased in this scenario, associated with a lower effective charge $Z^*$.

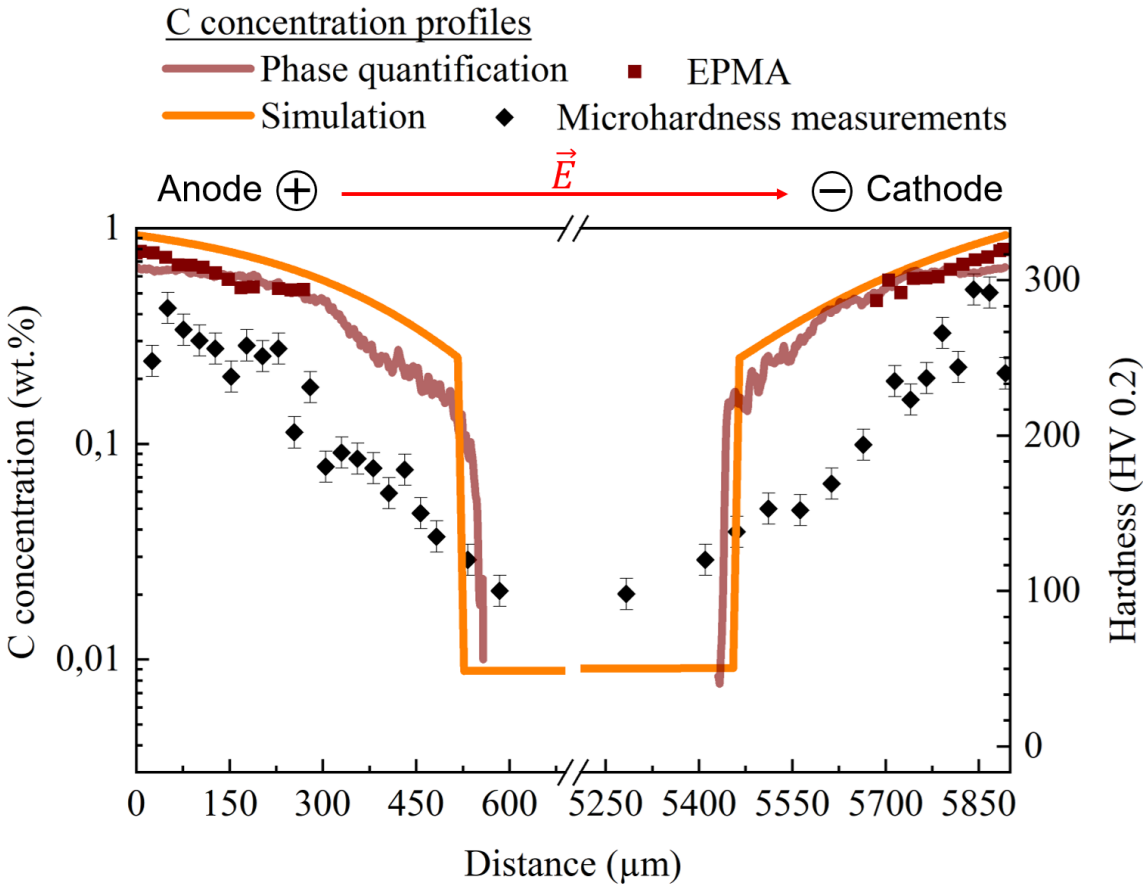


Figure 4.4: Comparison of C profiles after 7 h of carburisation at 825 °C: from simulation (red curve), from phase quantification (brown curve) and from EPMA (brown square dots). Black diamonds are the micro-hardness measurements also used to observe qualitatively the evolution of the C concentration along the section.

Table 4.4 represents this scenario and gathers the new values of the model parameters obtained for these new boundary conditions. In this case, the lower concentrations imposed on the extreme nodes ($j = 1$ and $j = nn$) result in slightly smaller concentration gradients through the sample. As expected, this logically leads to higher diffusion coefficient ratios. Indeed, it is now found to be $0.76 \pm 0.02$ (instead of $0.69 \pm 0.02$) at 825 °C. However, the evolution of the effective charge $Z^*_\gamma$ is not the same at the three different temperature levels. A lower boundary condition leads to a lower $Z^{*'}_\gamma$ at 775 °C ($+14 \pm 3$ instead of $+17 \pm 4$) but a higher value at 875 °C ($+41 \pm 1$ instead of $+39 \pm 1$). This is consistent with the sensitivity study in Chapter 2 Table 2.4 which reveals that the diffusion coefficient of C in austenite has also an influence on the difference of interface displacement between anode and cathode.

## 4.3 Discussion

We propose the same approach than in previous Chapter 3 to study the effect of the electric current's nature on the the C diffusion in our experiments. As a reminder, the temperature dependence of the diffusion coefficient of carbon in ferrite or austenite can be described by an Arrhenius equation:

$$D = D_0 \exp\left(-\frac{Q}{RT}\right) \tag{4.2}$$

$$\ln(D) = \ln(D_0) - \frac{Q}{RT} \tag{4.3}$$

where $D_0$ is the frequency pre-factor (in $\mathrm{m^2\,s^{-1}}$) and $Q$ the activation energy (in $\mathrm{J\,mol^{-1}}$) for diffusion of C in iron. The latter is calculated from the slope of the Arrhenius plot: $\ln(D_\gamma)$ as a function of $1/T$. The activation energy $Q$ can be converted in eV to compare the energy levels for the diffusion of one atom of C:

$$Q\ (eV) = \frac{Q\ (\mathrm{J\,mol^{-1}})}{(1.6 \times 10^{-19}\,\mathrm{J\,eV^{-1}})\,(6.022 \times 10^{23}\,\mathrm{mol^{-1}})} \tag{4.4}$$

The large values of $Z^*_\gamma$ identified for the electric-assisted heat treatments performed are all positive for continuous and pulsed current. They suggest that the electrostatic force is predominant during the electromigration of C in iron in both case. We cannot conclude if C atoms have a different behaviour under the effect of pulses compared to DC current. Then, we determine and discuss the activation energies of diffusion with pulsed current in the frame of our experimental conditions.

We consider that the identified ratios of $D_\gamma/D_{Agren}$ for Joule heating treatments is representative of the diffusion of C in austenite enhanced by the electric current (thanks to the EMG). It is very likely to be true since these values are fitted on the results for 7 h holding time heat treatments with DC current. In Figure 4.5 are compared the calculated activation energies for diffusion of 0.5 wt.% C in $\gamma$-iron with DC and PDC current respectively.

We found that the activation energy for C diffusion in austenite is decreased in a similar way in presence of electric current. Its value calculated with pulsed current (1.13 ± 0.25) eV is similar to the one with continuous current (1.03 ± 0.31) eV. Consequently, Joule heating with pulsed current do not imply faster C diffusion and $\alpha/\gamma$ phase transformation kinetics because of lower activation barriers for C

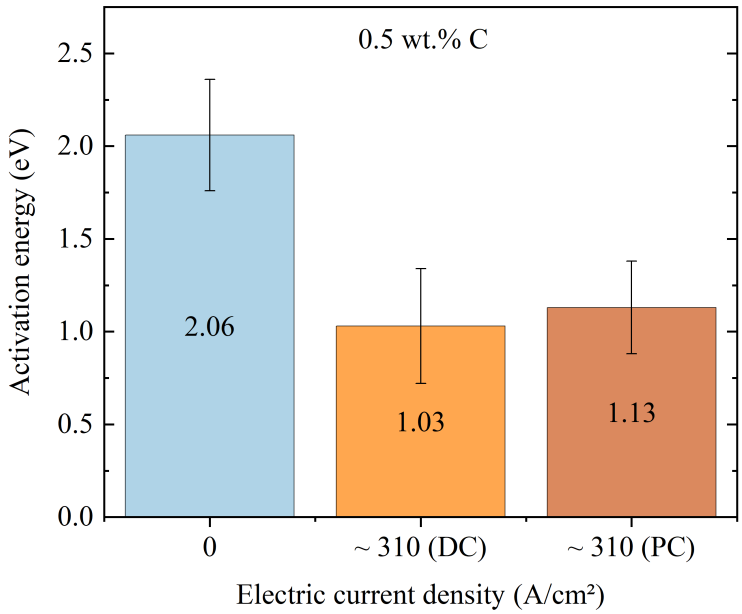


Figure 4.5: Activation energies of carbon diffusion in austenite (0.5 wt.% C) calculated in the case of either continuous (DC) in orange or pulsed (PDC) current Joule heating in brown. They are compared with the values calculated for diffusion without electric current in blue.

diffusion in austenite. The waveform of electric current used in SPS consists of pulses with a frequency of 667 Hz and a duty ratio of 2/3. The RMS current density is indicated in Table 4.2, which implies that the peak density is higher (Equation 4.5. For example, the peak current density used was 359 A cm$^{-2}$ at 825 °C. Thereby, the larger difference between the fronts' positions obtained with pulsed current would come from the higher electric current density inducing a faster electromigration of C in iron.

$$j_{peak} = \frac{j_{RMS}}{\sqrt{2/3}} \tag{4.5}$$

This conclusion is related to the higher diffusion coefficient of C in $\gamma$-iron in the case of heat treatments with pulsed current in Table 4.3. With the RMS intensity of pulsed current equal to intensity of DC current, the pulses of peak intensity lead a stronger electromigration effect on C in iron. When using pulsed current for the same heat treatment, the $\alpha/\gamma$ phase change fronts are faster than with continuous current on both the anode and the cathode sides, and their difference of final positions is

larger as well. The assumption of equivalence between pulsed and direct current only concerns the Joule effect, *i.e.* the heating obtained in the sample. The effect of current pulses, the electromigration of C at higher current densities and the diffusion of C without current in-between pulses are to considered as-well.

Unfortunately, these observations could not be linked with a different mechanism of C electromigration when using pulsed or continuous current. Yet, studies of electropulsing treatments of metals often report accelerated microstructural evolutions through enhanced nucleation and/or recrystallization rates. The two main explanations mentioned for these observations are (1) the interaction of electropulses and drift electrons with dislocations, and (2) the contribution of the electric current to the total free energy $\Delta G_{tot}$.

**Electron-dislocation interactions under pulsed current** Many authors reported an evolution of the dislocation structure in cold-worked metals under electroplastic effect [SPR 86, ZHA 03, DAI 12, XIA 19]. They suggest that the drift electrons influence the generation and motion of dislocations. They would exert a push or "wind" on dislocations, assisting them in overcoming obstacles [GUO 15]:

$$F_{ew} = \alpha \bar{b} p_f \left( j/e - n_e \nu_d \right) \tag{4.6}$$

where $\alpha$ is an adimensional factor (0.25-1.0), $\bar{b}$ is the Burgers vector, $p_f$ is the Fermi momentum, $j$ is the current density, $e$ is the electron charge, $n_e$ is the electron density and $\nu_d$ is the dislocation density.

It leads to improvements in mechanical properties such as tensile strength and elongation [SPR 86]. Song *et al.* showed that the electropulsing treatment (EPT) promotes dislocation movement and annihilation, resulting in a decreased residual stress in cold-rolled M50 steel specimens [SON 20]. Electropulsing was also found to accelerate carbon atoms diffusion and the dissolution of cementite. However, there is no proof that the enhanced motion of dislocation and the faster diffusion of C are related in the case of electropulsing treatments.

**Additional Gibbs free energy** The theory of an additional Gibbs free energy $\Delta G_e$ is often evoked to explain the acceleration of various phenomena in presence of electric current, such as nucleation and recrystallisation [JIN 15, LIU 18] or phase transformation [CON 04, LIU 19, WAN 20]. A theoretical treatment of $\Delta G_e$ was

developed by Qin *et al.*:

$$\Delta G_e = \frac{\mu}{8\pi} \iint \frac{j_1(r)\, j_1(r') - j_2(r)\, j_2(r')}{|r - r'|} d^3r d^3r' \tag{4.7}$$

where $\mu$ is the magnetic permeability, $j$ is the density of electric current, and the sub-indexes 1 and 2 represent the deformed state and recrystallised state of the material, respectively.

By the interactions of electrons with the matter, the electric current would contribute to the total Gibbs free energy of the system. In most cases, the observations were made in deformed materials treated by electropulsing [LI 12, QIN 14, ZHA 03, LU 15]. Thus, the electrical energy would allow earlier and faster nucleation or recrystallisation in deformed materials. There is no link made between these results and the fact that the electric current is pulsed. The authors agree more on the electroplastic effect (well described by Conrad [CON 00b]), which allows the internal stresses of deformed materials to be reduced rapidly by an enhanced dislocations' mobility.

In a review written by Sheng *et al.* [SHE 18], the authors report several studies where phase transition seemed to be facilitated by electropulsing treatment. Comparing the effect of EPT on phase transition with conventional heat treatment, an additional electric Gibbs free energy substantially decreased the apparent solid phase transition temperature of $\alpha + \beta \longrightarrow \alpha'$ in aged AZ91 magnesium alloy strips. Electropulsing ($1.7 \times 10^3\,\mathrm{A\,cm^{-2}}$) also helped with the regeneration (reverse spinodal decomposition in ferrite phase) of aged duplex stainless steel [ZHA 18]. Using the Equation 4.7, the authors estimated the electropulsing-induced extra free energy to be $-891\,\mathrm{J\,mol^{-1}}$. These conclusions are well related to experimental observations but it is difficult to judge the energy calculations due to the lack of transparency about the detailed method. Thus, it is impossible to apply this method to estimate the electrical Gibbs free energy in the case of our carburation experiments with pulsed or direct current.

## 4.4 Conclusions

In the present chapter, the effect of pulsed (PDC) electric current on the C diffusion in iron and the ferrite-austenite phase transformation kinetics was studied in the intercritical domain. In the same way as in the previous Chapter 3, isothermal

holding treatments were carried out at 775 °C, 825 °C and 875 °C with a pulsed electric current density around 310 A cm$^{-2}$ for 7 h.

As expected, the ferrite-austenite phase transformation is faster for higher temperature since the diffusion is a phenomenon thermally activated. Thanks to the electromigration, the depth of C diffusion is increased in presence of pulsed electric current. Similar to the previous results with DC current, it is faster in the direction of the electric current and it is hindered in the opposite direction, on the anode and the cathode side respectively, regardless of the nature of the electric current. A higher current density increases this difference in kinetics. Yet, it is more pronounced with pulsed current than with DC current.

Thanks to the model developed in this work accounting for the electromigration of C in iron and the ferrite-austenite phase transformation in a 1-D system, the values of $D_\gamma$ and $Z^*_\gamma$ for pulsed current were determined based on our experimental results. For a given temperature, the pulsed current was modelled with the same electric charge transfer than during the DC current electromigration (RMS electric density). The diffusion coefficient of C in austenite $D_\gamma$ is found always higher for pulsed current for the same temperature level of heat treatment. The effective charge of C in austenite, $Z^*_\gamma$, is also higher for PDC current than DC current at 825 °C and 875 °C. There is a good agreement between our simulations and experimental results for the three temperature levels considered in the intercritical domain, in terms of prediction of $\alpha/\gamma$ phase transformation kinetics and resulting C concentration distribution. No correlation was found between the nature of electric current used and the value of effective charge. A set of model parameters is not unique to describe the experimental kinetics and C distribution. The phenomenon of electromigration is promoted by the temperature and the density of electric current. In the SPS, the temperature level is adjusted varying the current density. Thus, it is difficult to distinguish the influence of the electron wind and the local Joule heating in the core of the samples.

The temperature dependence of $D_\gamma$ identified accounting for our experiments was studied. We found that the activation energy for C diffusion in austenite is similar for both DC and PDC current, as its value is (1.03 ± 0.31) eV and (1.13 ± 0.25) eV with 310 A cm$^{-2}$ DC and pulsed current respectively. Thereby, the faster $\alpha/\gamma$ phase transformation kinetics observed with pulsed current are not due to a lower energy barrier. It would rather come from the higher electric current density of pulses

inducing a faster electromigration of C in iron. Unfortunately, these observations could not be linked with a different mechanism of C electromigration when using pulsed or continuous current.

# Conclusions and Perspectives

## Conclusions

This PhD-work was carried out as part of the ECUME project aiming at building a modelling framework to describe the evolution of the microstructure of materials during their electrical processing. The goal of ECUME project is to combine dedicated experiments on well-chosen systems and their corresponding simulations to propose the first quantitative prediction tool of the electrical processing of multiphase materials.

The aim of this thesis was to determine the impact of an applied current on the diffusion of C atoms in iron and on the ferrite-to-austenite phase transformation. To study these phenomena, solid carburisation of an ARMCO sample is realised during a thermal treatment in the intercritical domain, in which the C diffusion promotes the ferrite-to-austenite transformation. The sample is heated thanks to Joule effect due to a direct continuous or pulsed electric current. The effect of pulsed current was examined in a Spark Plasma Sintering apparatus, an existing equipment in the MATEIS laboratory, in which the temperature is regulated by the current density. To study the effect of direct current, the design and realisation of a new electromigration experimental set-up was required to be able to uncorrelate the temperature level from the current density. After cooling, the final microstructure of each sample made of pearlite and ferrite (depending on the C concentration) was easily observed after polishing and chemical etching.

A model for the C diffusion accounting for the phase transformation and the electromigration of C in iron has been proposed. In this model, the electric current is taken into account by the current density through the sample. In the case of pulsed current, the root mean square of the current density is considered for comparison with the direct current for an equivalent Joule effect. The sensitivity analysis on the

model parameters showed that the phase transformation kinetics mainly depends on the diffusion coefficient of C in austenite. In addition, the effective charge of C in austenite can be adjusted to model the electromigration of C. Thus, these two parameters were determined based on the comparison between experimental and simulation results.

The experimental observations for DC and pulsed current lead to the same tendencies. It was found that the displacement of the $\alpha/\gamma$ phase change's front is larger in the direction of the electric current. Thus, the phase transformation kinetics is faster in the direction of the electric current and it is hindered in the opposite direction, due to the electromigration phenomenon. This difference of kinetics is increased with a higher current density. Yet, it is even more pronounced with pulsed current than with DC current. As expected, a higher temperature level increased the displacement of the $\alpha/\gamma$ interfaces and therefore the phase transformation kinetics.

The diffusion coefficient and the effective charge of C in austenite were identified for each of the experimental conditions. The C diffusivity seems to depend on the current density since it was found to increase with the latter. Conversely, the effective charge would decrease when the current density is higher, due to the higher probability of collisions between electrons and C atoms. No correlation was found between the nature of electric current used and the value of effective charge. The influence of current on C diffusion in iron is an important new result since previous studies of carbon electromigration assumed a constant diffusion coefficient. Furthermore, the values of the effective charge of C in austenite determined in this study are much higher than those found in the literature.

This PhD-work has endeavoured to demonstrate and improve the understanding of the electromigration of C in iron accounting for the ferrite-to-austenite phase transformation. The model developed can be a quantitative prediction tool for the C concentration in iron during an isothermal holding stage by Joule heating with direct or pulsed electric current. This also allows to predict the microstructural evolutions after cooling thanks to the phase diagram of the Fe-C system. It has been shown that the electric current accelerates the diffusion of carbon into iron and the kinetics of ferrite-to-austenite phase transformation. This could be used advantageously to achieve faster heat treatments in particular. It opens new routes to tailor new microstructures and to improve the process productivity in the metallurgy domain. The anisotropic diffusion of C might be used to create interesting gradients of C,

micro-structure and mechanical properties. The numerical approach proposed in this thesis makes it possible to understand and predict the effect of the electric current on the microstructural evolution of iron alloys, which would allow to better control the effects of current in the processes that rely on the Joule effect.

# Perspectives

To continue and go further in this study, several ways of exploration can be proposed to complete and deepen the characterisation and modelling of the microstructural evolutions of the Fe-C system during an isothermal holding stage by Joule heating. They are organised in two parts: experimental and modelling aspects. Some of the ideas proposed below are based on preliminary test results that have not been presented in the manuscript. Nevertheless, we would like to share them for the many aspects of the study of the effect of electric current in metals.

## To deepen the experimental work

**Model samples** The ARMCO iron was not the ideal model material for the complex study of carbon electromigration in iron. The impurities (C, Mn, P, S) are not negligible if one wishes to study the carburisation of pure iron. The first challenge is to develop model samples to observe the role of different types of defects on electromigration. Pure iron or Fe-C binary alloys could be elaborated while controlling the impurities concentration (C, S, O, N $< 0.0005$ wt.%) and the initial microstructure (such as the grain size, the single or two-phase character or growing columnar grains). Austenitic cast iron (with nickel and chromium) samples could also be used to specifically study the electromigration of carbon into austenite without phase change.

The influence of the grain size on the diffusion and the electromigration of C in iron has already been explored during this thesis. Carburisation experiments were carried out using samples made from an iron as-drawn rod (99.8 % purity) from *Goodfellow* (subsequently referred to as NON-ARMCO iron). The initial microstructure was quite different from the ARMCO iron samples. They presented in particular a finer grain size and visibly larger inclusions, as shown in Figure 4.6.

After a carburisation treatment in the intercritical domain with direct electric current (at 875 °C for 1 h with 382 A cm$^{-2}$), the microstructures obtained after cool-

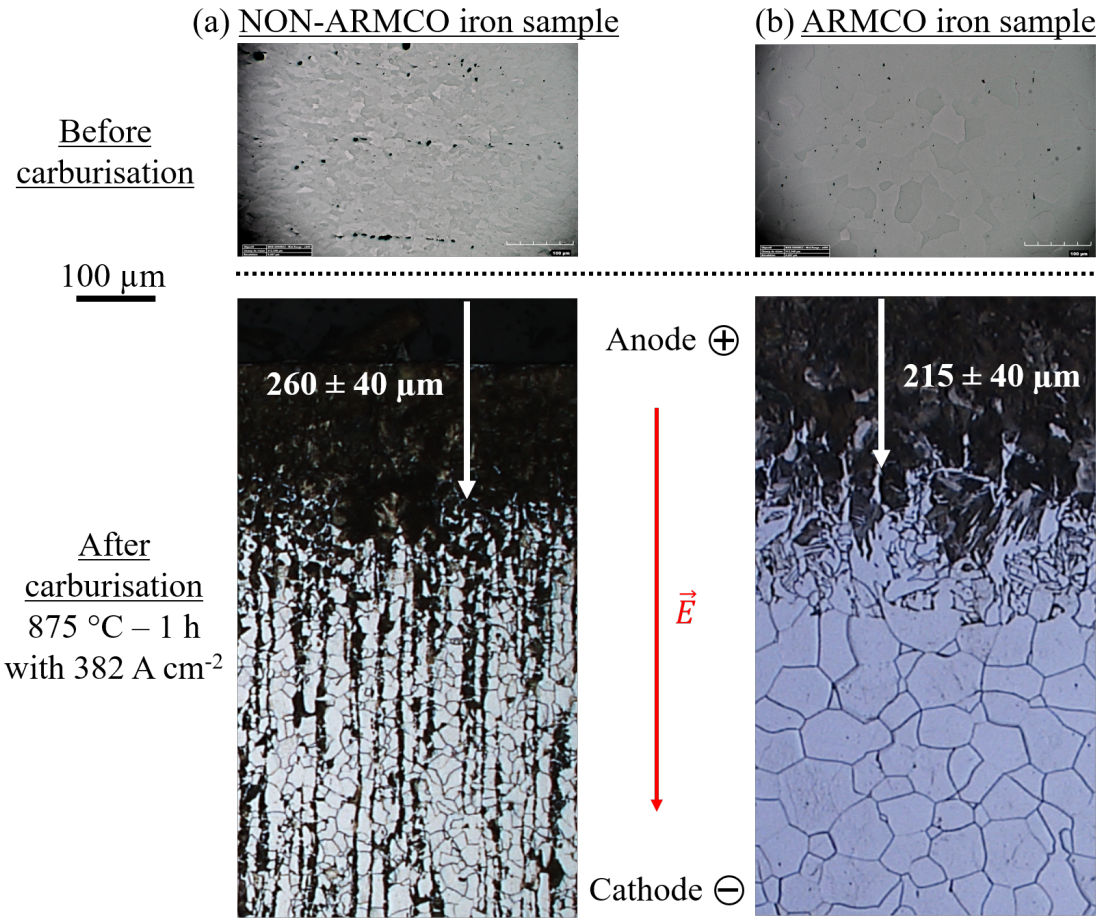


Figure 4.6: Optical micrographs of the microstructures before and after 1 h carburation at 875 °C with 382 A cm$^{-2}$. (a) NON-ARMCO iron sample on the left hand side, compared to (b) ARMCO iron sample on the right hand side.

ing are different. Both samples present fully pearlitic grains in the first 200 µm from the electrode boundary. Then, the distribution of pearlite in the mixture of pearlite and ferrite is not the same. The NON-ARMCO sample has smaller grains and the position of the $\alpha/\gamma$ interface is not as clear as in the ARMCO sample. Moreover, grain boundaries parallel to the direction of the electric current appear to be preferential paths for C diffusion. There is pearlite formed at the grain boundaries throughout the sample.

We assume that C rapidly diffused through the grain boundaries, thereby saturating them. However, the grain size is mainly determined by the grain boundary energy and the enthalpy change of grain boundary segregation [LIU 04]. Grain growth is unfavourable when grain boundaries are saturated. Thus, the growth of austenite grains may have been limited due to the saturation of their boundaries. Modelling the carbon diffusion in 2D (for example with the analytic solution proposed by Suzuoka [SUZ 64]) is necessary to account for this phenomenon. It would even be possible to study the relationship between the grain boundary orientation and the direction of the electric current. The latter may greatly accelerate the diffusion of carbon through the grain boundaries and precipitate their saturation.

**In situ X-ray diffraction** To get better insight of the C diffusion in iron and phase transformation kinetics, carburisation experiments coupled with *in situ* XRD measurements (synchrotron) might be useful. The phase transition can be followed thanks to the bcc to fcc transition. The carbon concentration profile can be obtained since it induces a lattice distortion in bcc and fcc [LEJ 16]. One one hand, the macroscopic mean field measurements would allow to track the average iron phase transformation during the experiments. On the other hand, microscopic measurements on large grains samples can be performed to differentiate inter- and intragranular C diffusion. The results from these experiments, with and without electric current, would be used to identify the electromigration parameters thanks to the model developed in this PhD-work.

On November 2019, preliminary experiments have been carried out in ESRF (without electron beam). They have shown that appropriate experimental conditions can be achieved: temperature from 700 to 950 °C and current densities up to $10^3\,\mathrm{A\,cm^{-2}}$. The experimental device used was the ETMT (Electro-Thermal Mechanical Testing) machine, which is dedicated to study phase change under mechanical stress during thermal treatments in situ followed by X ray diffraction. The

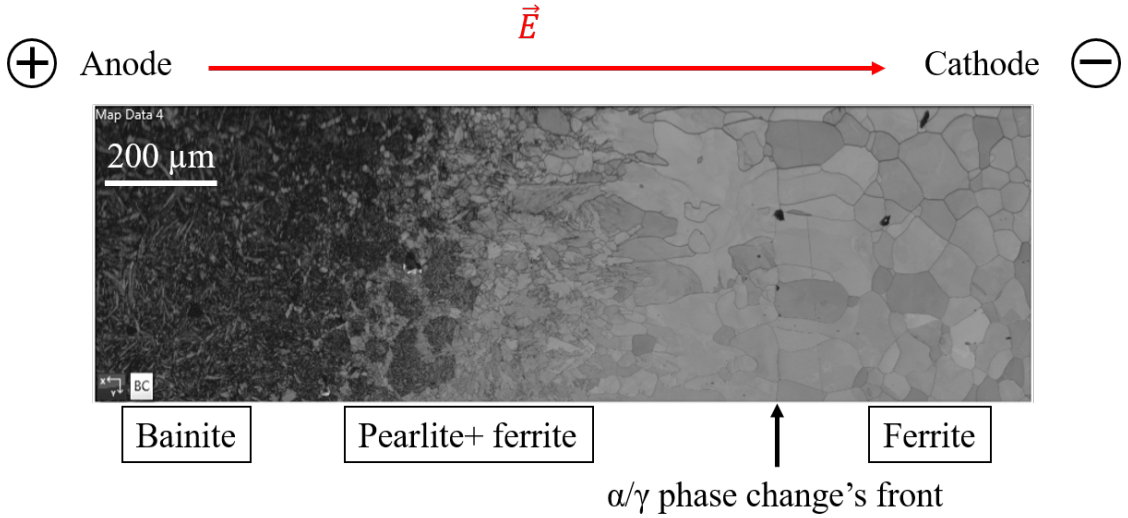


Figure 4.7: Metallography of the sample microstructure perpendicular to the C diffusion direction after a thermal treatment in ETMT machine at 875 °C for 1 h with $10^3$ A cm$^{-2}$.

sample is heated thanks to Joule effect induced by a DC current. The analysis of the sample microstructure after the thermal treatment at 875 °C for 1 h by Joule heating with $10^3$ A cm$^{-2}$ in Figure 4.7 shows that: 1) C diffusion has occurred and induced phase transformation, 2) the volume that has experienced phase change is large enough compared to gauge volume and 3) the grain size allows enough statistic during acquisition.

The microstructure observed is similar to the ones presented in this thesis, with a visible gradient of C concentration from pearlite to ferrite. Surprisingly, on the anode boundary, we also identified bainite formed during rapid cooling of the sample after treatment. Near the $\alpha/\gamma$ phase change's front (identified with an arrow), it is also interesting to note the presence of quite large ferrite grains with a columnar morphology in the direction of the electric current. We assume that it may be due to the presence of electric current. The C saturation of the grain boundaries parallel to the current's direction could lead to this abnormal growth.

However, severe temperature gradients were also observed in the samples during the tests. These were due to the significant heating of the graphite sheets as the current of $10^3$ A cm$^{-2}$ passed through them, causing an additional heating by conduction. Actually the electrical resistivity of graphite larger than the one of

iron. Thus, Joule effect is more important in the graphite sheets. The temperature gradients are due to this Joule effect inhomogeneity and the sample cooling on the electrode side. This phenomenon could be limited by using thinner sheets or graphite glue. Smaller sample cross-sections would also allow a more homogeneous temperature to be achieved.

## Taking modelling further

**Mixed-mode model** The electric current seems to influence the diffusivity of C in austenite. We showed in this thesis that the mobility of the $\alpha/\gamma$ interface is enhanced in the direction of the current. We also found that the activation energy for C diffusion in austenite is lowered in presence of direct or pulsed current. This observation is consistent with the literature where many authors reported an enhanced mobility of dislocations and vacancies with an electric current, as discussed in Chapter 4. The phase transformation's interface is possibly a region rich in crystal defects compared to ferrite and austenite. However, the phenomena that might be located at the interface are not yet captured by our model. This could be overcome by using a Mixed-mode model, in which the transformation is controlled by both the C diffusion and the interface mobility, with its own kinetics. The transformation kinetics is hence managed by the interface velocity which depends on the deviation of the interface conditions from equilibrium as expressed below:

$$v = M_0 \exp\left(-\frac{Q}{RT}\right) \times \chi\left(T\right) \times \left(C_{C,\gamma}^{Int} - C_{C,\gamma}^{Eq}\right) \tag{4.8}$$

with $C_{C,\gamma}^{Int}$ and $C_{C,\gamma}^{Eq}$ corresponding respectively to the interfacial and equilibrium carbon content in austenite. $\chi\left(T\right)$ is a temperature dependent parameter and the interface mobility $M$ is usually assumed to follow an Arrhenius law, with $Q$ the activation energy and $M_0$ a mobility constant. This approach makes it possible to reproduce experimental kinetics [KRI 97, SIE 04, BOS 07, BOS 09, OLL 17], but the mobility applied is characteristic of each system and therefore needs to be adjusted using experimental data.

This could call into question our results and conclusions, especially the influence of the electric current on the C diffusivity in austenite. Based on the comparison of our experimental data and simulations, we concluded that (1) the diffusion coefficient was lower than that predicted by Ågren without electric current and (2) the diffusion

coefficient increased in presence of electric current. It would be interesting to study the diffusion of C in austenite alone without current to verify the first point. Then, the influence of the electric current could be investigated.

**Interactions between electrons and C atoms** There is a real lack of a microscopic understanding of the electromigration and electroplasticity phenomena (linked with quantum mechanics and atomic behavior). It is truly necessary to explore the interactions between electrons and solutes in a metal crossed by electric current.

As a starting point, preliminary observations (graduation project of Sofia Molina Montoya, INSA Lyon) have been carried out using *Ab Initio* calculations of the Mulliken charge of interstitial C in iron. These calculations did not show any significant charge on the C. It suggests that the effective charge has a much more complex physical origin, as already discussed in other studies on electromigration in copper [HAU 04].

Then, one can investigate the dynamics of the defects under an electric current and quantify the affinity of the interstitial C towards the defects. In order to do this, two types of simulations are typically considered:

- Both *Ab Initio* and classical Molecular Dynamics simulations would allow to study the diffusion of defects in pure iron (vacancies, dislocations ...) under the effect of temperature as well as the possible interactions of interstitial C with these defects. However, the investigation of these thermally activated phenomena correspond to long molecular dynamics times for which important computational means are necessary.
- The second type of simulations corresponds to *Ab Initio* calculations considering the effect of an electric field ("Non Equilbrium Green's function technique"). The objective is to observe the influence of the local electric field on the interstitial C (appearance of an effective charge) but also on defects (vacancies, dislocations).

# Appendix A

# Demonstration of equations for C diffusion in Fe in presence of electric current

The conservation law (mass balance) governs the set of equations expressing the temporal evolution of the concentration of carbon in iron. In one (spatial) dimension, it can be written as:

$$\frac{\partial C}{\partial t} = -\frac{\partial J}{\partial x} \tag{A.1}$$

where $C$ is the concentration and $J$ is the flux of carbon in iron.

Fick's first law relates the diffusive flux to the gradient of concentration:

$$J = -D\frac{\partial C}{\partial x} \tag{A.2}$$

with $D$ the diffusion coefficient of C in iron (different in ferrite and in austenite).

Under the assumption of an ideal solution of C in Fe (generally true for low concentrations), its electrochemical potential $\mu$ in molar units is:

$$\mu = \mu^0 + RT \ln C + FZ^*\phi \tag{A.3}$$

where $\mu^0$ is the standard electrochemical potential of C, $R$ is the gas constant, $T$ is the temperature, $F$ is the Faraday constant, $Z^*$ is the effective charge of C and $\phi$ is the local electrostatic potential.

Then, the equations A.2 and A.1 are expressed with the electrochemical potential:

$$J = -D\frac{\partial C}{\partial x} = -C\frac{D}{RT}\frac{\partial \mu}{\partial x} \tag{A.4}$$

$$\frac{\partial C}{\partial t} = -\frac{\partial J}{\partial x} = \frac{\partial}{\partial x}\left[C\frac{D}{RT}\frac{\partial \mu}{\partial x}\right] \tag{A.5}$$

The spatial derivative of the electrochemical potential (equation A.3) is written as following:

$$\frac{\partial \mu}{\partial x} = \frac{\partial \mu^0}{\partial x} + RT\frac{1}{C}\frac{\partial C}{\partial x} + F\frac{\partial\left(Z^*\phi\right)}{\partial x} \tag{A.6}$$

The development continues by combining the two previous equations:

$$\frac{\partial C}{\partial t} = \frac{\partial}{\partial x}\left[C\frac{D}{RT}\left(\frac{\partial \mu^0}{\partial x} + RT\frac{1}{C}\frac{\partial C}{\partial x} + F\frac{\partial\left(Z^*\phi\right)}{\partial x}\right)\right] \tag{A.7}$$

$$\frac{\partial C}{\partial t} = \frac{\partial}{\partial x}\left[C\frac{D}{RT}\frac{\partial \mu^0}{\partial x} + D\frac{\partial C}{\partial x} + C\frac{D}{RT}F\frac{\partial\left(Z^*\phi\right)}{\partial x}\right] \tag{A.8}$$

$$\frac{\partial C}{\partial t} = \frac{\partial C}{\partial x}\frac{D}{RT}\frac{\partial \mu^0}{\partial x} + D\frac{\partial^2 C}{\partial x^2} + \frac{\partial C}{\partial x}\frac{D}{RT}F\frac{\partial\left(Z^*\phi\right)}{\partial x} \tag{A.9}$$

by using that $\frac{\partial^2 \mu^0}{\partial x^2} = 0$, $\frac{\partial D}{\partial x} = 0$ and $\frac{\partial^2\left(Z^*\phi\right)}{\partial x^2} = 0$.

Finally, the diffusion equation accounting for the electromigration is obtained:

$$\frac{\partial C}{\partial t} = \frac{D}{RT}\left[\frac{\partial \mu^0}{\partial x} + F\frac{\partial(Z^*\phi)}{\partial x}\right]\frac{\partial C}{\partial x} + D\frac{\partial^2 C}{\partial x^2} \tag{A.10}$$

The diffusion equation (A.10) is solved using 1-D implicit Finite centered Difference scheme for nodes $j = 2\ ..\ nn-1$.

$$\left.\frac{\partial \mu^0(x)}{\partial x}\right|_{j+\frac{1}{2}} = \frac{\mu^0_{j+1} - \mu^0_j}{\Delta x} \tag{A.11}$$

$$\left.\frac{\partial \mu^0(x)}{\partial x}\right|_{j-\frac{1}{2}} = \frac{\mu^0_j - \mu^0_{j-1}}{\Delta x} \tag{A.12}$$

$$\left.F\frac{\partial(Z^*(x)\phi(x))}{\partial x}\right|_{j+\frac{1}{2}} = F\frac{Z^*_{j+1}\phi_{j+1} - Z^*_j\phi_j}{\Delta x} \tag{A.13}$$

$$\left.F\frac{\partial(Z^*(x)\phi(x))}{\partial x}\right|_{j-\frac{1}{2}} = F\frac{Z^*_j\phi_j - Z^*_{j-1}\phi_{j-1}}{\Delta x} \tag{A.14}$$

$$\left.\frac{C(x)D(x)}{RT}\right|_{j+\frac{1}{2}} = \frac{C_jD_j + C_{j+1}D_{j+1}}{2RT} \tag{A.15}$$

$$\left.\frac{C(x)D(x)}{RT}\right|_{j-\frac{1}{2}} = \frac{C_jD_j + C_{j-1}D_{j-1}}{2RT} \tag{A.16}$$

$$
\begin{aligned}
J^0_{j+\frac{1}{2}} &= \left.\frac{C(x)D(x)}{RT}\right|_{j+\frac{1}{2}} \left( \left.\frac{\partial \mu^0(x)}{\partial x}\right|_{j+\frac{1}{2}} + F \left.\frac{\partial (Z^*(x)\phi(x))}{\partial x}\right|_{j+\frac{1}{2}} \right) \\
&= \frac{C_j D_j + C_{j+1} D_{j+1}}{2RT} \left( \frac{\mu^0_{j+1} - \mu^0_j}{\Delta x} + F \frac{Z^*_{j+1}\phi_{j+1} - Z^*_j \phi_j}{\Delta x} \right)
\end{aligned} \tag{A.17}
$$

$$
\begin{aligned}
J^0_{j-\frac{1}{2}} &= \left.\frac{C(x)D(x)}{RT}\right|_{j-\frac{1}{2}} \left( \left.\frac{\partial \mu^0(x)}{\partial x}\right|_{j-\frac{1}{2}} + F \left.\frac{\partial (Z^*(x)\phi(x))}{\partial x}\right|_{j-\frac{1}{2}} \right) \\
&= \frac{C_j D_j + C_{j-1} D_{j-1}}{2RT} \left( \frac{\mu^0_j - \mu^0_{j-1}}{\Delta x} + F \frac{Z^*_j \phi_j - Z^*_{j-1}\phi_{j-1}}{\Delta x} \right)
\end{aligned} \tag{A.18}
$$

$$
\begin{aligned}
&\frac{C_j^{t+\Delta t} - C_j^t}{\Delta t} = \frac{D_j \left( C^{t+\Delta t}_{j+1} + C^{t+\Delta t}_{j-1} - 2C^{t+\Delta t}_j \right)}{\Delta x^2} + \frac{J^{0,t}_{j+\frac{1}{2}} - J^{0,t}_{j-\frac{1}{2}}}{\Delta x} \\
&\Leftrightarrow C_j^{t+\Delta t} - \frac{\Delta t D_j^t}{\Delta x^2} \left[ C^{t+\Delta t}_{j+1} + C^{t+\Delta t}_{j-1} - 2C^{t+\Delta t}_j \right] - \frac{\Delta t}{\Delta x} \left[ J^{0,t}_{j+\frac{1}{2}} - J^{0,t}_{j-\frac{1}{2}} \right] = C_j^t \\
&\Leftrightarrow C_j^{t+\Delta t} - \frac{\Delta t D_j^t}{\Delta x^2} \left[ C^{t+\Delta t}_{j+1} + C^{t+\Delta t}_{j-1} - 2C^{t+\Delta t}_j \right] \\
&\qquad - \frac{\Delta t}{\Delta x} \left[ \frac{C_j D_j + C_{j+1} D_{j+1}}{2RT} \left( \frac{\mu^0_{j+1} - \mu^0_j}{\Delta x} + F \frac{Z^*_{j+1}\phi_{j+1} - Z^*_j \phi_j}{\Delta x} \right) \right. \\
&\qquad \left. - \frac{C_j D_j + C_{j-1} D_{j-1}}{2RT} \left( \frac{\mu^0_j - \mu^0_{j-1}}{\Delta x} + F \frac{Z^*_j \phi_j - Z^*_{j-1}\phi_{j-1}}{\Delta x} \right) \right] = C_j^t \\
&\Leftrightarrow C_j^{t+\Delta t} - \frac{\Delta t D_j^t}{\Delta x^2} \left[ C^{t+\Delta t}_{j+1} + C^{t+\Delta t}_{j-1} - 2C^{t+\Delta t}_j \right] \\
&- \frac{\Delta t}{2RT\Delta x^2} \left\{ C_j^{t+\Delta t} D_j^t \left[ \mu^0_{j+1} + \mu^0_{j-1} - 2\mu^0_j + F \left( Z^*_{j+1}\phi_{j+1} + Z^*_{j-1}\phi_{j-1} - 2Z^*_j \phi_j \right) \right] \right. \\
&\qquad + C_{j+1}^{t+\Delta t} D_{j+1}^t \left[ \mu^0_{j+1} - \mu^0_j + F \left( Z^*_{j+1}\phi_{j+1} - Z^*_j \phi_j \right) \right] \\
&\qquad \left. - C_{j-1}^{t+\Delta t} D_{j-1}^t \left[ \mu^0_{j+1} - \mu^0_{j-1} + F \left( Z^*_j \phi_j - Z^*_{j-1}\phi_{j-1} \right) \right] \right\} = C_j^t
\end{aligned} \tag{A.19}
$$

This discretization coupled with the boundary conditions makes it necessary to solve the following system:

$$\begin{bmatrix} C_1^{t+\Delta t} \\ C_2^{t+\Delta t} \\ C_3^{t+\Delta t} \\ \vdots \\ \vdots \\ C_{nn-1}^{t+\Delta t} \\ C_{nn}^{t+\Delta t} \end{bmatrix} = \begin{bmatrix} b_1 & c_1 & 0 & \cdots & \cdots & \cdots & 0 \\ a_2 & b_2 & c_2 & \ddots & & & \vdots \\ 0 & a_3 & b_3 & \ddots & \ddots & & \vdots \\ \vdots & \ddots & \ddots & \ddots & \ddots & \ddots & \vdots \\ \vdots & & \ddots & \ddots & b_{nn-2} & c_{nn-2} & 0 \\ \vdots & & & \ddots & a_{nn-1} & b_{nn-1} & c_{nn-1} \\ 0 & \cdots & \cdots & \cdots & 0 & a_{nn} & b_{\ nn} \end{bmatrix}^{-1} \begin{bmatrix} C_0 \\ C_2^t \\ C_3^t \\ \vdots \\ \vdots \\ C_{nn-1}^t \\ C_0 \end{bmatrix} \tag{A.20}$$

with the generic expression of each term $a_j$, $b_j$, $c_j$ and the 4 boundary conditions terms:

$$\text{for } j = 1,\ b_1 = 1 \text{ and } c_1 = 0 \tag{A.21}$$

$$\text{for } j = 2 \,..\, nn-1,$$

$$a_j = -\frac{\Delta t}{\Delta x^2}\left(D_j^t - \frac{D_{j-1}^t\left(\mu_j^0 - \mu_{j-1}^0 + F(Z_j^*\phi_j - Z_{j-1}^*\phi_{j-1})\right)}{2RT}\right)$$

$$b_j = 1 + \frac{\Delta t}{\Delta x^2}\left(2D_j^t - \frac{D_j^t\left(\mu_{j+1}^0 + \mu_{j-1}^0 - 2\mu_j^0 + F(Z_{j+1}^*\phi_{j+1} + Z_{j-1}^*\phi_{j-1} - 2Z_j^*\phi_j)\right)}{2RT}\right)$$

$$c_j = -\frac{\Delta t}{\Delta x^2}\left(D_j^t + \frac{D_{j-1}^t\left(\mu_{j+1}^0 - \mu_j^0 + F(Z_{j+1}^*\phi_{j+1} - Z_j^*\phi_j)\right)}{2RT}\right) \tag{A.22}$$

$$\text{for } j = nn,\ a_{nn} = 0 \text{ and } b_{nn} = 1 \tag{A.23}$$

# References


[ABÉ 06] Abé H., Sasagawa K., Saka M.
Electromigration failure of metal lines. Carpinteri A., Mai Y.-W., Ritchie R. O., Eds., *Advances in Fracture Research*, Dordrecht, 2006 Springer Netherlands, p. 219–240.

[ÅGR 82] Ågren J.
Computer simulations of the austenite/ferrite diffusional transformations in low alloyed steels. *Acta Metallurgica*, vol. 30, n° 4, 1982, p. 841–851.

[ÅGR 86] Ågren J.
A revised expression for the diffusivity of carbon in binary FeC austenite. *Scripta Metallurgica*, vol. 20, n° 11, 1986, p. 1507–1510.

[ALB 13] Albrecht T., Gibb T., Nuttall P.
Ion Transport in Nanopores. *Engineered Nanopores for Bioanalytical Applications: A Volume in Micro and Nano Technologies*, p. 1–30 William Andrew Publishing, jan 2013.

[ASH 17] Ashrafi H., Shamanian M., Emadi R., Saeidi N.
Examination of phase transformation kinetics during step quenching of dual phase steels. *Materials Chemistry and Physics*, vol. 187, 2017, p. 203–217, Elsevier.

[BAL 70] Balluffi R. W.
On measurements of self-diffusion rates along dislocations in F.C.C. Metals. *Physica Status Solidi (B)*, vol. 42, n° 1, 1970, p. 11–34.

[BER 01] Bertolino N., Garay J., Anselmi-Tamburini U., Munir Z. A.
Electromigration effects in Al-Au multilayers. *Scripta Materialia*, vol. 44, n° 5, 2001, p. 737–742.

[BER 02] Bertolino N., Garay J., Anselmi-Tamburini U., Munir Z. A.
High-flux current effects in interfacial reactions in Au/Al multilayers. *Philosoph-*

*ical Magazine B: Physics of Condensed Matter; Statistical Mechanics, Electronic, Optical and Magnetic Properties*, vol. 82, n° 8, 2002, p. 969–985.

[BHA 15] Bhadeshia H. K. D. H.
The Electrical Processing of Materials. *Materials Science and Technology*, vol. 31, n° 13, 2015, p. 1521–1522, Taylor & Francis.

[BHA 17] Bhadeshia H., Honeycombe R.
*Iron-Carbon Equilibrium and Plain Carbon Steels*. Elsevier Ltd, 4 édition, 2017.

[BIE 21] Biesuz M., Saunders T., Ke D., Reece M. J., Hu C., Grasso S.
Invited Review A review of electromagnetic processing of materials (EPM): Heating, sintering, joining and forming. *Journal of Materials Science & Technology*, vol. 69, 2021, p. 239–272.

[BOK 61] Bokshtein S. Z., Gubareva M. A., Kontorovich I. E., Moroz L. M.
Peculiarities of the diffusion of carbon in iron. *Metal Science and Heat Treatment of Metals*, vol. 3, n° 1-2, 1961, p. 6–9.

[BOS 62] Bosvieux C., Friedel J.
Sur l'électrolyse des alliages métalliques. *Journal of Physics and Chemistry of Solids*, vol. 23, 1962, p. 123–136.

[BOS 07] Bos C., Sietsma J.
A mixed-mode model for partitioning phase transformations. *Scripta Materialia*, vol. 57, n° 12, 2007, p. 1085–1088.

[BOS 09] Bos C., Sietsma J.
Application of the maximum driving force concept for solid-state partitioning phase transformations in multi-component systems. *Acta Materialia*, vol. 57, n° 1, 2009, p. 136–144.

[BRA 20] Bram M., Laptev A. M., Mishra T. P., Nur K., Kindelmann M., Ihrig M., Pereira da Silva J. G., Steinert R., Buchkremer H. P., Litnovsky A., Klein F., Gonzalez-Julian J., Guillon O.
Application of Electric Current-Assisted Sintering Techniques for the Processing of Advanced Materials. *Advanced Engineering Materials*, vol. 22, n° 6, 2020, Wiley-VCH Verlag.

[CHE 98] Chen S.-W., Chen C.-M., Liu W.-C.
Electric current effects upon the Sn/Cu and Sn/Ni interfacial reactions. *Journal of Electronic Materials*, vol. 27, n° 11, 1998, p. 1193–1199.

[CHE 99] Chen C.-M., Chen S.-W.
Electric currents effects on Sn/Ag interfacial reactions. *Journal of Electronic Materials*, vol. 28, n° 7, 1999, p. 902–906.

[CHE 00] Chen C.-M., Chen S.-W.
Electromigration effect upon the Zn/Ni and Bi/Ni interfacial reactions. *Journal of Electronic Materials*, vol. 29, n° 10, 2000, p. 1222–1228.

[CHE 14] Chen H., Van Der Zwaag S.
A general mixed-mode model for the austenite-to-ferrite transformation kinetics in Fe-C-M alloys. *Acta Materialia*, vol. 72, 2014, p. 1–12.

[CHI 11] Chiu Y. T., Liu C. H., Lin K. L., Lai Y. S.
Supersaturation induced by current stressing. *Scripta Materialia*, vol. 65, n° 7, 2011, p. 615–617.

[CHI 13] Chiu Y.-T., Lin K.-L., Wu A. T., Jang W.-L., Dong C.-L., Lai Y.-S.
Electrorecrystallization of Metal Alloy. *Journal of Alloys and Compounds*, vol. 549, 2013, p. 190–194, Elsevier.

[CHR 02] Christian J. W.
*The theory of transformations in metals and alloys.* Newnes, 2002.

[CON 00a] Conrad H.
Effects of electric current on solid state phase transformations in metals. *Materials Science and Engineering: A*, vol. 287, n° 2, 2000, p. 227–237, Elsevier.

[CON 00b] Conrad H.
Electroplasticity in metals and ceramics. *Materials Science and Engineering: A*, vol. 287, n° 2, 2000, p. 276–287, Elsevier.

[CON 04] Conrad H., Jung K.
Effects of an Electric Field and Current on Phase Transformations in Metals and Ceramics. *Materials and Manufacturing Processes*, vol. 19, n° 4, 2004, p. 573–585.

[DAI 12] Dai W., Wang X., Zhao H., Zhao X.
Effect of electric current on microstructural evolution in a cold-rolled 3% Si steel. *Materials Transactions*, vol. 53, n° 1, 2012, p. 229–233.

[DOL 93] Dolinsky Y., Elperin T.
Thermodynamics of phase transitions in current-carrying conductors. *Physical Review B*, vol. 47, n° 22, 1993, p. 14778–14785.

[FAB 14] Fabrègue D., Mouawad B., Hutchinson C. R.
Enhanced recovery and recrystallization of metals due to an applied current. *Scripta Materialia*, vol. 92, 2014, p. 3–6.

[FAL 70] Falquero E. A., Youdelis W. V.
Field dependence of carbon electrotransport in gamma iron. *Canadian Journal of Physics*, vol. 48, 1970, p. 1984–1990.

[FEL 53] Feltham P.
The Plastic Flow of Iron and Plain Carbon Steels above the A 3 -Point. *Proceedings of the Physical Society. Section B*, vol. 66, n° 10, 1953, p. 865–883, IOP Publishing.

[FIK 59] Fiks V. B.
On the mechanism of the mobility of ions in metals. *Soviet Physics-Solid State*, vol. 1, 1959, Page 14.

[GAL 16] Gall D.
Electron mean free path in elemental metals. *Journal of Applied Physics*, vol. 119, n° 8, 2016, Page 85101.

[GAN 05] Gan H., Tu K. N.
Polarity effect of electromigration on kinetics of intermetallic compound formation in Pb-free solder V-groove samples. *Journal of Applied Physics*, vol. 97, n° 6, 2005, Page 063514, American Institute of PhysicsAIP.

[GAN 11] Gandhewar V. R., Bansod S. V., BBorade A.
Induction Furnace-A Review. *International Journal of Engineering and Technology*, vol. 3, n° 4, 2011, p. 277–284.

[GAR 03] Garay J. E., Anselmi-Tamburini U., Munir Z. A.
Enhanced growth of intermetallic phases in the Ni-Ti system by current effects. *Acta Materialia*, vol. 51, n° 15, 2003, p. 4487–4495.

[GER 61] Gerardin M.
De l'action de la pile sur les sels de potasse et de soude et sur les alliages soumis à la fusion ignée. rapport, 1861, Sociéte chimique de Paris.

[GOU 15] Gouné M., Danoix F., Ågren J., Bréchet Y., Hutchinson C. R., Militzer M., Purdy G., Van Der Zwaag S., Zurob H.
Overview of the current issues in austenite to ferrite transformation and the role of migrating interfaces therein for low alloyed steels. *Materials Science and Engineering R: Reports*, vol. 92, 2015, p. 1–38.

[GRA 09] Grasso S., Sakka Y., Maizza G.
Electric current activated/assisted sintering (ECAS): A review of patents 1906-2008. *Science and Technology of Advanced Materials*, vol. 10, n° 5, 2009.

[GUA 10] Guan L., Tang G., Chu P. K.
Recent advances and challenges in electroplastic manufacturing processing of metals. *Journal of Materials Research*, vol. 25, n° 7, 2010, p. 1215–1224.

[GUO 15] Guo J. D., Wang X. L., Dai W. B.
Microstructure evolution in metals induced by high density electric current pulses. *Materials Science and Technology*, vol. 31, n° 13, 2015, p. 1545–1554, Taylor & Francis.

[HAR 17] Hariharan K., Moon Jo K., Sung Tae H., Daeyong K., Jung Han S., Myoung Gyu L., Heung Nam H.
Electroplastic behaviour in an aluminium alloy and dislocation density based modelling. *Materials and Design*, vol. 124, 2017, p. 131–142.

[HAU 04] Hau-Riege C. S.
An introduction to Cu electromigration. *Microelectronics Reliability*, vol. 44, n° 2, 2004, p. 195–205.

[HE 17] He K., Wang L.
A review of energy use and energy-efficient technologies for the iron and steel industry. *Renewable and Sustainable Energy Reviews*, vol. 70, 2017, p. 1022–1039.

[HEU 68] Heumann T., Imm R.
Self-diffusion and isotope effect in $\gamma$-iron. *Journal of Physics and Chemistry of Solids*, vol. 29, n° 9, 1968, p. 1613–1621.

[HOC 96] Hocquaux H., Lecourt S., Jacobs H., Derule H., Mataigne J.-m., Mysson C.
*The Book of Steel*. Lavoisier Publishing, intercept édition, 1996.

[HUA 89] Huang S., Meyer M., Pontikis V.
Is Pipe Diffusion in Metals Vacancy Controlled' A Molecular-Dynamics Study of an Edge Dislocation in Copper. *Physical Review Letters*, vol. 63, 1989.

[HUA 04] Huang J., Poole W. J., Militzer M.
Austenite Formation during Intercritical Annealing. *Metallurgical and Materials Transactions A: Physical Metallurgy and Materials Science*, vol. 35, 2004, p. 3363–3375.

[HUM 17] Humphreys J., Rohrer G. S., Rollett A.
The Structure and Energy of Grain Boundaries. *Recrystallization and Related Annealing Phenomena*, Appendix 4, p. 109–143 Elsevier, 2017.

[HUN 61] Huntington H. B., Grone A. R.
Current-induced marker motion in gold wires. *Journal of Physics and Chemistry of Solids*, vol. 20, n° 1-2, 1961, p. 76–87.

[JIN 15] Jin W., Fan J., Zhang H., Liu Y., Dong H., Xu B.
Microstructure, mechanical properties and static recrystallization behavior of the rolled ZK60 magnesium alloy sheets processed by electropulsing treatment. *Journal of Alloys and Compounds*, vol. 646, 2015, p. 1–9.

[KIM 17] Kim M. J., Lee M. G., Hariharan K., Hong S. T., Choi I. S., Kim D., Oh K. H., Han H. N.
Electric current-assisted deformation behavior of Al-Mg-Si alloy under uniaxial tension. *International Journal of Plasticity*, vol. 94, 2017, p. 148–170.

[KLE 62] Klemm A.
Zur Phänomenologie der isothermen Diffusion in Elektrolyten. *Zeitschrift für Naturforschung A*, vol. 17, n° 9, 1962, p. 805–807, De Gruyter.

[KOP 00] Kop T. A., Van Leeuwen Y., Sietsma J., Van Der Zwaag S.
Modelling the austenite to ferrite phase transformation in low carbon steels in terms of the interface mobility. *ISIJ International*, vol. 40, n° 7, 2000, p. 713–718.

[KRI 97] Krielaart G. P., Sietsma J., Van Der Zwaag S.
Ferrite formation in Fe-C alloys during austenite decomposition under non-equilibrium interface conditions. *Materials Science and Engineering A*, vol. 237, n° 2, 1997, p. 216–223.

[KUL 13] Kulakov M., Poole W. J., Militzer M.
The Effect of the Initial Microstructure on Recrystallization and Austenite Formation in a DP600 Steel. *Metallurgical and Materials Transactions A*, vol. 44, n° 8, 2013, p. 3564–3576, Springer.

[KUL 14] Kulakov M., Poole W. J., Militzer M.
A Microstructure Evolution Model for Intercritical Annealing of a Low-carbon Dual-phase Steel. *ISIJ International*, vol. 54, n° 11, 2014, p. 2627–2636.

[LEJ 16] Lejay V., Sidoroff C., Le Bourlot C., Perez M., Dierickx P.
Ageing of 100Cr6 steel: synchrotron X-ray diffraction and dimensional analysis

investigation. *Materials Science and Technology*, vol. 32, n° 11, 2016, p. 1106–1110.

[LI 12] CHUN LI Q., XING LI R., SHUAI LIN D., WEI CHANG G., JIE ZHAI Q.
Influence of Electropulsing Pretreatment on Solid-State Graphitization of Spherical Graphite Iron. *Journal of Iron and Steel Research International*, vol. 19, n° 12, 2012, p. 66–72.

[LI 13] LI P., LI J., MENG Q., HU W., XU D.
Effect of heating rate on ferrite recrystallization and austenite formation of cold-roll dual phase steel. *Journal of Alloys and Compounds*, vol. 578, 2013, p. 320–327, Elsevier.

[LIA 17a] LIANG C.-L., LEE S.-W., LIN K.-L.
The mechanism of an increase in electrical resistance in Al thin film induced by current stressing. *Thin Solid Films*, vol. 636, 2017, p. 164–170.

[LIA 17b] LIANG P., LIN K.-L.
Non-deformation recrystallization of metal with electric current stressing. *Journal of Alloys and Compounds*, vol. 722, 2017, p. 690–697.

[LIN 17] LIN S. K., LIU Y. C. Y. T., CHIU S. J., LIU Y. C. Y. T., LEE H. Y.
The electromigration effect revisited: Non-uniform local tensile stress-driven diffusion. *Scientific Reports*, vol. 7, n° 1, 2017, p. 1–10, Springer US.

[LIU 98] LIU W.-C., CHEN S.-W., CHEN C.-M.
The Al/Ni interfacial reactions under the influence of electric current. *Journal of Electronic Materials*, vol. 27, n° 1, 1998, p. L6–L9.

[LIU 04] LIU F., KIRCHHEIM R.
Grain boundary saturation and grain growth. *Scripta Materialia*, vol. 51, n° 6, 2004, p. 521–525.

[LIU 18] LIU X., ZHANG X.
An ultrafast performance regeneration of aged stainless steel by pulsed electric current. *Scripta Materialia*, vol. 153, 2018, p. 86–89, Acta Materialia Inc.

[LIU 19] LIU M.
Study on microstructural and crystallogarphic characteristics of phase transformation induced by ECP in annealed Cu-40%Zn alloy. Thèse de doctorat, Université de Lorraine, 2019.

[LOV 64] LOVE G.
Dislocation pipe diffusion. *Acta Metallurgica*, vol. 12, n° 6, 1964, p. 731–737.

[LU 14] Lu W. J., Zhang X. F., Qin R. S.
Electropulsing-induced strengthening of steel at high temperature. *Philosophical Magazine Letters*, vol. 94, n° 11, 2014, p. 688–695, Taylor & Francis.

[LU 15] Lu W. J., Zhang X. F., Qin R. S.
Stability of precipitates under electropulsing in 316L stainless steel. *Materials Science and Technology*, vol. 31, n° 13, 2015, p. 1530–1535.

[MAT 21] Mathevon A., Perez M., Massardier V., Fabrègue D., Chantrenne P., Rocabois P.
Gibbs energy minimisation model for the austenite-ferrite phase transformation in Fe-C-X-Y alloys. *Philosophical Magazine Letters*, vol. 101, n° 6, 2021, p. 232–241.

[MEC 15] Mecozzi M. G., Bos C., Sietsma J.
A mixed-mode model for the ferrite-to-austenite transformation in a ferrite/pearlite microstructure. *Acta Materialia*, vol. 88, 2015, p. 302–313.

[MEH 07] Mehrer H.
*Diffusion in Solids*, vol. 155 de *Springer Series in Solid-State Sciences*. Springer Berlin Heidelberg, Berlin, Heidelberg, 2007.

[MUN 11] Munir Z. A., Quach D. V., Ohyanagi M.
Electric current activation of sintering: A review of the pulsed electric current sintering process. *Journal of the American Ceramic Society*, vol. 94, n° 1, 2011, p. 1–19.

[NAK 77] Nakajima H., Hirano K. I.
Electromigration of carbon in $\alpha$-iron. *Journal of Applied Physics*, vol. 48, n° 5, 1977, p. 1793–1796, American Institute of Physics.

[NAK 78] Nakajima H., Hirano K.-i.
Electromigration of Carbon in FCC Fe-0.52wt%C Alloy. *Transactions of the Japan Institute of Metals*, vol. 19, n° 7, 1978, p. 400–409, The Japan Institute of Metals.

[NGU 15] Nguyen-Tran H. D., Oh H. S., Hong S. T., Han H. N., Cao J., Ahn S. H., Chun D. M.
A review of electrically-assisted manufacturing. *International Journal of Precision Engineering and Manufacturing - Green Technology*, vol. 2, n° 4, 2015, p. 365–376.

[OBE 99] Oberlin C.
Électrothermie industrielle - Introduction. *Techniques de l'ingénieur - D5900 V1*, , 1999, p. 1–5.

[OKA 70] Okabe T., Guy A. G.
Steady-state electrotransport of carbon in iron. *Metallurgical Transactions*, vol. 1, n° 10, 1970, p. 2705–2713.

[OKA 73] Okabe T., Guy A. G.
Constancy of Z* for electrotransport of carbon in austenite. *Metallurgical Transactions*, vol. 4, n° 11, 1973, p. 2673–2674.

[OLL 17] Ollat M.
Characterization and modeling of microstructural evolutions during the thermal treatment of cold-rolled Dual-Phase steels. Thèse de doctorat, Université de Lyon, 2017.

[PHI 04] Phillion A., Zurob H. S., Hutchinson C. R., Guo H., Malakhov D. V., Nakano J., Purdy G. R.
Studies of the influence of alloying elements on the growth of ferrite from austenite under decarburization conditions: Fe-C-Ni alloys. *Metallurgical and Materials Transactions A: Physical Metallurgy and Materials Science*, vol. 35 A, n° 4, 2004, p. 1237–1242.

[POL 20] Poletaev G. M., Zorya I. V., Rakitin R. Y., Iliina M. A., Starostenkov M. D.
Interaction of impurity atoms of light elements with vacancies and vacancy clusters in FCC metals. *Materials Physics and Mechanics*, vol. 44, n° 1, 2020, p. 26–33.

[QIN 14] Qin R. S., Rahnama A., Lu W. J., Zhang X. F., Elliott-Bowman B.
Electropulsed steels. *Materials Science and Technology*, vol. 30, n° 9, 2014, p. 1040–1044.

[QIN 15] Qin R. S., Bhowmik A.
Computational thermodynamics in electric current metallurgy. *Materials Science and Technology*, vol. 31, n° 13, 2015, p. 1560–1563.

[RAH 15a] Rahnama A., Qin R. S.
Electropulse-induced microstructural evolution in a ferritic-pearlitic 0.14% C steel. *Scripta Materialia*, vol. 96, n° C, 2015, p. 17–20, Pergamon.

[RAH 15b] Rahnama A., Qin R. S.
The effect of electropulsing on the interlamellar spacing and mechanical properties of a hot-rolled 0.14% carbon steel. *Materials Science and Engineering A*, vol. 627, 2015, p. 145–152, Elsevier.

[ROB 06] Robaut F., Crisci A., Durand-Charre M., Jouanne D.
Practical aspects of carbon content determination in carburized steels by EPMA. *Microscopy and Microanalysis*, vol. 12, n° 4, 2006, p. 331–334.

[ROS 87] Rossiter P. L.
*The electrical resistivity of metals and alloys*. Cambridge University Press, Cambridge, 1987.

[ROS 89] Rosato V.
Comparative behavior of carbon in b.c.c. and f.c.c. iron. *Acta Metallurgica*, vol. 37, n° 10, 1989, p. 2759–2763.

[RUD 17] Rudnev V., Loveless D., Cook R. L., Eds. *Handbook of Induction Heating, second edition*. CRC Press, July 2017.

[SAK 11] Saka M., Ed. *Metallic Micro and Nano Materials Fabrication: Fabrication with Atomic Diffusion*, vol. 1. Springer-Verlag Berlin Heidelberg, 1 édition, 2011.

[SAV 10] Savran V. I., Offerman S. E., Sietsma J.
Austenite nucleation and growth observed on the level of individual grains by three-dimensional X-ray diffraction microscopy. *Metallurgical and Materials Transactions A: Physical Metallurgy and Materials Science*, vol. 41, n° 3, 2010, p. 583–591.

[SCH 81] Schreiber H. U.
Activation energies for the different electromigration mechanisms in aluminum. *Solid State Electronics*, vol. 24, n° 6, 1981, p. 583–589.

[SEI 51] Seith W., Wever H.
Die Aktivität bei der Diffusion in metallischen Dreistoffsystemen. *Zeitschrift für Elektrochemie und angewandte physikalische Chemie*, vol. 55, n° 5, 1951, p. 380–384, John Wiley & Sons, Ltd.

[SHE 18] Sheng Y., Hua Y., Wang X., Zhao X., Chen L., Zhou H., Wang J., Berndt C. C., Li W.
Application of high-density electropulsing to improve the performance of metallic

materials: Mechanisms, microstructure and properties. *Materials*, vol. 11, n° 2, 2018, Multidisciplinary Digital Publishing Institute (MDPI).

[SHU 20] Shu C. C., Liang C. L., Lin K. L.
Electro-work hardening of metals induced by the athermal electromigration effect. *Materials Science and Engineering A*, vol. 772, n° September 2019, 2020, Page 138689, Elsevier B.V.

[SIE 04] Sietsma J., Van Der Zwaag S.
A concise model for mixed-mode phase transformations in the solid state. *Acta Materialia*, vol. 52, n° 14, 2004, p. 4143–4152.

[SKA 14] Skaupy F.
Electral conduction in metals. *Verband Deutscher Physikalischer Gesellschaften*, vol. 16, 1914, Page 156.

[SON 20] Song X., Wang F., Qian D., Hua L.
Tailoring the residual stress and mechanical properties by electroshocking treatment in cold rolled M50 steel. *Materials Science and Engineering A*, vol. 780, n° 139171, 2020.

[SØR 00] Sørensen M. R., Mishin Y., Voter A. F.
Diffusion mechanisms in Cu grain boundaries. *Physical Review B*, vol. 62, n° 6, 2000, p. 3658–3673.

[SPR 86] Sprecher A. F., Mannan S. L., Conrad H.
Overview no. 49. On the mechanisms for the electroplastic effect in metals. *Acta Metallurgica*, vol. 34, n° 7, 1986, p. 1145–1162, Pergamon.

[SUZ 64] Suzuoka T.
Exact Solutions of Two Ideal Cases in Grain Boundary Diffusion Problem and the Application to Sectioning Method. *Journal of the Physical Society of Japan*, vol. 19, n° 6, 1964, p. 839–851.

[VAL 03] Valek B. C., Tamura N., Spolenak R., Caldwell W. A., MacDowell A. A., Celestre R. S., Padmore H. A., Bravman J. C., Batterman B. W., Nix W. D., Patel J. R.
Early stage of plastic deformation in thin films undergoing electromigration. *Journal of Applied Physics*, vol. 94, n° 6, 2003, p. 3757–3761.

[VAS 11] Vasilyev A. A., Sokolov S. F., Kolbasnikov N. G., Sokolov D. F.

Effect of alloying on the self-diffusion activation energy in $\gamma$-iron. *Physics of the Solid State*, vol. 53, n° 11, 2011, p. 2194–2200.

[WAN 20] Wang Y., Yao Y., Long Z., Keer L.
Energy variation in diffusive void nucleation induced by electromigration. *Acta Mechanica Sinica/Lixue Xuebao*, vol. 36, n° 4, 2020, p. 866–872.

[WEL 50] Wells C., Batz W., Mehl R. F.
Diffusion coefficient of carbon in austenite. *Journal of Metals*, vol. 188, 1950, p. 553–560.

[WU 05] Wu A. T., Gusak A. M., Tu K. N., Kao C. R.
Electromigration-induced grain rotation in anisotropic conducting beta tin. *Applied Physics Letters*, vol. 86, n° 24, 2005, p. 1–3, American Institute of Physics.

[XIA 19] Xiang S., Zhang X.
Dislocation structure evolution under electroplastic effect. *Materials Science and Engineering: A*, vol. 761, 2019, Page 138026, Elsevier B.V.

[YAF 09] Yafei S., Dongjie N., Jing S.
Temperature and carbon content dependence of electrical resistivity of carbon steel. *4th IEEE Conference on Industrial Electronics and Applications*, 2009, p. 368–372.

[ZHA 03] Zhang W., Sui M. L., Zhou Y. Z., Li D. X.
Evolution of microstructures in materials induced by electropulsing. *Micron*, vol. 34, n° 3-5, 2003, p. 189–198.

[ZHA 05] Zhang H., Senkara J.
*Resistance welding: Fundamentals and applications*. CRC Press, 2005.

[ZHA 08] Zhang H., Cargill G. S., Ge Y., Maniatty A. M., Liu W.
Strain evolution in Al conductor lines during electromigration. *Journal of Applied Physics*, vol. 104, n° 12, 2008, Page 123533.

[ZHA 14] Zhang J., Zhan L., Jia S.
Effects of electric pulse current on the aging kinetics of 2219 aluminum alloy. *Advances in Materials Science and Engineering*, vol. 2014, 2014.

[ZHA 18] Zhao Y., He B., Saillet S., Domain C., Le Delliou P., Perez M., Qin R.
Anti-aging treatment of nuclear power plant steel. *Materials Science and Engineering: A*, vol. 735, 2018, p. 73–80.

[ZUR 09] Zurob H. S., Hutchinson C. R., Bréchet Y., Seyedrezai H., Purdy G. R.

Kinetic transitions during non-partitioned ferrite growth in Fe-C-X alloys. *Acta Materialia*, vol. 57, n° 9, 2009, p. 2781–2792, Pergamon.

FOLIO ADMINISTRATIF

THESE DE L'UNIVERSITE DE LYON OPEREE AU SEIN DE L'INSA LYON

NOM : MONZEY DATE de SOUTENANCE : le 24 Mars 2022

Prénoms : Maxime Guy Christian

TITRE : Experimental and numerical study of C electromigration in iron during ferrite - austenite phase transformation

NATURE : Doctorat Numéro d'ordre : 2022LYSEI019

École doctorale : ED 34 Matériaux de Lyon

Spécialité : Matériaux

RÉSUMÉ :

Joule heating is widely used during the different thermal treatments and material forming processes in metallurgy. Until recently, thermal treatments assisted by electric current were considered equivalent to conventional heating methods. However, the evolution of the microstructure in presence of electric current is still not well understood.

The aim of this thesis was to determine the impact of an electric current on the diffusion of carbon in iron and on the ferrite-to-austenite phase transformation. To study these phenomena, solid carburization of high-purity iron samples (ARMCO) is performed during thermal treatments in the intercritical domain. Samples are heated thanks to Joule effect induced by direct continuous or pulsed electric current.

A model of carbon diffusion which accounts for both the phase transformation and the electromigration of carbon in iron has been proposed. The sensitivity study on the model parameters showed that the phase transformation kinetics mainly depends on the diffusion coefficient of carbon in austenite. In addition, the effective charge of carbon in austenite can be adjusted to model the electromigration of carbon. Thus, these two parameters were determined based on a comparison between experimental data and simulations.

Phase transformation kinetics were found faster in the direction of the electric current and hindered in the opposite. A 30% higher current density resulted in a diffusion coefficient 50% higher. The effective charge was found to be between +12 and +36, depending on the experimental conditions.

All these results are discussed in the light of the physical phenomena reported in the literature. In particular, they question the studies of the effective charge that do not consider the influence of current on the diffusion coefficient. This PhD-work also provides new values for the effective charge of carbon in the intercritical domain.

MOTS-CLÉS : Electromigration, Carbon, Austenite, Ferrite, Phase transformation

Laboratoire de recherche : MATEIS – UMR CNRS 5510
INSA LYON
25 avenue Jean Capelle
69621 VILLEURBANNE CEDEX

Directeurs de thèse : Patrice CHANTRENNE (Professeur) et Damien FABRÈGUE (Professeur)

Président de jury :

Composition du jury : Benoît APPOLAIRE (Professeur)
Sabine DENIS (Professeure)
Anna FRACZKIEWICZ (Directrice de recherche)
Anne-Françoise GOURGUES-LORENZON (Professeure)
Yann LE BOUAR (Directeur de recherche)
Hugo VAN LANDEGHEM (Chargé de recherche)